Dynamics of beach vortices and multipolar vortex patches

by

Bin Bin Xue M.A.ST.

A thesis submitted in conformity with the requirements

for the degree of Doctor of Philosophy

Department of Mathematics

Faculty of Mathematical & Physical Sciences

University College London

November, 2017

Disclaimer

I, Bin Bin Xue, confirm that the work presented in this thesis is my own. Where information has been derived from other sources, I confirm that this has been indicated in the thesis.

Signature _____

Date _____

Abstract

The classical problem of point vortex equilibria has inspired many studies and discovery of various equilibrium configurations involving non-zero vorticity distributions. That infinitesimal vortices can be 'smeared out' to a finite area vortex patch with constant vorticity to achieve equilibria has attracted large interest due to its relevance to large-scale geophysical flows and the coherent flow structures observed in two-dimensional turbulence. The present work starts with a consideration of monopolar vortex equilibria in 2D inviscid incompressible flows. By employing a Schwarz function method, an exact solution of monopolar equilibria under specific straining field has been found. Numerical considerations are then used to study multipolar vortex equilibria: the '$m+1$' point vortex - vortex patch equilibria are numerically computed and consist of a finite area central patch surrounded by m identical point vortices arranged at the vertices of a polygon. Two distinct families of solutions have been found and their limiting states computed. Linear stability analysis is carried out to study the effect of having a finite area central patch. Numerical routines are further modified to compute the '$m+1$' multipolar vortex equilibria where the m point vortices from the previous configuration are replaced with finite area satellite patches. Various properties are investigated including the limiting

states and non-linear stability through time-dependent integrations. The existence of new, finite area multipolar vortex equilibria are suggested by the streamlines of multipolar vortex equilibria and have thus been found numerically here. A general numerical procedure is described and focus is put on particular multipolar vortex equilibria consisting of two nested polygonal vortex patches. There exist two distinct families of solutions each having a further two separate cases. Time-dependent integrations are carried out to study their non-linear stability and it has been shown in certain unstable solution regimes the nested polygonal vortex equilibria evolve into the '$m+1$' multipolar vortex equilibria.

The second topic here concerns vortex patches over an exponential bottom topography. This study is inspired by rip currents observed when water waves break while propagating alongshore or offshore. Steady translating beach vortices have been found numerically. Asymptotic approximation in the small slope limit is derived and shown to agree well with the numerical solution. Linear stability analysis indicates these structures are linearly stable and time-dependent integrations suggest these are robust structures.

This thesis was completed under the supervision of ***Professor Robb McDonald and Professor Ted Johnson****.*

Acknowledgments

I would like to thank everyone who has given me invaluable support during my Ph.D. studies especially my supervisors Professor Edward Johnson and Professor Robb McDonald. The most sincere thanks to Professor Robb McDonald for his generous and enormous help in every single way.

Bin Bin Xue, *University College London*, November 2017

This page has been left empty intentionally

Contents

List of Figures

Chapter 1

Monopolar vortex patch equilibria

1.1 Introduction

A vortex patch is a two-dimensional finite area region with constant vorticity ω_0 surrounded by an irrotational flow in two dimensions. Arguably the first classical analytical solution for a vortex patch is the Kirchhoff ellipse (Lamb, 1932): an elliptical patch with semi-axes a and b rotating at constant rate $\Omega = \omega_0 ab/(a+b)^2$. Love (1893) investigated its linear stability, and more recently the non-linear stability analysis by Tang (1987) leads to the conclusion that the Kirchhoff ellipse is non-linearly stable for aspect ratio $1/3 < b/a < 3$. An analytical extension to the Kirchhoff ellipse has been given by Moore and Saffman (1971) for a steadily rotating elliptical patch in an imposed strain or shear provided the ratio e/ω_0 is less than a critical value, where e is the strain rate or shear rate. Monopolar vortex equilibria with higher symmetry have been numerically computed in Deem and Zabusky (1978) using contour integral method. The contour integral method reduces the 2D area integral for the velocity field in the problem to a 1D boundary integral, and so brings great simplification. Various forms of equilibria have been revealed using contour integral method and Figure 1.1 shows some of the examples. The primary concern of the first two chapters of this thesis is on steady rotating vortex equilibria

such as the rotating monopole in Figure 1.1(b), and it is assumed all the 2D vortex equilibria in chapters 1 and 2 of this thesis are at a constant rate of rotation Ω. A later study by Wu et al. (1984) reveals families of solutions of monopolar vortex equilibria having various symmetries and were called m-fold V-States (see Figure 1.2). These m-fold symmetric V-states are uniquely defined by two characteristic radii $R_A = r_a$, $R_B = r_b$ (where $r_a > r_b$ by construction) illustrated in Figure 1.1(b). For the solutions with fixed characteristic radius say r_b, there is a range of r_a beyond which no equilibria exist and the monopole attains its limiting state at the maximum value of r_a. A local expansion of the streamfunction by Overman (1986) and Saffman and Tanveer (1982) together with the numerical results in Wu et al. (1984) lead to the conclusion that limiting state must have non-continuous tangent jumps of 90 degree (corners) on the boundary as shown by the outermost boundaries in Figure 1.2 (hereafter, limiting states with corners). It is not ruled out that in some other scenarios, limiting states with 180 degree tangent jumps on the boundary exist (hereafter, limiting states with cusps). A stability analysis of the V-states has been carried out by Burbea and Landau (1982) for $3 \leq m \leq 6$, which leads to the conclusion that V-states are (secularly) stable when their angular velocity Ω lies in a critical range characterised by the number of symmetries.

Aside from the numerically computed equilibria, an analytical construction by Burbea (1981) that studied a m-fold symmetric monopole in a corresponding straining field reveals a limiting state with cusps. Similar limiting state equilibria have been found by Crowdy (2002) for the configuration of a central vortex patch surrounded by identical point vortices arranged at the vertices of a polygon. These equilibria are characterised by zero velocity at all points on the boundary of the central patch viewed in the rotating frame. i.e. a stagnant central vortex patch.

Other well-known vortex equilibria includes a translating dipole (two equal and opposite-signed vortex pairs, see Figure 1.1(a)) computed by Wu et al. (1984) and

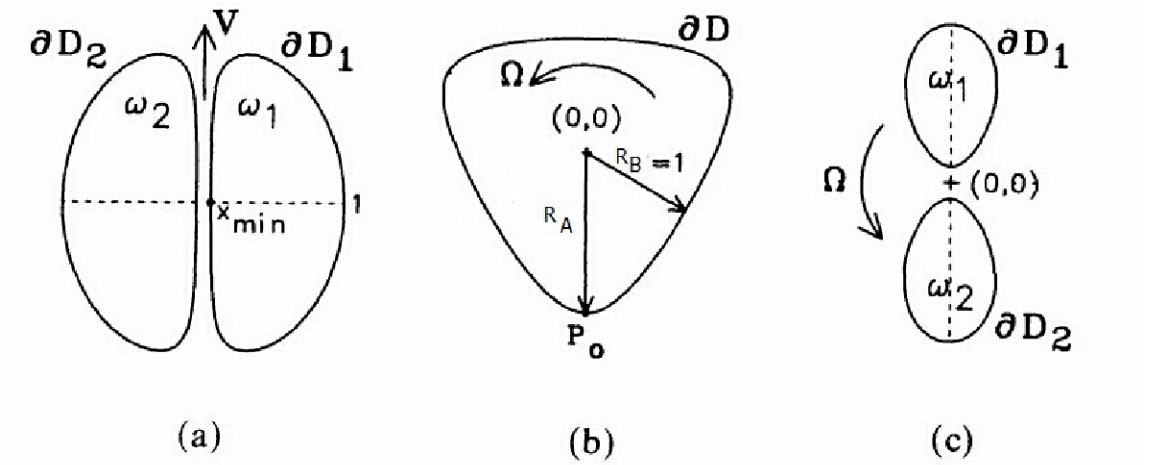

Figure 1.1: From Wu et al. (1984). (a) Steady translating vortex dipole with equal and opposite-signed vorticity. (b) 3-fold symmetric vortex patch in a constant rotation. (c) Co-rotating vortex patches of the same-signed vorticity

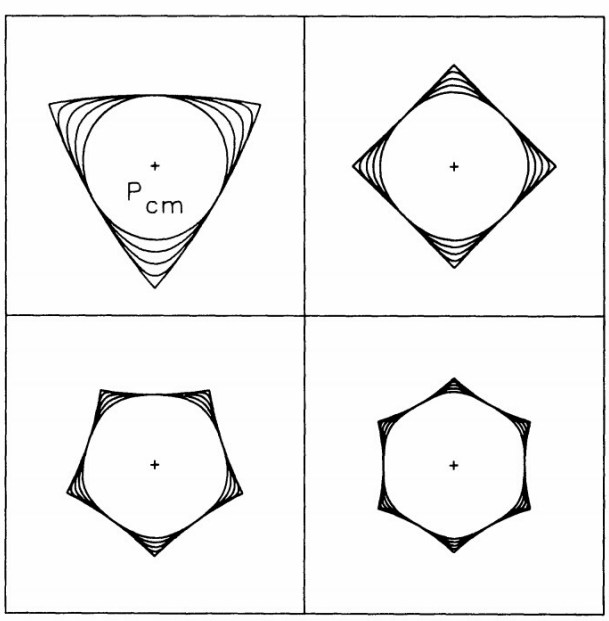

Figure 1.2: From Wu et al. (1984). Families of solutions of rotating V-states for $3 \leq m \leq 6$. The crosses are the centre of vorticity at origin. The limiting states acquire m corners on the boundaries (the outer most boundary in each picture).

Pierrehumbert (1980), co-rotating vortex pairs computed by Saffman and Szeto (1980) (two identical vortex patches, see Figure 1.1(c)), and m-polygon, co-rotating vortex patches computed by Dritschel (1985) (m identical vortex patches arranged at vertices of a m-polygon). More recently, laboratory experiments by Van Heijst and Kloosterziel (1989) demonstrate a robust tripolar vortex equilibria consisting of a central vortex patch surrounded by two opposite-signed satellite vortex patches. Similar structures were subsequently computed by Polvani and Carton (1990) and Morel and Carton (1994). But their solutions are confined to mostly equilibria with zero circulation. It is plausible there exists a much wider class of solution with arbitrary overall circulation including distinct families when the central patch has the same-signed vorticity as the satellite patches.

The first chapter here focuses on the steady rotating m-fold monopolar vortex equilibria of the form in Figure 1.1(b). It is structured as follows: Section 1.2 finds an asymptotic approximation of a near circular m-fold monopolar vortex equilibria. Section 1.3 introduces a conformal mapping method based on Schwarz function to represent the monopolar vortex equilibria. Section 1.4 and Section 1.5 gives some comparisons between the asymptotic approximation, conformal mapping method and the numerical solutions by contour integral method. And Section 1.6 presents some special exact solutions using conformal mapping method under a specific straining field. Finally, Section 1.7 gives a summary.

1.2 The near-circular approximation

The 2D Euler equation in the form of vorticity-streamfunction is:

$$\omega_t + u\omega_x + v\omega_y = 0, \tag{1.1}$$

where ω is the vorticity and is equal to a constant ω_0 inside the boundary of vortex patch and zero outside. The streamfunction ψ satisfies

$$\nabla^2\psi = -\omega, \tag{1.2}$$

and the velocity field is

$$u = \psi_y, \qquad v = -\psi_x, \tag{1.3}$$

$$\text{or} \quad u_r = \frac{1}{r}\frac{\partial\psi}{\partial\theta}, \qquad u_\theta = -\frac{\partial\psi}{\partial r}. \tag{1.4}$$

Assume a m symmetric near-circular vortex patch having boundary described in polar coordinate

$$r = a + \epsilon\cos\left(m\widetilde{\theta}\right), \tag{1.5}$$

where m is an integer, $\epsilon \ll a$ and $\widetilde{\theta}$ is the angle in the rotating frame. Asymptotically, the perturbation to the circular patch gives rise to perturbation vorticity $\epsilon\omega_0\cos(m\widetilde{\theta})$. The corresponding perturbation streamfunction satisfies the equation $\nabla^2\psi_{\text{pert}} = -\epsilon\omega_0\delta(r-a)\cos(m\widetilde{\theta})$. Using Green's function, ψ_{pert} can be expressed as

$$\psi_{\text{pert}}\left(\widetilde{\theta}\right) = -\frac{1}{2\pi}\int_{-\pi}^{\pi}\epsilon\omega_0\cos(m\theta')\log\left|ae^{i\widetilde{\theta}} - ae^{i\theta'}\right| a\mathrm{d}\theta', \tag{1.6}$$

since $u_r = \frac{1}{r}\frac{\partial\psi}{\partial\widetilde{\theta}} = \frac{1}{a}\frac{\partial\psi}{\partial\widetilde{\theta}}$ at $r = a$, so the perturbation radial velocity at $r = a$ becomes

$$u_r^{(p)}(\widetilde{\theta}) = -\frac{1}{4\pi}\epsilon\omega_0\int_{-\pi}^{\pi}\cos(m\theta')\cot\left(\frac{1}{2}(\theta'-\widetilde{\theta})\right)\mathrm{d}\theta', \tag{1.7}$$

where superscript (p) is to refer to the perturbation variables. Now using change of variables this becomes

$$u_r^{(p)}(\widetilde{\theta}) = -\frac{1}{4\pi}\epsilon\omega_0\int_{-\pi}^{\pi}\cos(m\theta' + m\widetilde{\theta})\cot\left(\frac{1}{2}\theta'\right)\mathrm{d}\theta'$$

$$
\begin{aligned}
&= -\frac{1}{4\pi}\epsilon\omega_0 \int_{-\pi}^{\pi} \left[\cos(m\theta')\cos(m\widetilde{\theta}) - \sin(m\theta')\sin(m\widetilde{\theta})\right] \cot\left(\frac{1}{2}\theta'\right) \mathrm{d}\theta' \\
&= -\frac{1}{4\pi}\epsilon\omega_0 \left[\int_{-\pi}^{\pi} \cos(m\theta')\cot\left(\frac{1}{2}\theta'\right)\mathrm{d}\theta'\right]\cos(m\widetilde{\theta})\ \mathrm{d}\theta' \\
&\quad + \frac{1}{4\pi}\epsilon\omega_0 \left[\int_{-\pi}^{\pi} \sin(m\theta')\cot\left(\frac{1}{2}\theta'\right)\mathrm{d}\theta'\right]\sin(m\widetilde{\theta})\ \mathrm{d}\theta', \qquad (1.8)
\end{aligned}
$$

where the first integral on the right is zero since the integrand is odd. The second integral equals 2π, so $u_r^{(p)}(\widetilde{\theta}) = \frac{1}{2}\epsilon\omega_0 \sin(m\widetilde{\theta})$. Since $r = a + \epsilon\cos(m\widetilde{\theta})$, so $u_r^{(p)} = -\epsilon\sin(m\widetilde{\theta})m\dot{\widetilde{\theta}}$, by equating with the $u_r^{(p)}$ just derived, this gives

$$
\dot{\widetilde{\theta}} = -\frac{1}{2}\omega_0/m. \qquad (1.9)
$$

Note a circular patch gives solid body rotation with $\dot{\widetilde{\theta}} = \frac{1}{2}\omega_0$. So the near-circular patch with m-fold symmetry gives rise to rigid rotation of the whole vorticity distribution with angular velocity

$$
\Omega = \frac{1}{2}\omega_0 - \frac{1}{2}\omega_0/m = \frac{1}{2}\omega_0\left(\frac{m-1}{m}\right). \qquad (1.10)
$$

For a 3-fold symmetric near-circular patch, the angular velocity $\Omega = \omega_0/3$. For convenience, consider a 3-fold symmetric vortex patch boundary of the form

$$
r = \frac{1}{2}(r_a + r_b) + \frac{1}{2}(r_a - r_b)\cos\left[3\left(\theta - \Omega t + \frac{\pi}{2}\right)\right],
$$

where r_a and r_b are two characteristic radii of the 3-fold patch defined in Figure 1.1(b). This form is chosen so that $\theta - \Omega t = -\pi/2$ corresponds to $r = r_a$, and $\theta - \Omega t = -\pi/6$ corresponds to $r = r_b$. It is obvious that $a = \frac{1}{2}(r_a + r_b)$ and $\epsilon = \frac{1}{2}(r_a - r_b)$. The vorticity due to the perturbation to circular patch is

$$
\omega_{\text{pert}} = \epsilon \cdot \omega_0 \delta(r - a)\cos\left[3\left(\theta - \Omega t + \frac{\pi}{2}\right)\right],
$$

accurate to $O(\epsilon^2)$. The corresponding streamfunction satisfies

$$\nabla^2\psi_{\text{pert}} = -\epsilon \cdot \omega_0 \delta(r-a)\cos\left[3\left(\theta - \Omega t + \frac{\pi}{2}\right)\right]. \tag{1.11}$$

By expressing $\psi_{\text{pert}} = f(r)\omega_0 \cos\left[3\left(\theta - \Omega t + \frac{\pi}{2}\right)\right]$, it can be shown that $\psi \sim r^3$ for $r < a$ and $\psi \sim r^{-3}$ for $r > a$. Then using continuity of ψ_{pert} at boundary, it is found

$$\psi_{\text{pert}} = \begin{cases} Ar^3\omega_0 \cos\left[3\left(\theta - \Omega t + \frac{\pi}{2}\right)\right], & \text{for } r < a, \\ Aa^6 r^{-3}\omega_0 \cos\left[3\left(\theta - \Omega t + \frac{\pi}{2}\right)\right], & \text{for } r > a, \end{cases} \tag{1.12}$$

where A is a constant. By integrating (1.11) with respect to r from $a-\epsilon_1$ to $a+\epsilon_1$ and taking $\epsilon_1 \to 0$, gives

$$\left.\frac{\partial \psi_{\text{pert}}}{\partial r}\right|_{a-\epsilon_1}^{a+\epsilon_1} = -\epsilon\omega_0 \cos\left[3\left(\theta - \Omega t + \frac{\pi}{2}\right)\right], \tag{1.13}$$

which leads to $A = \frac{\epsilon}{6a^2}$, so the perturbation streamfunction is

$$\psi_{\text{pert}} = \begin{cases} \frac{\epsilon}{6a^2} r^3\omega_0 \cos\left[3\left(\theta - \Omega t + \frac{\pi}{2}\right)\right] & \text{for } r < a, \\ \frac{\epsilon a^4}{6} r^{-3}\omega_0 \cos\left[3\left(\theta - \Omega t + \frac{\pi}{2}\right)\right] & \text{for } r > a. \end{cases} \tag{1.14}$$

Now the velocity field due to a circular patch is

$$u - iv = \begin{cases} -\frac{1}{2} i\omega_0 \bar{z}, & \text{for } |z| < a, \\ -\frac{1}{2} i\omega_0 \frac{a^2}{z}, & \text{for } |z| > a, \end{cases} \tag{1.15}$$

so the streamfunction ψ_{circ} due to a circular patch is

$$\psi_{\text{circ}} = \begin{cases} -\frac{1}{4}\omega_0 |z|^2 + C_1, & \text{for } |z| < a, \\ -\frac{1}{2}\omega_0 a^2 \log|z|, & \text{for } |z| > a. \end{cases} \tag{1.16}$$

Hence the total streamfunction ($\psi = \psi_{\text{pert}} + \psi_{\text{circ}} + \psi_{\text{rot}}$) in the rotating frame is:

$$\psi = \begin{cases} \frac{\epsilon}{6a^2} r^3 \omega_0 \cos\left[3\left(\widetilde{\theta} + \frac{\pi}{2}\right)\right] - \frac{1}{4}\omega_0 |z|^2 + \frac{1}{2}\Omega|z|^2 + C_1, & \text{for } |z| < a, \\ \frac{\epsilon a^4}{6} r^{-3} \omega_0 \cos\left[3\left(\widetilde{\theta} + \frac{\pi}{2}\right)\right] - \frac{1}{2}\omega_0 a^2 \log|z| + \frac{1}{2}\Omega|z|^2, & \text{for } |z| > a, \end{cases} \tag{1.17}$$

where $\widetilde{\theta} = \theta - \Omega t$ is in the rotating frame. $C_1 = \omega_0 a^2/4 - 1/2\omega_0 a^2 \log(a)$ using continuity of streamfunction. This can be rewritten in the complex form

$$\psi = \begin{cases} \frac{\epsilon}{12a^2}\omega_0 \left(z^3 e^{i\frac{3}{2}\pi} + \frac{|z|^6}{z^3} e^{-i\frac{3}{2}\pi}\right) + \frac{1}{4}\omega_0 a^2 - \frac{1}{12}\omega_0 |z|^2, & \text{for } |z| < a, \\ \frac{\epsilon a^4}{12}\omega_0 \left(\frac{z^3}{|z|^6} e^{i\frac{3}{2}\pi} + \frac{1}{z^3} e^{-i\frac{3}{2}\pi}\right) + \frac{1}{2}\omega_0 a^2 \log\left(\frac{a}{|z|}\right) + \frac{1}{6}\omega_0 |z|^2, & \text{for } |z| > a. \end{cases} \tag{1.18}$$

The corresponding velocity field can be found using $u - iv = 2i\frac{\partial \psi}{\partial z}$ which gives

$$u - iv = \begin{cases} \frac{\epsilon}{2a^2} i\omega_0 z^2 e^{i\frac{3}{2}\pi} - \frac{1}{6} i\omega_0 \bar{z}, & \text{for } |z| < a, \\ -\frac{\epsilon a^4}{2z^4} i\omega_0 e^{-i\frac{3}{2}\pi} - \frac{1}{2} i\omega_0 \frac{a^2}{z} + \frac{1}{3} i w_0 \bar{z}, & \text{for } |z| > a. \end{cases} \tag{1.19}$$

The approximate form (1.19) can be used to plot streamlines for various ϵ and find the corresponding stagnation points that must lie on the lines of symmetries of the vortex patch. Results will be shown in Section 1.4.

1.3 Conformal mapping method

This section introduces a conformal mapping to find an analytical representation of V-states using a Schwarz function. It is based on the mapping described in Saffman (1992, p. 167) which demonstrates an alternative derivation of Kirchhoff ellipse exact solution. No exact solution (finite term mapping) can be found for m symmetric V-states for which a truncated finite terms approximation is adopted. Assume there exists a mapping which consists of an infinite series that maps the exterior of a m-

fold vortex equilibria to the exterior of a unit circle. By truncation of the infinite series and using the collocation points on the boundary where it is insisted that the normal velocity in the rotation frame is zero, the coefficients of the truncated series can be found giving an approximation to an equilibrium. The rotational velocity Ω is determined as part of the question. For illustration, consider a 3-fold symmetric patch that is uniquely characterised by chosen values of radii r_a and r_b .

A Schwarz function of a 2D curve C is a function $\Phi(z)$ that equals $\bar{z}$ on C and is analytic in the neighbourhood of C. e.g. for a circle of radius R, $\Phi(z) = R^2/z$. So, for the case of closed C, $\Phi(z)$ can be written as

$$\Phi(z) = F(z) + G(z),$$

where $F(z)$ is analytic inside boundary C and $G(z)$ is analytic outside C. If $\Phi(z)$ has a Laurent expansion in an annulus containing C,

$$\Phi(z) = \sum_{0}^{\infty} f_n z^n + \sum_{1}^{\infty} g_n z^{-n}, \tag{1.20}$$

and F,G are the analytic continuations of the series, then

$$u - iv = \begin{cases} -\frac{1}{2} i\omega_0 G, & \text{outside } C, \\ \frac{1}{2} i\omega_0 F - \frac{1}{2} i\omega_0 \bar{z}, & \text{inside } C, \end{cases} \tag{1.21}$$

so that $v_x - u_y = \omega_0$ inside C. For 3-fold symmetric vortex patches that are not too deformed from circular shapes, it is expected that the Laurent expansion (1.20) exists. Assume the mapping from the exterior of the unit circle (ζ plane) to the exterior of the patch (z plane) is

$$A(\zeta) = z(\zeta) = \zeta \left(a_0 + \frac{a_1}{\zeta^3} + \frac{a_2}{\zeta^6} + \cdots \right), \tag{1.22}$$

which is 3-fold symmetric. Since $\bar{\zeta} = 1/\zeta$ on the unit circle

$$\overline{A(\zeta)} = \overline{z(\zeta)} = \frac{1}{\zeta}\left(\bar{a}_0 + \bar{a}_1\zeta^3 + \bar{a}_2\zeta^6 + \cdots\right), \tag{1.23}$$

on ∂C. So the coefficients g_n, f_n can be evaluated using

$$g_n = \frac{1}{2\pi i}\oint_{\partial C} \bar{z}z^{n-1}\,dz = \frac{1}{2\pi i}\oint_{\partial D(0,1)} \bar{z}z^{n-1}\frac{dA}{d\zeta}\,d\zeta, \tag{1.24}$$

$$f_n = \frac{1}{2\pi i}\oint_{\partial C} \bar{z}z^{-n-1}\,dz = \frac{1}{2\pi i}\oint_{\partial D(0,1)} \bar{z}z^{-n-1}\frac{dA}{d\zeta}\,d\zeta, \tag{1.25}$$

where $\partial D(0,1)$ is the boundary of a unit circle centred at origin. The higher order coefficients $|a_i|$ are expected to decrease. To determine the truncated coefficients $a_0, a_1, \ldots a_{n-1}$ and Ω, total of $2n+1$ equations are required since $a_i, i = 0, 1, \ldots, n-1$ has real and imaginary part. Without loss of generality $\zeta = 1$ is mapped to $z = e^{-\frac{i\pi}{2}}r_a$ and $\zeta = e^{\frac{i\pi}{3}}$ is mapped to $z = e^{-\frac{i\pi}{6}}r_b$. These provide four equations

$$\Re(a_0 + a_1 + a_2 + \ldots + a_{n-1} + ir_a) = 0, \tag{1.26}$$

$$\Im(a_0 + a_1 + a_2 + \ldots + a_{n-1} + ir_a) = 0, \tag{1.27}$$

$$\Re\left(a_0 - a_1 + a_2 - \ldots + (-1)^{n+1}a_{n-1} + ir_b\right) = 0, \tag{1.28}$$

$$\Im(a_0 - a_1 + a_2 - \ldots + (-1)^{n+1}a_{n-1} + ir_b) = 0. \tag{1.29}$$

The remaining $2n-3$ equations required to close the system are taken from the boundary condition requiring the normal velocity $(u - iv)_\zeta \cdot \underline{n} = 0$ in the mapped ζ-plane in the rotating frame. That is,

$$\Re[(u_\zeta - iv_\zeta)\underbrace{(\cos\theta + i\sin\theta)}_{e^{i\theta}=\zeta}] = 0, \tag{1.30}$$

where u_ζ and v_ζ are the velocities in ζ-plane. But

$$u - iv = \frac{d\bar{z}}{dt} = \frac{\partial \bar{z}}{\partial \bar{\zeta}} \frac{d\bar{\zeta}}{dt} = \frac{\partial \bar{A}}{\partial \bar{\zeta}} \frac{d\bar{\zeta}}{dt}, \tag{1.31}$$

so the velocity in the ζ-plane is

$$u_\zeta - iv_\zeta = \frac{d\bar{\zeta}}{dt} = (u - iv) \frac{1}{\frac{\partial \bar{A}}{\partial \bar{\zeta}}}, \tag{1.32}$$

and the boundary condition gives

$$\Re \left[\frac{\zeta}{\frac{\partial \bar{A}}{\partial \zeta}} \{ -\frac{1}{2} i\omega_0 G + i\Omega \bar{z} \} \right] = 0, \tag{1.33}$$

where $u - iv = -\frac{1}{2} i\omega_0 G + i\Omega \bar{z}$ is the velocity outside the vortex patch in the rotating frame. Note $\frac{\partial \bar{A}}{\partial \zeta} \neq 0$ since the mapping is conformal. Since G is a function of z and z is a function of ζ, so the velocity boundary condition (1.33) is a function of ζ, by picking $2n - 1$ collocation points on the unit circle in ζ-plane, this completes a closed system to solve for $a_0, a_1, ...a_{n-1}, \Omega$. The equations are highly non-linear, so successive computation of lower order truncation is used to advance to next order. (i.e. using solution for two terms truncation to initialize the computation of three terms mapping and so on), Newton iteration is used for computation. The remaining task is to find the function G in terms of ζ.

By definition, G is an analytical function outside C. Using the expression for z from (1.22), ζ can be rewritten as

$$\zeta = \frac{1}{a_0} \left(z - \left(\frac{a_1}{\zeta^2} + \frac{a_2}{\zeta^4} + \ldots + \frac{a_{n-1}}{\zeta^{3(n-1)-1}} \right) \right), \tag{1.34}$$

by plugging this into (1.23) it gives

$$\bar{z} = \frac{\bar{a}_0}{\zeta} + \frac{\bar{a}_1}{a_0^2}\left(z - \left(\frac{a_1}{\zeta^2} + \frac{a_2}{\zeta^4} + \ldots + \frac{a_{n-1}}{\zeta^{3(n-1)-1}}\right)\right)^2 + \frac{\bar{a}_2}{a_0^5}(\ldots)^5 + \ldots, \tag{1.35}$$

by picking out the terms (z, ζ) with the power of z less than the power of ζ, the function $G(z(\zeta), \zeta)$ is then found. The function $F(z(\zeta), \zeta)$ is also found in the meantime. This procedure can be implemented into a numerical procedure to solve the system.

For example, for a truncated mapping with 3 terms,

$$z = \zeta\left(a_0 + \frac{a_1}{\zeta^3} + \frac{a_2}{\zeta^6}\right), \tag{1.36}$$

$$\zeta = \frac{1}{a_0}\left(z - \left(\frac{a_1}{\zeta^2} + \frac{a_2}{\zeta^4}\right)\right), \tag{1.37}$$

$$\bar{z} = \frac{\bar{a}_0}{\zeta} + \frac{\bar{a}_1}{a_0^2}\left(z - \left(\frac{a_1}{\zeta^2} + \frac{a_2}{\zeta^4}\right)\right)^2 + \frac{\bar{a}_2}{a_0^5}\left(z - \left(\frac{a_1}{\zeta^2} + \frac{a_2}{\zeta^4}\right)\right)^5. \tag{1.38}$$

for convenience put $t = a_1/\zeta^2 + a_2/\zeta^4$, then $\bar{z}$ can be written as

$$\bar{z} = \frac{\bar{a}_0}{\zeta} + \frac{\bar{a}_1}{a_0^2}\left(-2zt + t^2\right) + \frac{\bar{a}_2}{a_0^5}\left(-5z^4t + 10z^3t^2 - 10z^2t^3 + 5zt^4 + t^5 + 5z^4\frac{a_1}{\zeta^2}\right) + \frac{\bar{a}_1}{a_0^2}z^2 + \frac{\bar{a}_2}{a_0^5}\left(z^5 - 5z^4\frac{a_1}{\zeta^2}\right),$$

where the first three terms are the function G and last two terms are the function F. For n number of terms, the same procedures apply.

This method relies on the existence of the Laurent series. As $|r_a - r_b|$ increases the patch boundary deviates further from the circular shape so the accuracy of this method is expected to drop across some critical ratio of r_a/r_b. To get an idea of the accuracy, comparisons are made to the numerical results from numerical method by Wu et al. (1984) (Denoted WOZ here) which is briefly described in the next chapter. A quantitative error is computed for various r_a with fixed r_b by comparing the boundary points obtained from WOZ method and the conformal mapping method.

The corresponding points found by interpolation using cubic spline interpolation (so they have same corresponding angles) are subtracted, squared, summed and then divided by the total number of points and square rooted:

$$\mathrm{q_{error}} = \sqrt{\frac{\sum_{1}^{\mathrm{npt}}(x_i - x_i^m)^2 + (y_i - y_i^m)^2}{\mathrm{npt}}}, \tag{1.39}$$

where npt is the total number of points, x_i, y_i are the numerically computed patch boundary points and x_i^m, y_i^m are the boundary points through conformal mapping. The quantitative error results will be presented in Section 1.6.

Now using the velocity (1.21), the streamlines can be plotted and stagnation points found. The stagnation points are an important property of the flow fields, new equilibrium can be achieved by growing identical vortices or patches at these stagnation points and these configurations will be studied in Chapter 2. To plot the streamlines, note the derivative of the complex potential W in terms of ζ is

$$\frac{dW}{d\zeta} = \frac{dW}{dz}\frac{dz}{d\zeta} = (u - iv)\frac{dz}{d\zeta}. \tag{1.40}$$

Direct integration with respect to ζ gives the complex potential and hence ψ by taking the imaginary part of the complex potential W, values of $\psi(z(\zeta))$ and its corresponding z can be found and used to plot the streamlines in the z-plane. An extra term $\Omega z\bar{z}/2$ is added to account for the rotating frame.

1.4 Asymptotic approximation versus exact mapping for Kirchhoff vortex

The Kirchhoff elliptical patch is a well known exact analytical solution: an elliptical patch with semi-axes a, b in steady rotation of angular speed $\Omega = \omega_0 ab/(a+b)^2$.

There are many ways to derive this exact analytical solution. It is shown in Saffman (1992) that there is a two term exact conformal mapping for the Kirchhoff ellipse of the type described in Section 1.3. However, no finite term exact mapping can be found for a m-fold V-state ($m \geq 3$). To get a sense of the accuracy of the near circular asymptotic approximation, the exact mapping and the near circular asymptotic approximation of Section 1.3 are compared for the Kirchhoff ellipse.

Using elliptical coordinates, the boundary of an ellipse can be represented by

$$x = c\cosh(\xi)\cos(\eta), \tag{1.41}$$

$$y = c\sinh(\xi)\sin(\eta), \tag{1.42}$$

where a particular ellipse corresponds to $\xi = \xi_0$, and

$$\cosh(\xi_0) = r_b/c, \tag{1.43}$$

$$\sinh(\xi_0) = r_a/c. \tag{1.44}$$

Here r_a, r_b are the two characteristic radii or semi-axes of the ellipse. The streamfunction exterior to the ellipse in the rotating frame found by Kirchhoff is then

$$\psi = \frac{r_a r_b \omega_0}{2}\xi + \frac{r_a r_b \omega_0}{4}e^{-2\xi}\cos(2\eta) - \frac{r_a r_b \omega_0}{4}e^{-2\xi_0}\left(\cosh(2\xi) + \cos(2\eta)\right), \quad \forall\, \xi > \xi_0, \tag{1.45}$$

where $c^2 = r_b^2 - r_a^2$ and the last term is due to steady angular rotation

$$\Omega = \omega_0 \frac{r_a r_b}{(r_a + r_b)^2}. \tag{1.46}$$

For the Schwarz function method, in the rotating frame, the map from the exterior

of a circle (ζ-plane) to the exterior of an ellipse (z-plane) is

$$z = a_0\zeta + \frac{a_1}{\zeta}, \tag{1.47}$$

where a_0 and a_1 are constants. Without loss of generality let $\zeta = 1$ map to $z = r_b$ and $\zeta = i$ map to $z = ir_a$, then

$$a_0 = \frac{1}{2}(r_b + r_a), \qquad a_1 = \frac{1}{2}(r_b - r_a). \tag{1.48}$$

(this implies $a_0, a_1 \in \mathbb{R}$ for the choice of mapping since $r_a, r_b \in \mathbb{R}$). Now the Schwarz function on the boundary is

$$\bar{z} = \frac{a_0}{\zeta} + a_1\zeta = \frac{a_1}{a_0}z + \frac{r_a r_b}{a_0\zeta}, \tag{1.49}$$

since $a_0 a_0 - a_1 a_1 = r_a r_b$. The function which is analytic outside the ellipse G can be read off from (1.49) and is

$$G(z) = \frac{r_a r_b}{a_0\zeta}, \tag{1.50}$$

and the velocity field outside the patch is

$$u - iv = -\frac{1}{2}i\omega_0 G + i\Omega\bar{z} = -i\omega_0\frac{r_a r_b}{2a_0\zeta} + i\omega_0\frac{r_a r_b}{(r_a + r_b)^2}\bar{z}. \tag{1.51}$$

From (1.51) the steady rotational velocity can be shown to be given by (1.46) by applying the boundary condition in (1.33), see Saffman (1992, p. 167). Using (1.40) and by direct integration, the streamfunction in the rotating frame is obtained

$$\psi = \Im\left[-i\omega_0\frac{1}{2}r_a r_b\log\zeta - \frac{1}{4}i\omega_0\frac{r_a r_b}{r_a + r_b}(r_b - r_a)\frac{1}{\zeta^2}\right] + \frac{1}{2}\frac{r_a r_b}{(r_a + r_b)^2}\omega_0 z\bar{z}. \tag{1.52}$$

Now consider the near-circular asymptotic approximation. Given a patch boundary

of the form

$$r = a + \epsilon \cos(2\widetilde{\theta}),$$

the asymptotic rotational velocity is $\Omega = \frac{1}{4}\omega_0$ from (1.10). Now consider an elliptical patch enclosed by the curve

$$r = \frac{1}{2}(r_b + r_a) + \frac{1}{2}(r_b - r_a)\cos\left(2\left(\theta - \Omega t\right)\right), \tag{1.53}$$

where the variables

$$a = \frac{1}{2}(r_b + r_a), \qquad \epsilon = \frac{1}{2}(r_b - r_a). \tag{1.54}$$

Following the same procedure described above, the streamfunction in the rotating frame is found to be

$$\psi = \begin{cases} \frac{\epsilon}{8a}\omega_0\left(z^2 + \frac{|z|^4}{z^2}\right) - \frac{1}{8}\omega_0|z|^2 + \frac{1}{4}\omega_0 a^2, & \text{for } r < a, \\ \frac{\epsilon}{8}a^3\omega_0\left(\frac{1}{z^2} + \frac{z^2}{|z|^4}\right) + \frac{1}{2}\omega_0 a^2 \log\left(\frac{a}{|z|}\right) + \frac{1}{8}\omega_0|z|^2, & \text{for } r > a. \end{cases} \tag{1.55}$$

The streamfunction is expressed in terms of $z, \bar{z}$ for convenience. The velocity field in the rotating frame is then

$$u - iv = \begin{cases} \frac{\epsilon}{2a}i\omega_0 z - \frac{1}{4}i\omega_0\bar{z}, & \text{for } r < a, \\ -\frac{\epsilon}{2}ia^3\omega_0\frac{1}{z^3} - \frac{1}{2}i\omega_0\frac{a^2}{z} + \frac{1}{4}i\omega_0\bar{z}, & \text{for } r > a. \end{cases} \tag{1.56}$$

Three streamlines plots for the exact solution (1.55) are compared to the asymptotic solution in Figure 1.3, for $r_a = 1$ and $r_b = 1.1, 1.4, 1.7$. Since $r_b = r_a + 2\epsilon = 1 + 2\epsilon$ from (1.54), the rotational velocity using (1.46) is

$$\Omega = \omega_0\frac{r_a r_b}{(r_a + r_b)^2} = \frac{1}{4}\frac{1 + 2\epsilon}{(1 + \epsilon)^2}\omega_0 \approx \frac{1}{4}\omega_0 + o(\epsilon^2), \tag{1.57}$$

which shows the approximation (1.10) is accurate to $o(\epsilon^2)$.

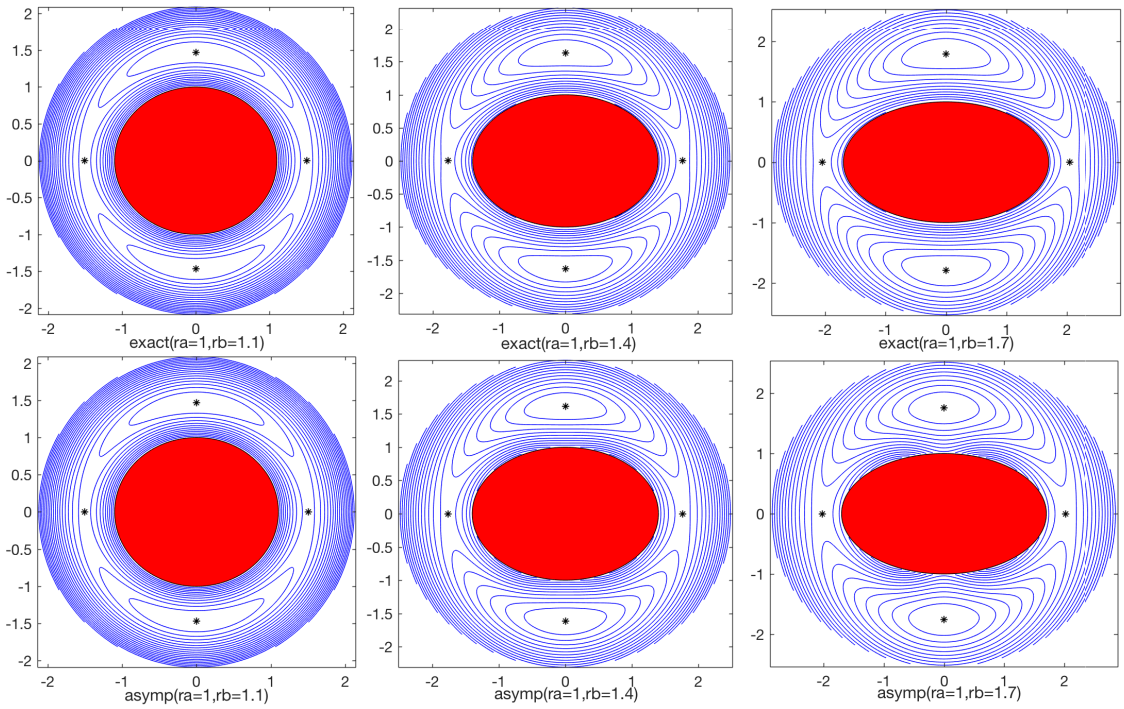

Figure 1.3: Streamlines for Kirchhoff ellipse in rotating frame, shaded region represents vortex patch and asterisks indicates the positions of stagnation points. Upper panels are the exact solutions and lower panels are the asymptotic solutions.

Two pairs of symmetric stagnation points are evident from the streamlines in Figure 1.3: one stable pair on the minor axis of the ellipse, another unstable pair on the major axis of the ellipse. Unstable stagnation point here means a fluid point near it will be carried away and stable means the opposite. The Kirchhoff ellipse is fundamentally different than the m-fold V-states ($m \geq 3$). When a V-state approaches limiting state it has the unstable stagnation points getting closer to the patch boundary, Wu et al. (1984) has shown that limiting state V-state acquires corners on its boundary with non-continuous tangent jump of 90 degree, this suggests the unstable stagnation points meet the corners at the limiting state. In contrast no limiting state has been found for Kirchhoff ellipse since the unstable stagnation points never meet the patch boundary, but instead move infinitesimally close to it. This is easily shown from the exact solution (1.51) for stagnation point on the x-axis

i.e. $\zeta = \xi$. Where the location of the stagnation points are given by

$$\xi^2 = 2 - \frac{a_1}{a_0}. \tag{1.58}$$

Now as the aspect ratio of ellipse increases, a_1/a_0 tends to 1^+ from (1.48). So the stagnation points move infinitesimally close to, but never meet the boundary of the patch. The presence of these stagnation points also suggests new forms of equilibria by 'growing' set of point vortices or vortex patches of either signed vorticity at these stagnation points. Such types of equilibria are explored in the next chapter.

1.5 Conformal mapping versus contour integral method

There are no exact (analytical) solutions found for a m-fold symmetric V-state ($m \geq 3$). The conformal mapping method described above has no exact, finite terms mapping for V-states. However, truncation of the infinite series can give a good approximation for V-states. To get a sense of how accurate this approximation based on conformal mapping is, results by this method are compared to the numerically computed results using WOZ. The second order accurate WOZ routine has been used for computations (second order accurate representation of velocities has been used). Figure 1.4 presents three streamline plots of 3-fold symmetric V-states produced by a standard 4th order Runge-Kutta time-advancing scheme, using boundary points computed from WOZ. The flow field viewed in rotating frame indicates two sets of stagnation points: 3 stable stagnation points which lie on the 'flat' side of the V-states and 3 unstable stagnation points lie on the 'pointy' sides of the V-states. The last picture in Figure 1.4 presents the family of solutions with r_a varying and $r_b = 1$ fixed, and demonstrates that as the limiting state is approached the unstable

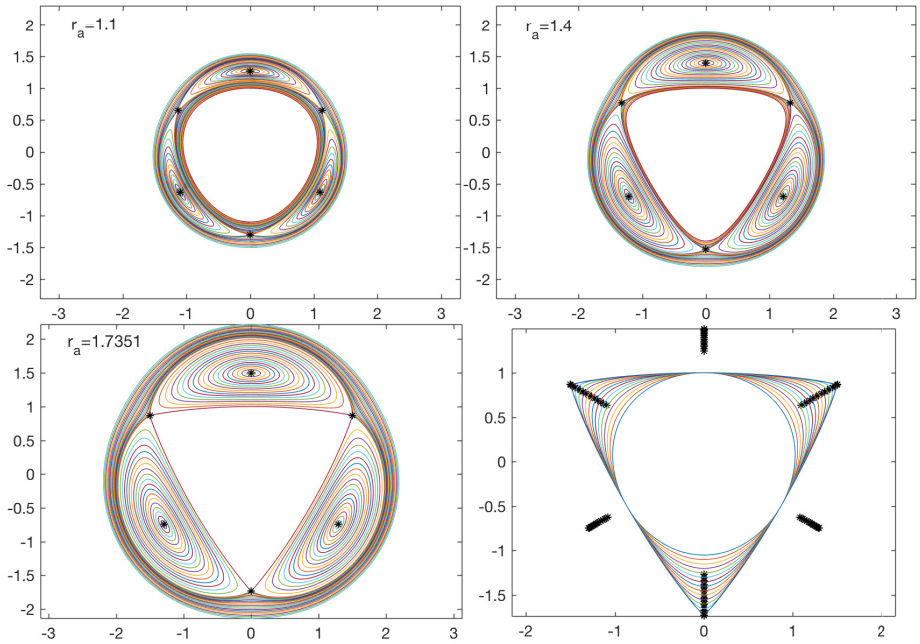

Figure 1.4: Three streamlines plots with the locations of stagnation points for 3-fold symmetric V-states. Last picture shows the family of solutions with variable r_a and $r_b = 1$ with associated stagnation points. Third picture gives the limiting state when the unstable stagnation points meet the patch boundary at the corners.

stagnation points and eventually meets the patch boundary. It has been shown by Overman (1986) that this limiting state must have 90 degree corner of the patch boundary at the location of the stagnation points. Again these stagnation points suggest new vortex equilibria by growing a set of patches of either signed vorticity at them which are to be studied in next chapter.

The 3-fold symmetric V-states computed by WOZ and conformal mapping method are compared. Boundary points are interpolated using cubic spline to R_i having evenly spaced θ_i for comparison. Three or four terms in the mapping (1.22) are used for comparison with higher number of terms introducing negligible improvement on accuracy. The family of solutions defined by fixed $r_b = 1$ with various values of r_a up to the limiting state are compared. In particular, the following are compared: the rotational speed Ω and the location of boundary points in terms of the quantitative error by (1.39). These values are plotted against values of r_a as it increases towards its limiting value. The left picture in Figure 1.5 plots Ω against r_a, and good agree-

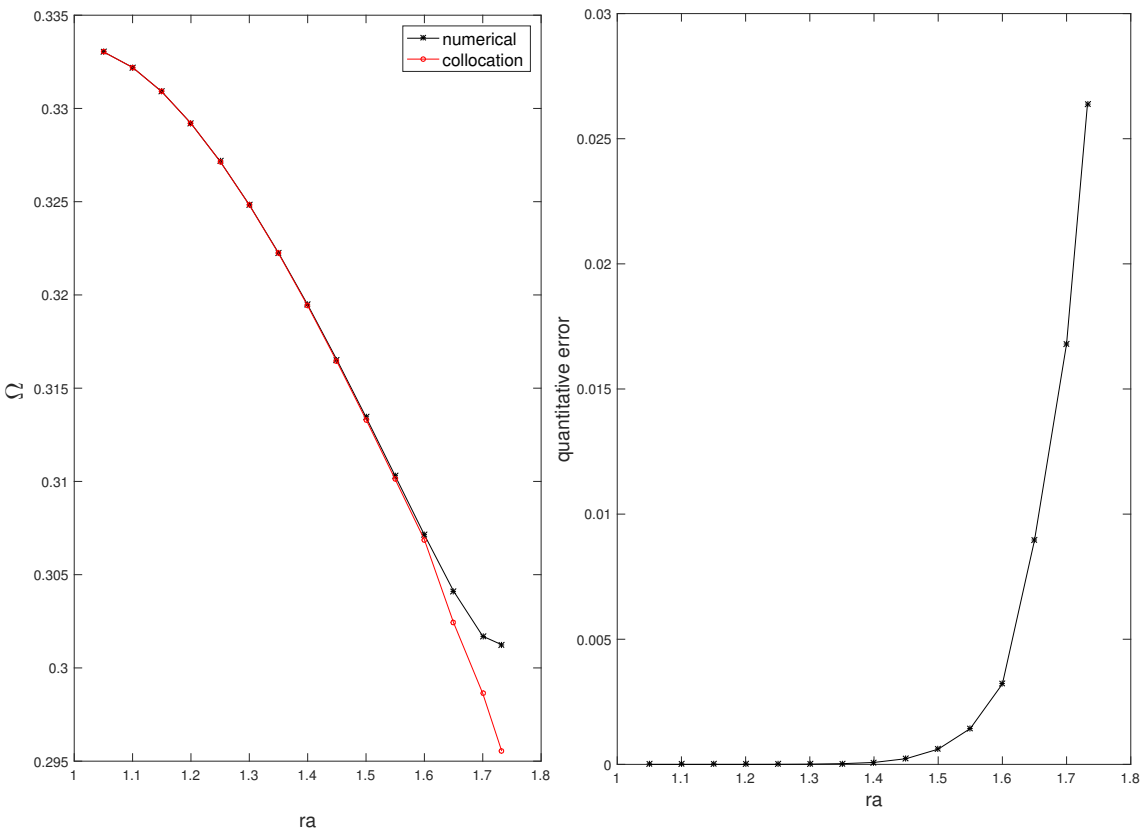

Figure 1.5: 3-fold symmetric V-states comparison: left panel is comparisons of the rotational speed Ω produced by two methods for various r_a, right panel is the plot of corresponding quantitative error of the boundary against r_a.

ment is observed even for r_a approaching its limiting value. The right picture in Figure 1.5 plots the quantitative error against r_a and a dramatic change is evident after a certain value of r_a. Recall that conformal mapping works if the Laurent series exists for function F, G defined above i.e. if the V-states are not too close to limiting states.

1.6 Special exact solutions in a straining field using conformal mapping

Unlike the Kirchhoff ellipse no exact finite terms mapping exists for m-fold ($m \geq 3$) V-states. But, with an additional straining field, an exact, finite terms mapping

has been found here for m-fold ($m \geq 3$) symmetric vortex equilibria. Burbea (1981) presented equivalent analytical results using a different method. Another study by Crowdy (2002) also used a Schwarz function but involved surrounding point vortices of specific strength in place of the straining field. All these result falls into the same category: these equilibria are all characterized by zero velocity on the patch boundary viewed in the rotational frame and the steady rotational velocities are exactly $\omega_0/2$ where ω_0 is the vorticity strength of the patch. Lastly, the limiting states of these equilibria acquire 180 degree tangent jumps (cusps) on the patch boundary rather than corners.

For illustration, the derivation of the exact mapping for the 3-fold symmetric vortex equilibria in a straining field is presented here for a mapping having two terms. Higher symmetry solutions and those with more terms in the mapping can be found similarly. Assume there exists an exact mapping with two terms

$$z = \zeta \left(a_0 + \frac{a_1}{\zeta^3} \right), \tag{1.59}$$

that maps the exterior of a unit circle to the exterior of an 3-fold symmetric vortex patch. For a steady state to exist the boundary conditions in (1.33) must be satisfied. Everything inside (1.33) can be written as a function of ζ where $\zeta = \exp(i\theta)$. By expansion and collection of terms, the boundary condition reduces to

$$C_1(a_0, a_1, \Omega) + C_2(a_0, a_1, \Omega)\cos(3\theta) = 0,$$

where C_1, C_2 are functions of a_0, a_1, Ω, this gives $C_1 = C_2 = 0$, but $C_2 = 0$ gives trivial solution where $a_1 = 0$. To find a non-trivial solution, look for the same mapping for a vortex patch embedded in a specific straining field. By symmetry, this straining field is expected to be of form $b_1 z^2 + b_2 z^5 + \ldots$. Applying the same

boundary condition (1.33) now with extra term due to straining field.

$$\Re\left[\frac{\zeta}{\frac{\partial\bar{A}}{\partial\zeta}}\{-\frac{1}{2}i\omega_0 G + i\Omega\bar{z} + b_1 z^2 + b_2 z^5 + \ldots\}\right] = 0. \tag{1.60}$$

The only possible solution that satisfies boundary condition is $\Omega = \omega_0/2$ and $b_1 = -i\omega_0\bar{a}_1/(2a_0^2)$. An important fact about this solution is that the velocities on the boundary vanish which means the vortex patch remain stagnant in the rotating frame. It is also noted that $b_1 z^2$ is exactly $-i\omega_0 F/2$ where the function F is defined above for the Schwarz function.

An alternative and more general way to derive above result is as follows. Assume there exists an exact mapping with finite terms for a $m \geq 3$ symmetric patch:

$$z = \zeta\left(a_0 + \frac{a_1}{\zeta^m} + \frac{a_2}{\zeta^{2m}}\ldots\right) = \zeta\sum_{i=1}^{k}\left(\frac{a_{i-1}}{\zeta^{m(i-1)}}\right). \tag{1.61}$$

Assume the corresponding external straining field needed to find an equilibrium is $S(z)$. Following the procedure described above, the functions G, F can be found and the Schwarz function equals to their sum $\bar{z} = G + F$ on the boundary. The velocity field outside the patch is defined by the function G in (1.21). Putting all this together, the boundary condition becomes

$$\Re\left[\frac{\zeta}{\frac{\partial\bar{A}}{\partial\zeta}}\{-\frac{1}{2}i\omega_0 G + i\Omega\bar{z} + S(z)\}\right] = 0. \tag{1.62}$$

For the special class solution where $\Omega = w_0/0$, the sum of two terms

$$-\frac{1}{2}i\omega_0 G + i\Omega\bar{z} = \frac{1}{2}iw_0(\bar{z} - G) = \frac{1}{2}iw_0 F, \tag{1.63}$$

where $F(z)$ is a function of z to positive powers which is in the form of straining field. Hence the straining field needed for the steady state is $S(z) = -\frac{1}{2}iw_0 F$, then the velocities on the boundary reduce to zero and are automatically satisfied. So for all

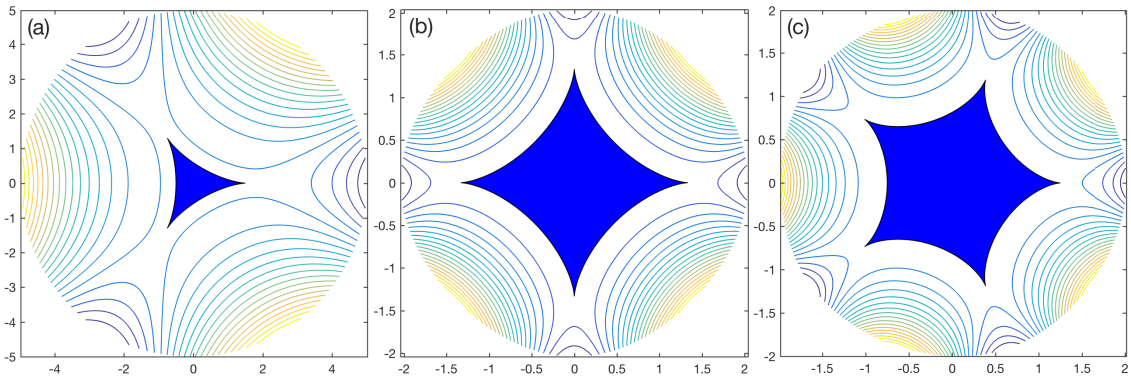

Figure 1.6: Limiting state equilibria with cusps and the streamlines in the rotating frame with $a_0 = 1$ for $m = 3, 4, 5$.

one-to-one mappings of finite terms with m-symmetry, there exists a corresponding equilibrium that is in steady rotation $\Omega = \omega_0/2$ under a specific straining field. Now the velocity field outside the patch is,

$$u - iv = -\frac{1}{2} i\omega_0 \left[\bar{z}\left(\frac{1}{\zeta}\right) - \overline{z(\zeta)} \right]. \tag{1.64}$$

The streamfunction in rotational frame can be found by integration:

$$\psi(\zeta) = \Im\left[\int -\frac{1}{2} i w_0 \bar{z}\left(\frac{1}{\zeta}\right) \frac{dz}{d\zeta}\, d\zeta \right] + \frac{1}{4} w_0 z\bar{z}. \tag{1.65}$$

The requirement that the mapping be one-to-one mapping puts a constraint on ratio $|a_1/a_0|$. To ensure a one-to-one mapping for $|\zeta| > 1$, it is required that

$$\frac{dz}{d\zeta} = a_0 - (m-1)\frac{a_1}{\zeta^m} \neq 0, \qquad \forall |\zeta| > 1, \tag{1.66}$$

which is true only if $|a_1/a_0| \leq 1/(m-1)$. The limiting case when $|a_1/a_0| = 1/(m-1)$ implies $dz/d\zeta = 0$ at m points of the patch boundary. This gives a 'hypotrochoid' cusp shape for the boundaries, see also Burbea (1981).

Figure 1.6 presents the limiting state monopolar vortex equilibria calculated using 2-terms mapping for the cases $m = 3, 4, 5$ with cusps for various symmetry under

a specific straining field. The streamfunction is found using (1.65) through direct integration:

$$\psi = \Im\left[-\frac{1}{2}i\omega_0\left((|a_0|^2-(m-1)|a_1|^2)\log\zeta + \frac{1}{m}a_0\bar{a}_1\zeta^m + \frac{m-1}{m}\frac{\bar{a}_0 a_1}{\zeta^m}\right)\right] + \frac{1}{4}\omega_0 z\bar{z}. \tag{1.67}$$

The background straining field is of the form $-i\omega_0 F/2 = -iw_0\bar{a}_1 z^{m-1}/(2a_0^{m-1})$. Without loss of generality take both coefficients a_0, a_1 to be real and $a_0 = 1$. In the limiting case, $a_1 = a_0/(m-1)$.

More generally, if instead three terms are included in the exact mapping

$$z = \zeta\left(a_0 + \frac{a_1}{\zeta^m} + \frac{a_2}{\zeta^{2m}}\right), \tag{1.68}$$

then equilibria can be found provided they exist in a straining field of the form

$$F = \frac{\bar{a}_1}{a_0^{m-1}}z^{m-1} + \frac{\bar{a}_2}{a_0^{2m-1}}\left(z^{2m-1} + (2m-1)\frac{a_1 z^{2m-2}}{\zeta^{m-1}}\right). \tag{1.69}$$

The streamfunction in the rotating frame is

$$\psi(\zeta) = -\frac{1}{2}\omega_0\Re\left[A(a_0, a_1, a_2, \zeta)\right] + \frac{1}{4}\omega_0 z\bar{z}, \tag{1.70}$$

where the function A is

$$\begin{aligned} A &= \Big[|a_0|^2-(m-1)|a_1|^2-(2m-1)|a_2|^2\Big]\log(\zeta) + \frac{1}{m}\Big[a_0\bar{a}_1 - (m-1)a_1\bar{a}_2\Big]\zeta^m \\ &\quad + \frac{1}{2m}a_0\bar{a}_2\zeta^{2m} + \frac{1}{m}\Big[(m-1)\bar{a}_0 a_1 - (2m-1)\bar{a}_1 a_2\Big]\frac{1}{\zeta^m} + \frac{1}{2m}(2m-1)\bar{a}_0 a_2\frac{1}{\zeta^{2m}}. \end{aligned} \tag{1.71}$$

For the demonstration of the three terms exact mapping, a 4-fold symmetric limiting state equilibrium is presented in Figure 1.7, using the one-to-one condition $dz/d\zeta = 0$ on the boundary as well as fixing two characteristic radii $r_a = 1.4, r_b = 1.2$ which

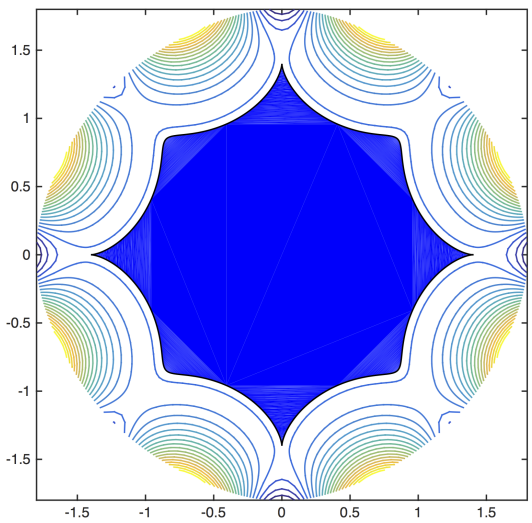

Figure 1.7: Limiting cusp-like 4-fold symmetric equilibrium with streamlines using the three terms mapping with $r_a = 1.4, r_b = 1.2$.

gives three equations to solve for a_0, a_1, a_2. Many other various equilibria can be found.

1.7 Summary

This chapter reviewed the monopolar patch equilibria, in particularly the Kirchhoff ellipse and m-fold V-states. A near-circular asymptotic approximation and an analytical mapping have been derived for m-fold symmetric vortex equilibria. These analytical approximations have been compared to existing exact solutions and numerical results to demonstrate their accuracy. The analytical mapping is based on Schwarz function and has been shown to be accurate when the vortex patch has an aspect ratio within a critical value. Further studies reveal that under a specific straining field, the finite terms conformal mapping represents an exact solution. The corresponding family of solutions described by these exact solutions have limiting states characterized by cusps on the boundary. The next chapter considers vortex patch equilibria of multiple connectivity including a further investigation of limiting

states with cusps or corners.

Chapter 2

Multipolar vortex equilibria

2.1 Introduction

Arising from studies of magnetism and plasma physics, the well known equilibria of identical point vortices arranged at the vertices of a polygon by Thomson (1883) (hereafter called m-polygon point vortex equilibria) inspired many subsequent studies and the search for new equilibria involving point vortices of arbitrary strengths along with their stability analysis. A detailed summary of various forms of point vortex equilibria and their stability analysis has been given in Aref et al. (2002). That infinitesimal vortices can be 'smeared out' to finite area vortex patches with constant vorticity to achieve equilibria has attracted large interest due to its relevance to large-scale geophysical flows and the coherent flow structures observed in quasi-geostrophic or two-dimensional turbulence. Following application of contour dynamics that reduces the problem to 1D boundary integral, various forms of steady rotating finite area vortex equilibria have been revealed. Monopolar vortex equilibria such as m-fold symmetric V-states and Kirchhoff ellipse have been discussed in Chapter 1, much work have also been done on multipolar vortex equilibria such as translating dipole consisting of two identical vortex patches of opposite-signed vorticity in Wu et al. (1984) and Pierrehumbert (1980). Other multipolar vortex

equilibria such as the finite area analogue of m-polygon point vortex equilibria have been numerically computed and thoroughly studied by Dritschel (1985) (hereafter called m-polygon multipolar vortex equilibria). This chapter investigates the steady rotating multipolar vortex equilibria, it is assumed all equilibria in the chapter are in a steady rotation of angular speed Ω.

More recently, numerical and laboratory experiments (see Larichev and Reznik, 1983; Flór et al., 1993; Legras et al., 1988; Larichev and Reznik, 1983; Van Heijst et al., 1991; Carnevale and Kloosterziel, 1994) indicate the existence of coherent rotating tripolar structure and that of higher connectivity. Their point vortex analogues have been summarised in Aref et al. (2002) which consists of m identical point vortices of strength Γ_s arranged at the vertices of polygon and a central point vortex of strength Γ_c at origin. For convenience, they will be called '$m+1$' point vortex equilibria with '1' referring to the single central point vortex. Numerical computations of '$m+1$' configurations having finite area patches in place of point vortices and zero total circulation have been done in Polvani and Carton (1990) and Morel and Carton (1994), they consist of central patch of vorticity surrounded by opposite-signed m identical satellite vortex patches. Numerous studies including laboratory simulations (see Morel and Carton, 1994; Carnevale and Kloosterziel, 1994; Carton, 1992; Carton et al., 1989; Carton and Legras, 1994) indicate these multipolar vortex equilibria with zero total circulation can be generated through barotropic instability of shielded vortex i.e. a shielded circular patch with zero total circulation. These equilibria belong to a more general class which here will be called '$m+1$' multipolar vortex equilibria where '1' refers to the single central patch at origin, including those having same-signed vorticity central patch. Linear stability of '$m+1$' point vortex equilibria depends on the circulation ratio of central point vortex to satellite point vortex shown in Morikawa and Swenson (1971) and Cabral and Schmidt (2000). Such equilibria are linearly stable for a range of circulation ratios both negative and

positive. The presence of a same-signed central point vortex have been shown to make the m-polygon point vortex structures more stable in Morikawa and Swenson (1971). Apart from these 2D vortex equilibria, geophysical tripolar vortex equilibria in a two-layer fluid has been numerically found recently in Reinaud et al. (2017).

A further class of multipolar vortex equilibria are computed here: new finite area vortex equilibria consisting of two sets of nested polygonal arranged vortex patches i.e. a structure comprising two sets of identical vortex patches arranged at the vertices of polygons of different sizes. There exists two distinct cases when two sets of polygonal patches are aligned with each other or staggered, each having two distinct families of solutions when two sets of polygonally arranged patches have same-signed vorticity or opposite-signed vorticity.

This chapter is structured as follows: Section 2.2 gives a brief description of a second order contour dynamics from Wu et al. (1984) for computations of m-fold symmetric V-state, and the co-rotating solution of a single vortex patch with a single point vortex using modified numerical routine. Section 2.3 presents '$m+1$' point vortex - vortex patch equilibria. The limiting state solutions are discussed, and the family is subjected to linear stability. Section 2.4 computes '$m+1$' multipolar vortex equilibria and various limiting state behaviours are investigated. These equilibria are simulated in a time-dependent integration in order to test their stability. In Section 2.5, new finite area equilibria are found numerically which are called here the '$m+m$' equilibria. Results are compared and connections made to the existing equilibria. Finally section 2.6 gives a summary and discussion.

2.2 The modified WOZ method

Using Green's theorem, the streamfunction in (1.2) for piecewise constant vortex patches enclosed by boundaries ∂D_i with vorticity ω_i can be written:

$$\psi(x,y) = -\sum_{i=1}^{\widetilde{N}} \frac{\omega_i}{2\pi} \int_{\partial \mathrm{D}_i} \log(l^{(i)})\, \mathrm{d}\xi^{(i)}\, \mathrm{d}\eta^{(i)}, \tag{2.1}$$

where the superscripts (i) refer to the i-th patch and$\widetilde{N}$ is the number of vortex patches in the configuration, $(\xi^{(i)}, \eta^{(i)}) \in \partial \mathrm{D}_i$ and $l^{(i)}\left(x, y, \xi^{(i)}, \eta^{(i)}\right) = \sqrt{(x-\xi^{(i)})^2 + (y-\eta^{(i)})^2}$. Using integration by parts the velocity field (u, v) at (x, y) can be written:

$$(u,v)(x,y) = -\sum_{i=1}^{\widetilde{N}} \frac{\omega_i}{2\pi} \int_{\partial \mathrm{D}_i} \left[(x-\xi^{(i)}, y-\eta^{(i)})/l^{(i)}\right] \mathrm{d}l^{(i)}. \tag{2.2}$$

In order to be a steady rotating vortex equilibria, the velocity $\mathbf{u} = (u, v)$ on the vortex boundary satisfies

$$(\mathbf{u} - \mathbf{\Omega} \wedge \mathbf{x}) \cdot \mathbf{n} = 0, \tag{2.3}$$

where $\mathbf{\Omega} = \Omega \mathbf{k}$, $\mathbf{k}$ is a unit vector orthogonal to the axis of rotation, and Ω is the rotational velocity of the equilibria. The boundaries of vortex patches in a time-dependent simulation can be evolved using

$$\left(\frac{\mathrm{d}\xi^{(i)}}{\mathrm{d}t}, \frac{\mathrm{d}\eta^{(i)}}{\mathrm{d}t}\right) = (u,v)|_{x=\xi^{(i)}, y=\eta^{(i)}}\,. \tag{2.4}$$

All numerical routines used here are various modified forms of the iterative routines developed by Wu et al. (1984) (hereafter WOZ) and based on a 2nd-order contour dynamics routine to compute the velocities on patch boundaries.

2.2.1 Steady rotating monopolar equilibria

Assume the boundary points (x, y) of a vortex patch in an equilibrium configuration are expressed in polar coordinates relative to its 'centre' e.g centre of mass,

$$(x - x_0, y - y_0) = R(\theta)(\cos\theta, \sin\theta), \tag{2.5}$$

where (x_0, y_0) is the 'centre' of vortex. The boundary condition in (2.3) can be written as

$$u\frac{\mathrm{d}y}{\mathrm{d}\theta} - v\frac{\mathrm{d}x}{\mathrm{d}\theta} + \Omega\widetilde{R}\frac{\mathrm{d}\widetilde{R}}{\mathrm{d}\theta} = 0, \tag{2.6}$$

where $\widetilde{R}$ is the distance of the patch boundary point to the origin, which is equal to R if the vortex is centred at the origin (monopole). Note that

$$\begin{aligned}\widetilde{R}^2 &= (x + x_0)^2 + (y + y_0)^2 \\ &= (R\cos(\theta) + x_0)^2 + (R\sin(\theta) + y_0)^2 \\ &= R^2 + 2R\cos(\theta)x_0 + 2R\sin(\theta)y_0 + x_0^2 + y_0^2.\end{aligned} \tag{2.7}$$

For discretized boundary points, first represent the velocity in (2.2) as

$$(u_k, v_k) = (2\pi)^{-1}\sum_{j=1}^{\widetilde{N}} w_j \sum_{i=1}^{N_T^{(j)}} \frac{(x_k - \xi_{i+1/2}^{(j)}, y_k - \eta_{i+1/2}^{(j)})}{\left[(x_k - \xi_{i+1/2}^{(j)})^2 + (y_k - \eta_{i+1/2}^{(j)})^2\right]^{1/2}}(l_{k,i+1}^{(j)} - l_{k,i}^{(j)}), \tag{2.8}$$

where ω_j is the vorticity of the j-th vortex patch, $\widetilde{N}$ is the total number of vortex patches in the equilibrium, $N_T^{(j)}$ is the total number of points on j-th vortex patch, $f_{i+1/2} = (f_i + f_{i+1})/2$ and $(\xi_i^{(j)}, \eta_i^{(j)}) \in \partial D_j$. Also

$$l_{k,i}^{(j)} = \left[(x_k - \xi_{i+1/2}^{(j)})^2 + (y_k - \eta_{i+1/2}^{(j)})^2\right]^{1/2}.$$

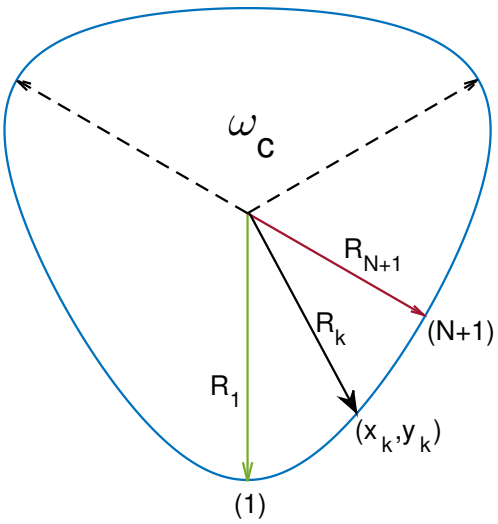

Figure 2.1: Discretization of the boundary of a m-fold symmetry vortex patch for computation. Here $m = 3$. By symmetry, only $1/2m$ section of the boundary needs to be considered. That is R_k for $1 \leq k \leq N+1$ with corresponding $0 \leq \theta_k + \pi/2 \leq \pi/m$. Here $N + 1$ is the number of points on that section of boundary.

For the computation of m-fold symmetric monopolar equilibrium, Figure 2.1 shows $N + 1$ boundary points with R_1, R_{N+1} fixed and R_k adjustable at each iteration. With second order accuracy, the boundary condition in (2.6) is expressed as

$$u_{k+1/2}\Delta y_k - v_{k+1/2}\Delta x_k + (\Omega/2)\Delta\widetilde{R}_k^2 = 0, \qquad 1 \leq k \leq N, \tag{2.9}$$

where $\Delta f_k = f_{k+1} - f_k$ and $u_{k+1/2} = (u_k + u_{k+1})/2$. Substituting (2.7) gives

$$u_{k+1/2}\Delta\left(R_k \sin\theta_k\right) - v_{k+1/2}\Delta\left(R_k \cos\theta_k\right) + (\Omega/2)\left(\Delta R_k^2 + 2\Delta R_k \cos\theta_k x_0 + 2\Delta R_k \sin\theta_k y_0\right) = 0. \tag{2.10}$$

Using (2.5) this can be reduced to

$$R_k - F_{k+1/2}R_{k+1} = 0, \qquad 1 \leq k \leq N, \tag{2.11}$$

or, alternatively

$$R_k - F_{k-1/2}^{-1}R_{k-1} = 0, \qquad 2 \leq k \leq N+1, \tag{2.12}$$

where the function $F_{k+1/2}$ is defined as

$$F_{k+1/2} = \frac{u_{k+1/2}\sin\theta_{k+1} - v_{k+1/2}\cos\theta_{k+1} + (\Omega/2)R_{k+1} + \Omega x_0\cos\theta_{k+1} + \Omega y_0\sin\theta_{k+1}}{u_{k+1/2}\sin\theta_k - v_{k+1/2}\cos\theta_k + (\Omega/2)R_k + \Omega x_0\cos\theta_k + \Omega y_0\sin\theta_k}. \tag{2.13}$$

Now a three-point scheme and a relaxation procedure follows: first average (2.11) and (2.12) to give

$$-\frac{1}{2}F_{k-1/2}^{-1}\bar{R}_{k-1} + \bar{R}_k - \frac{1}{2}F_{k+1/2}\bar{R}_{k+1} = 0, \qquad 2 \le k \le N, \tag{2.14}$$

where $\bar{R}_1 = r_a$, $\bar{R}_{N+1} = r_b$ are prescribed and fixed. Equation (2.14) can then be used to solve for $\bar{R}_k$ given $F_{k+1/2}$. Assume $R_k^{(n)}$ are the boundary points after the n-th iteration. The velocities are found using (2.8) and Ω is updated by summing (2.9) giving

$$\Omega^{(n)} = 2\sum_{k=1}^{N}\left[u_{k+1/2}^{(n)}\Delta y_k^{(n)} - v_{k+1/2}^{(n)}\Delta x_k^{(n)}\right]/\left(\widetilde{R}_1^2 - \widetilde{R}_{N+1}^2\right). \tag{2.15}$$

These in turn gives $F_{k+1/2}^{(n)}$ in (2.13) and can be used to solve for $R_k^{(n+1)}$ using (2.14). Finally a relaxation is used

$$R_k^{(n+1)} = \mu\bar{R}_k^{(n+1)} + (1-\mu)R_k^{(n)}, \tag{2.16}$$

where μ is the relaxation parameter. This completes an iteration. The iteration continues until

$$\sum_{k=1}^{N+1}\left|R_k^{(n+1)} - R_k^{(n)}\right| < 5\times 10^{-7}. \tag{2.17}$$

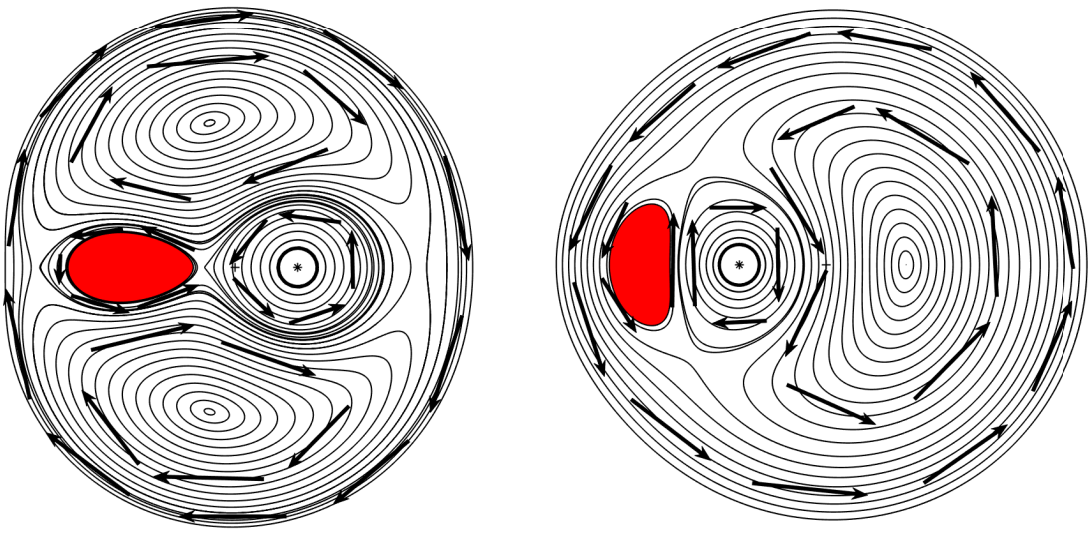

Figure 2.2: (a) Same-signed equilibrium with $r_a = -0.2, r_b = -0.8, \omega_c = 1, r_p = 0.3, \Gamma = 0.262$. (b) Opposite-signed equilibrium with $r_a = -0.72, r_b = -1, \omega_c = 1, r_p = 0.4, \Gamma = -0.272$. Arrows are to indicate the direction of the flows.

2.2.2 Co-rotating equilibria of a single vortex patch with a single point vortex

Now consider the simplest multiply connected vortex equilibria consisting of a single vortex patch with a single point vortex in steady rotation as shown in Figure 2.2. The vortex patch is symmetric against x-axis so it is sufficient to consider the upper half discretized boundary points. To find a unique solution, the parameters r_a, r_b, r_p, ω_c are prescribed and fixed where r_a, r_b are the distances of two patch boundary points that intersect with x-axis to the origin and r_p is the distance of point vortex to the origin, ω_c is the vorticity of the vortex patch. In comparison to a single vortex patch problem, an extra unknown of this problem is the strength of the point vortex Γ which requires an extra boundary equation. This extra boundary condition comes from the fact point vortex stays fixed in the rotational frame. The detailed modified WOZ method used here differs little from computations in Section 2.3 and shall be skipped here.

Two equilibria are plotted in Figure 2.2 with streamlines produced using a stan-

dard 4th order Runge-Kutta scheme to advance in time, the arrows have been added to indicate the direction of flow. There are two scenarios: in the first scenario the vortex patch and point vortex have same-signed vorticity and they rotate around a point in-between them as shown in Figure 2.2(a). In the second scenario, the vortex patch and point vortex have opposite-signed vorticity and they rotate as a pair in a circle relative to the origin as shown in Figure 2.2(b). The same-signed co-rotating equilibrium has an oval vortex patch pointing towards the centre of rotation. There exists an unstable stagnation point between the vortex patch and the point vortex and two stable stagnation points above and below. The opposite-signed equilibrium has the vortex patch flatten against the point vortex with one stable stagnation point on the opposite side of the rotating pair to the origin and two unstable stagnation points on two sides.

2.3 '$m+1$' point vortex - vortex patch equilibria

Now consider equilibria in which a central finite area vortex patch with vorticity ω_c is surrounded by m identical point vortices of strength Γ_s (see Figure 2.3(a)). Hereafter this equilibrium type is called '$m+1$' point vortex - vortex patch equilibria. Symmetry considerations dictate that the central patch must have m-fold symmetry. There are 5 parameters in this problem: two characteristic radii of the central patch R_1, R_{N+1}, the radial distance b of the point vortices to the origin, ω_c (or the total circulation of the patch Γ_c) and Γ_s, the circulation of the satellite point vortices. Prescribing four of them uniquely defines an equilibrium. Two modified WOZ methods have been used for computation of the equilibria and are briefly described below. One routine seeks convergent solutions with prescribed $R_1 = a_1$, b, ω_c, Γ_s, the other prescribes $R_1 = a_1$, $R_{N+1} = a_2$, b, ω_c. For all the computations, at

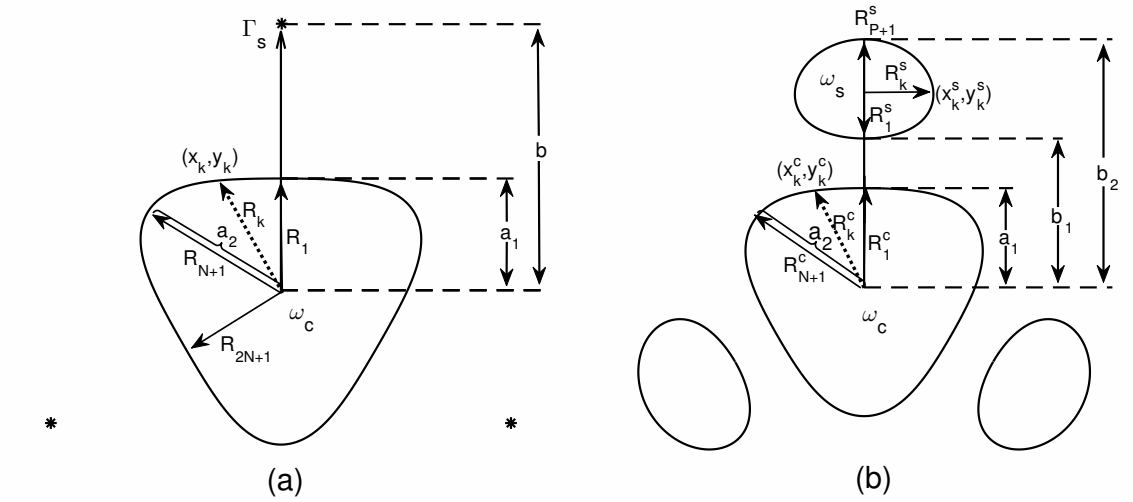

Figure 2.3: Schematic diagram of (a) '3+1' point vortex - vortex patch equilibria, (b) '3+1' multipolar vortex equilibria along with their boundary points discretizations and parameters for numerical considerations.

least 300 discretized boundary points have been used on each symmetric section of the individual patch.

To find the convergent solution uniquely defined by $R_1, b, \omega_c, \Gamma_s$, the boundary points on a $1/m$ section of the central patch needs to be considered using the procedure described in Section 2.2.1 i.e. the boundary points R_k for $1 \leq k \leq 2N+1$ in Figure 2.3(a) where $R_1 = R_{2N+1} = a_1$ (due to symmetry) are prescribed. A circular patch is used to initialise the central patch for computation. The rotational velocity Ω cannot be updated using (2.15) since $R_1 = R_{2N+1}$. Instead, it is updated using the boundary condition that the point vortex is fixed in the rotating frame:

$$\begin{aligned} & u\left(\omega_c, \Gamma_s, b, x_k^{(n)}, y_k^{(n)}\right) + \Omega^{(n+1)} b = 0, \\ \text{or} \qquad & \Omega^{(n+1)} = u\left(\omega_c, \Gamma_s, b, x_k^{(n)}, y_k^{(n)}\right)/b, \end{aligned} \tag{2.18}$$

where u is the velocity at the point vortex and $\left(x_k^{(n)}, y_k^{(n)}\right)$ are the boundary points at the n-th iteration. The procedure now follows that of Section 2.2.1.

An alternative is to find a convergent solution by prescribing parameters R_1, R_{N+1}, b, ω_c. This means the strength of satellite point vortices Γ_s needs to be

determined as part of the solution. The initial profile for central patch to initialise computation is

$$R = \frac{1}{2}(a_1 + a_2) + \frac{1}{2}(a_1 - a_2)\cos(m(\theta + \pi/2)). \tag{2.19}$$

so that $\theta = 0$ gives $R_1 = a_1$ and $\theta = \pi/m$ gives $R_{N+1} = a_2$. The boundary points that needs to be updated are R_k for $2 \leq k \leq N$. At the n-th iteration with boundary points $\left(x_k^{(n)}, y_k^{(n)}\right)$, the boundary condition from (2.15) and (2.18) give two linear equations for Ω and Γ_s. The velocities are split into two parts: a contribution from the central patch and a contribution from point vortices as follows

$$\begin{aligned} \omega_c \sum_{k=1}^{N} \left[u_{k+1/2}^{(cc)} \Delta y_k^{(n)} - v_{k+1/2}^{(cc)} \Delta x_k^{(n)}\right] + \frac{\Gamma_s^{(n+1)}}{2\pi} \sum_{k=1}^{N} \left[u_{k+1/2}^{(cp)} \Delta y_k^{(n)} - v_{k+1/2}^{(cp)} \Delta x_k^{(n)}\right] \\ + \frac{\Omega^{(n+1)}}{2}\left(R_{N+1}^2 - R_1^2\right) = 0, \\ \omega_c u^{(pc)} + \frac{\Gamma_s^{(n+1)}}{2\pi} u^{(pp)} + \Omega^{(n+1)} b = 0, \end{aligned} \tag{2.20}$$

where $u_{k+1/2}^{(cc)}$ is the velocity on the central patch boundary points induced by the central patch of unit strength and $u_{k+1/2}^{(cp)}$ is the velocity on the central patch due to the surrounding point vortices of unit strength, $u^{(pc)}$ is the velocity at the point vortex induced by unit strength central patch and $u^{(pp)}$ is the velocity owing to the other point vortices. The coupled linear equations (2.20) are solved to find $\Omega^{(n+1)}, \Gamma_s^{(n+1)}$ enabling $F_{k+1/2}$ to be found. The rest follows from Section 2.2.1.

2.3.1 Summary of numerical results and some observations

These two numerical routines have been cross-checked and found to agree with each other. Fixing the two characteristic radii R_1, R_{N+1} of the central patch while relaxing the constraint on Γ_s reveals a family of solutions with a limiting state central patch. Figure 2.4 shows families of equilibria obtained by prescribing R_1, R_{N+1} with values a_1, a_2 for various aspect ratios a_2/a_1. All the solutions are normalised so that the satellite point vortices have unit strength and are unit distance from the origin i.e. $\Gamma_s = 1$, $b = 1$. The circulation ratio of the central patch to point vortices is denoted as $\alpha = \Gamma_c/\Gamma_s$. There are two distinct families of solutions: the equilibria with $a_2/a_1 > 1$ have corresponding $\alpha < 0$ (i.e. central patch and satellite patches have opposite-signed circulation), while those with $a_2/a_1 < 1$ have corresponding $\alpha > 0$ (same-signed circulation). The opposite-signed ($\alpha < 0$) equilibria have the boundary of the central patch flatten on the side nearest surrounding point vortices as shown in Figure 2.4(a,b,c), while same-signed ($\alpha > 0$) equilibria have the boundary of central patch pointing towards each of the surrounding point vortices as shown in Figure 2.4(d,e,f).

Solution families are computed and limiting states approached by increasing or decreasing the a_2/a_1 ratio. In the $\alpha > 0$ family it is clear that the limiting states acquire corners on the central patch boundary when a_2/a_1 is decreased to a minimum as shown in Figure 2.4(d,e,f), and in the $\alpha < 0$ family limiting states are approached when a_2/a_1 is increased to a maximum as shown in Figure 2.5. A clear indication of the occurrence of a limiting states is when increasing or decreasing the aspect ratio a_2/a_1, the stagnation points of the flow (not shown) found on the lines of symmetry of the central patch meet the boundary. This means in Figure 2.4(d,e,f) the limiting states have stagnation points on the corners for $\alpha > 0$ equilibria, while the limiting

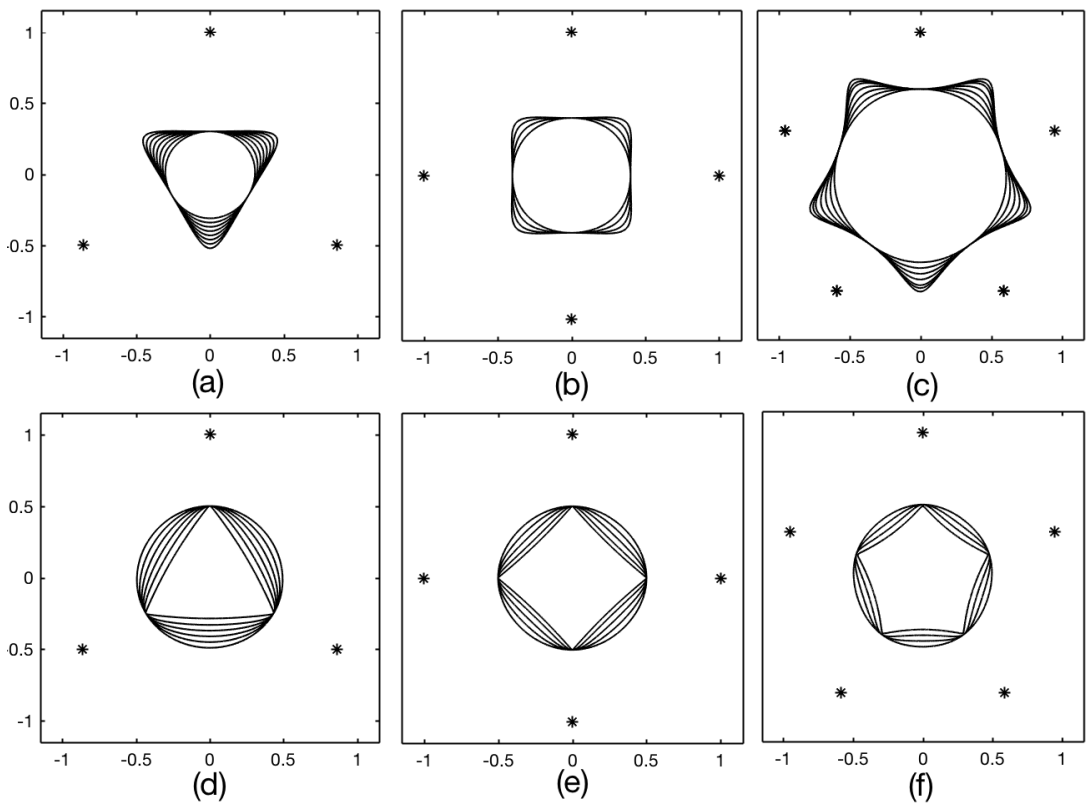

Figure 2.4: Families of solutions of normalised (i.e $b = 1, \Gamma_s = 1$) '$m + 1$' point vortex - vortex patch equilibria with $3, 4, 5$-fold symmetry. (a,b,c) shows opposite-signed equilibria ($\alpha < 0$) with solutions corresponding to (a) $a_1 = 0.3$ with values of a_2 from a_1 increasing to 0.541. (b) $a_1 = 0.4$ with values of a_2 from a_1 increasing to 0.524. (c) $a_1 = 0.6$ with values of a_2 from a_1 increasing to 0.814. (d,e,f) shows same-signed equilibria ($\alpha > 0$) with solutions corresponding to (d) $a_1 = 0.5$ with values of a_2 from a_1 decreasing to 0.285. (e) $a_1 = 0.5$ with values of a_2 from a_1 decreasing to 0.34. (f) $a_1 = 0.5$ with values of a_2 from a_1 decreasing to 0.375.

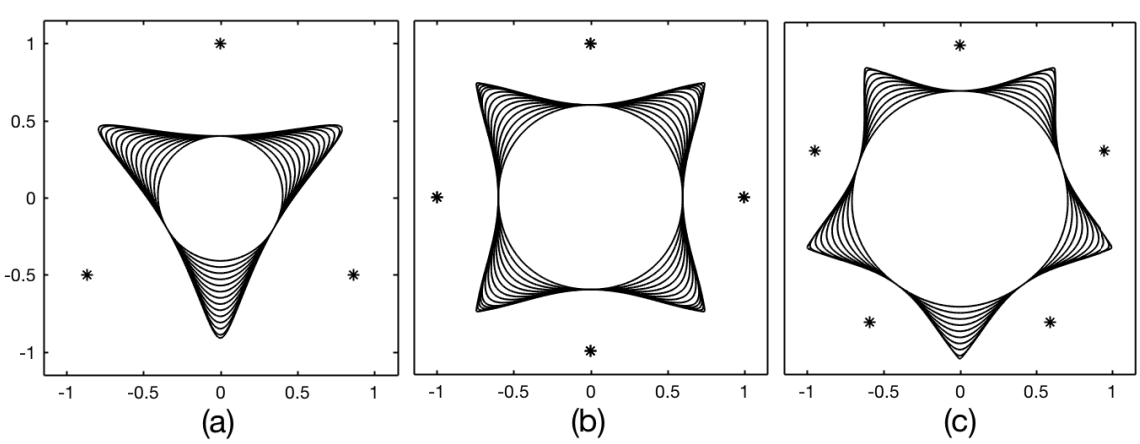

Figure 2.5: Families of solutions of normalised opposite-signed '$m + 1$' point vortex -vortex patch equilibria ($\alpha < 0$) with 3,4,5-fold symmetry. Solutions correspond to (a) '3+1' equilibria having $a_1 = 0.4$ with values of a_2 from a_1 up to 0.94. (b) '4+1' equilibria having $a_1 = 0.6$ with values of a_2 from a_1 up to 1.05. (c)'5+1' equilibria having $a_1 = 0.7$ with values of a_2 from a_1 up to 1.05.

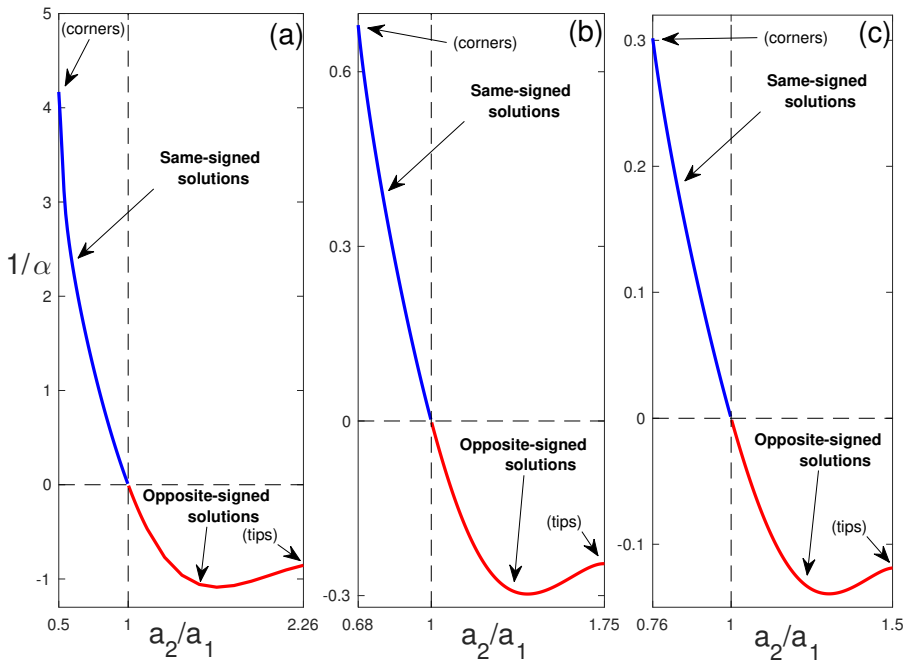

Figure 2.6: Plots of inverse circulation ratio $1/\alpha$ against a_2/a_1 for complete families of solutions with 3,4,5-fold symmetry. (a) '3+1' solutions with $a_1 = 0.4$. (b) '4+1' solutions with $a_1 = 0.6$. (c) '5+1' solutions with $a_1 = 0.7$. Minimum a_2/a_1 corresponds to same-signed limiting equilibria with corners and the maximum a_2/a_1 corresponds opposite-signed limiting equilibria with tips.

states for $\alpha < 0$ equilibria, as shown in Figure 2.5, have stagnation points at the tips of central patch. To illustrate the complete solution for the families with given choice of a_1, the inverse circulation ratio $1/\alpha$ is plotted against a_2/a_1 in Figure 2.6. The inverse circulation ratio changes sign when the aspect ratio $a_2/a_1 = 1$ i.e. a circular patch, and the satellite vertices have zero strength. Note also that increasing the number of satellite point vortices gives shorter range of solutions for a_2/a_1 but supports a larger central patch. It is expected that when $m \to \infty$ the equilibrium must have circular central patch. As $a_1 \to 0$ i.e a smaller central patch, equilibria with an infinite range of circulation ratios $-\infty \leq \alpha \leq \infty$ is recovered as in the 'm+1' point vortex equilibria in Morikawa and Swenson (1971).

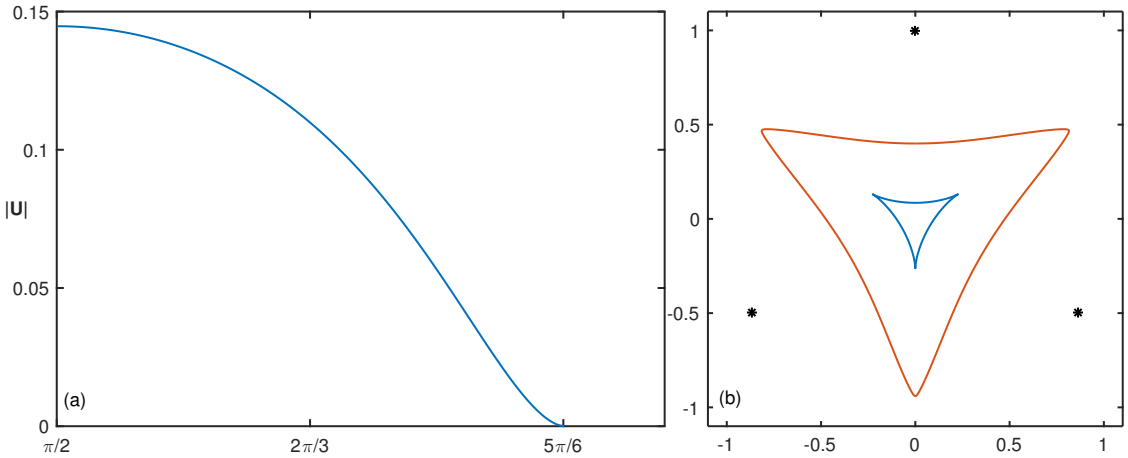

Figure 2.7: Comparisons of numerically computed limiting state opposite-signed '3+1' equilibrium and the exact limiting state solution. (a) Absolute velocity profile on $1/(2m)$ section of the central patch boundary of the numerically produced equilibrium in rotating frame. (b) Outer central patch corresponds to numerically produced limiting state for prescribed $a_1 = 0.4$, $a_2 = 0.94$ giving $\alpha = -1.19$ and inner central patch corresponds to exact solution in Crowdy (2002) having cusps with parameters $a_1 = 0.085$, $a_2 = 0.261$, $\alpha = -0.0149$.

2.3.2 Discussion of limiting states of normalised solutions

The local expansion of the streamfunction in Overman (1986) leads to the conclusion that limiting state m-fold rotating vortex equilibria must have non-continuous tangent jumps of 90 degree (corners) on its boundary, but it does not rule out the possibility of a cusp type limiting state in other scenarios involving the presence of background flows, possibly due to other vortex patches. As found here, limiting corner-like equilibria arise in same-signed solution families, and limiting states with tip-like central patch arise in the opposite-signed solution families. For opposite-signed equilibria, there exist analytical results from Burbea (1981) and Crowdy (2002) with limiting states having cusps, these being the equivalent of the tips of normalised solutions presented here. These solutions either have surrounding point vortices on the 'flat' side of central patch (see Crowdy (2002)) as in the numerical solutions presented here or involve a patch embedded in a straining field that pro-

vides an equivalent effect in Burbea (1981). They both share the property that the tangential and normal velocities on the patch boundary are identically zero when viewed in the rotating frame, and the equilibria have steady rotational speed of exactly $\omega_c/2$. The exact solutions from Crowdy (2002) with surrounding point vortices lie outside the range of solutions that are capable of being computed by the numerical routine used here. In Figure 2.7(a) the absolute velocity in the rotating frame for a numerically computed '3+1' limiting state opposite-signed equilibrium is plotted against θ for the section of central patch boundary points defined by R_1 to R_{N+1} as in Figure 2.3(a). The patch boundary attains the maximum absolute velocity at R_1 and gradually decreases towards zero at the tips as shown in Figure 2.7(a). In contrast the exact analytical solution from Crowdy (2002) has zero velocity profile for all θ. Figure 2.7(b) plots the numerically produced opposite-signed '3+1' limiting state solution and the exact analytical solution in Crowdy (2002), scaled so that the point vortices coincide. This indicates the exact analytical solution is a special member of the opposite-signed family of solutions.

2.3.3 Linear stability analysis

The linear stability of both m-polygon point vortex equilibria (m identical point vortices arrange at the vertices of m-gon) and its finite-area analogous m-polygon co-rotating vortex patch equilibria (i.e. with the surrounding point vortices replaced by patches whose shape is numerically computed) have been thoroughly studied by Dritschel (1986). It is well known that m-polygon point vortex equilibria are linearly stable if $m \leq 7$ and unstable for $m \geq 8$. This mode of instability for $m \geq 8$ will be referred to as 'circular instability'. If a central vortex is added, then linear stability analysis of '$m+1$' point vortex equilibria by Morikawa and Swenson (1971) with the satellite point vortices with unit distance from the central patch, reveals stability

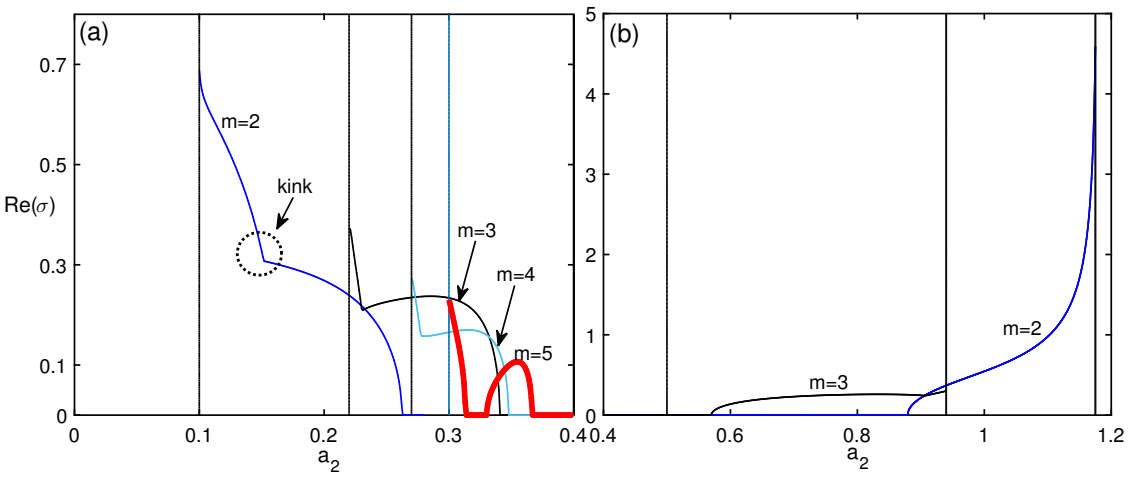

Figure 2.8: Max over $i, i = 1, 2, \ldots, M$ the absolute real part of eigenvalues $\mathrm{Re}(|\sigma|)$ plotted against values of a_2 for a family of equilibria with $a_1 = 0.4$ fixed. (a) Same-signed equilibria with $a_2 < a_1$. The thick line is for $m = 5$ case. (b) Opposite-signed equilibria with $a_2 > a_1$.

regions within which the configurations are Liapunov stable:

$$\begin{aligned} m = 3, \quad & -0.5 < \alpha < 1, \\ m = 4, \quad & -0.5 < \alpha < 2.25, \\ m = 5, \quad & -0.5 < \alpha < 4, \\ m = 6, \quad & -0.25 < \alpha < 6.25. \end{aligned} \tag{2.21}$$

There are two instability mechanisms described in Morikawa and Swenson (1971) (i) central point vortex instability, where the location of the central point vortex is unstable if α is below the lower negative threshold, and (ii) circular instability affecting the surrounding m point vortices if α is above the upper positive threshold. The presence of same-signed central point vortex is shown to stabilize the m-polygon point vortex equilibria in Morikawa and Swenson (1971).

To study the effect of having a finite area central patch in the '$m + 1$' equilibria, consider a perturbation on the central patch boundary while keeping the point vortices fixed. A numerical method from Dritschel (1985) is used, adapted here to include surrounding point vortices. A brief description is given here and more details

will be provided in Chapter 3. Consider a perturbed central patch boundary

$$r(\theta) = r_0(\theta) + \widehat{r}(\theta)e^{\sigma t}, \tag{2.22}$$

where r_0 is the unperturbed central patch boundary in an '$m+1$' equilibrium, the second term is the small perturbation ($\widehat{r} \ll r_0$) to the boundary which is in the form of normal mode. The real part of σ is the growth rate and the imaginary part is the frequency of the boundary disturbance. The form of $\widehat{r}(\theta)$ is expressed as

$$\widehat{r}(\theta) = r_0(\theta) \sum_{i=1}^{M} C_i \phi_i(\theta), \tag{2.23}$$

where ϕ_i are the orthonormal functions

$$\pi^{\frac{1}{2}}\phi = \left(\frac{1}{\sqrt{2}}, \cos\theta, \ldots, \cos(P\theta), \sin\theta, \ldots, \sin(P\theta) \right). \tag{2.24}$$

Hence $M = 2P + 1$ and C_i are the coefficients to be determined. The points on the perturbed boundary move with local fluid velocity

$$\frac{\partial r}{\partial t} + \frac{u_\theta}{r}\frac{\partial r}{\partial \theta} = u_r, \tag{2.25}$$

where u_θ, u_r are the tangential and radial velocity on the patch boundary in the rotating frame with the contributions of fixed point satellite vortices taken into account. Inserting (2.22) into (2.25) gives

$$\sigma\widehat{r} - \frac{u_{\theta 0}}{r_0^2}\frac{dr_0}{d\theta}\widehat{r} + \frac{u_{\theta 0}}{r_0}\frac{d\widehat{r}}{d\theta} + \frac{1}{r_0}\frac{dr_0}{d\theta}\widehat{u}_\theta = \widehat{u}_r, \tag{2.26}$$

where $u_{\theta 0}$ is the unperturbed tangential velocity and $\widehat{u}_\theta, \widehat{u}_r$ are the perturbation velocities. Using the linearised velocity equation (2.26) and Galerkin method requiring

that

$$\int_0^{2\pi} \epsilon(\theta')\phi_i(\theta')d\theta' = 0, \quad i = 1, 2, \ldots, M, \tag{2.27}$$

this leads to an eigenvalue problem

$$\sigma \boldsymbol{C} = \boldsymbol{A}\boldsymbol{C}. \tag{2.28}$$

where $\boldsymbol{C} = (C_1, C_2, \ldots, C_M)$ and $\boldsymbol{A}$ is a real $M \times M$ matrix. Here $M = 201$, equation (2.28) can be used to find $\sigma_i, i = 1, 2, \ldots, M$. The maximum growth rate, $\max(\mathbf{Re}(\sigma_i)), i = 1, 2, \ldots, M$ is plotted against values of a_2 in Figure 2.8 for normalised solutions of '$m+1$' point vortex - vortex patch equilibria with fixed $a_1 = 0.4$. Figure 2.8(a) plots the maximum growth rate for same-signed equilibria and Figure 2.8(b) for opposite-signed equilibria. The vertical lines in Figure 2.8(a,b) indicate the lower and upper limit of a_2 beyond which no equilibria are found. Recall also that $a_2 < a_1$ corresponds to same-signed equilibria and $a_2 > a_1$ corresponds to opposite-signed equilibria.

When $|a_2 - a_1|$ is small, the central patch is near circular and the absolute relative circulation ratio $|\alpha|$ is large then the central patch is linearly stable. On the other hand, when $a_2 - a_1$ approaches the upper and lower limit so that central patch is relatively weak ($|\alpha|$ small) and has distinct non-circular boundary or develops corners, tips as shown in Figures 2.4 and 2.5, then the central patch is linearly unstable. The kinks in the growth rate of the instability of the same-signed solution region in Figure 2.8(a) indicates the transition from one instability mechanism to another. This is especially evident for case $m = 5$ (i.e '5+1' equilibria) shown by the thick line where a small linear stable region resides in-between two separate linearly unstable regions. The possible different mechanisms are illustrated later when discussing the time-dependent evolution. The opposite-signed equilibria have only one linear instability region which indicates these are more stable structures than their same-signed

counterparts. Figure 2.8(a,b) also reveal that same-signed equilibria have generally smaller linearly stable region than opposite-signed equilibria. Increasing the number of satellite point vortices makes the central patch more stable for both same and opposite-signed equilibria. However, increasing the number of satellite point vortices will eventually bring in the circular instability in which the polygonally arranged satellite vortices become unstable (see Morikawa and Swenson (1971)).

2.4 'm+1' multipolar vortex equilibria

Now consider the '$m+1$' multipolar vortex equilibria in which a central patch is surrounded by m identical satellite patches (see Figure 2.3(b)). This configuration has one degree of freedom more than the '$m+1$' point vortex - vortex patch equilibria: two characteristic radii R_1^c, R_{N+1}^c for the central patch, two boundary points corresponding to R_1^s, R_{P+1}^s for the satellite patches and their respective vorticities ω_c, ω_s (or their circulations Γ_c, Γ_s). Here superscripts and subscripts c, s refers to variables for central patch and satellite patches. Symmetry considerations dictate the central patch must have m-fold symmetry and the satellite patches having mirror symmetry, so only discretized points on fundamental sectors of the vortex patch boundaries need be considered in the numerical computation. Let $N+1$ be the number of points on a $1/2m$ section of the central patch and $P+1$ be the number of points on one half of the symmetric boundary of a satellite patch. These boundaries are discretized relative to the 'centre' of individual patches with evenly spaced θ as in Section 2.2.1.

As in the case of '$m+1$' point vortex - vortex patch equilibria there exist two distinct families of solutions: one with a central patch having opposite-signed vorticity to the satellite patches, the other with all patches having the same-signed vorticity. Previous results in Polvani and Carton (1990) and Morel and Carton (1994)

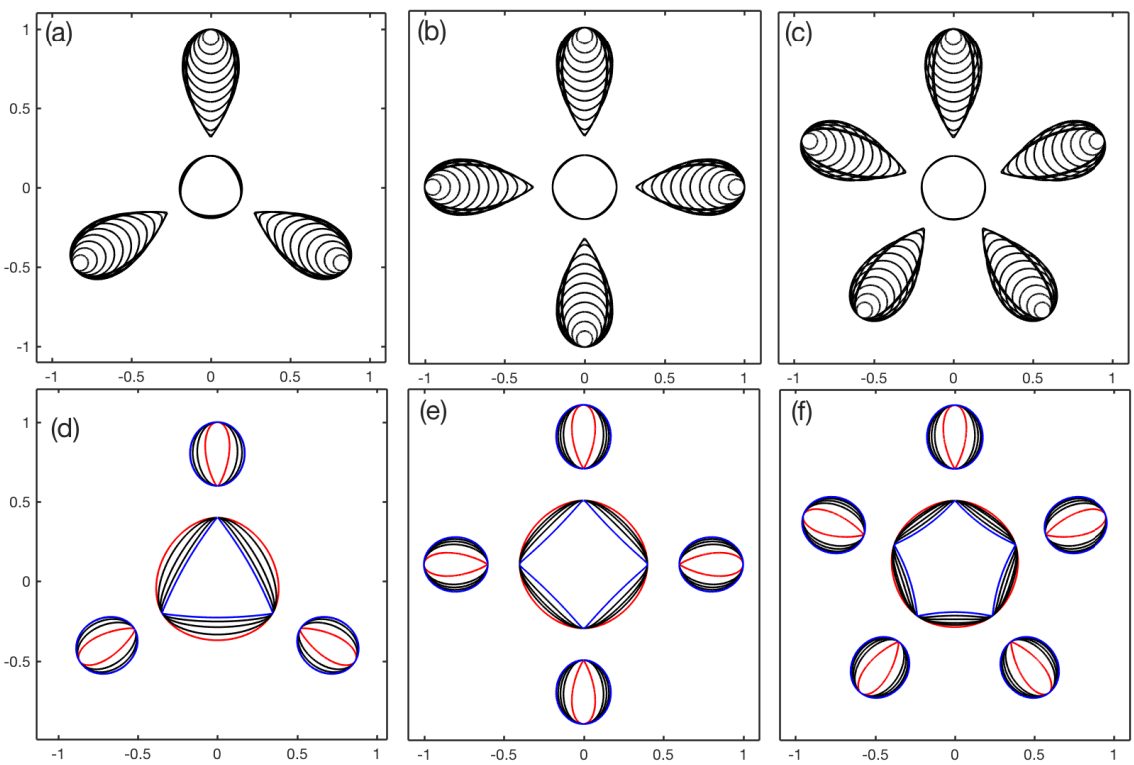

Figure 2.9: Family of solutions of same-signed multipolar vortex equilibria with 3,4,5-fold symmetry. For (a,b,c) the families have $a_1 = 0.2$, $b_2 = 1$, $\omega_c = 1$, $\omega_s = 1$ with decreasing values of b_1 from 0.9, so that satellite patches increase in size towards limiting states. (a) Limiting value $b_1 = 0.316$. (b) Limiting value $b_1 = 0.32$. (c) Limiting value $b_1 = 0.314$. For (d,e,f), the families have $a_1 = 0.4$, $b_1 = 0.6$, $b_2 = 1$, $\omega_c = 1$ with decreasing values of α corresponding to weaker central patch and a boundary tending to limiting states with corners. (d) α from 7 to a limiting value 0.75. (e) α from 7.5 to a limiting value 0.8. (f) α from 7.5 to a limiting value 0.8.

exist for opposite-signed multipolar vortex equilibria for the special case of total total zero circulation. The same-signed multipolar vortex equilibria obtained here are new, as are the opposite-signed equilibria with non-zero total circulation. Together they give a complete class of '$m+1$' multipolar vortex equilibria. Different modified WOZ methods have been used here for computations: one approach prescribes $a_1, b_1, b_2, \omega_c, \omega_s$ (see Figure 2.3) as in Polvani and Carton (1990) and Morel and Carton (1994); another prescribes $a_1, a_2, b_2, \omega_c, \omega_s$ (or the circulations Γ_c, Γ_s in place of their strengths). This latter approach prescribes two characteristic radii of the central patch while relaxing the constraint on the inner boundary point b_1 of satellite patches. A further approach employed here prescribes $a_1, a_2, b_1, b_2, \omega_c$ (or α the circulation ratio) and has proved effective in finding new finite area vortex equilibria. These different methods have been crossed-check and found to agree with each other.

Equilibria sought by prescribing $a_1, a_2, b_1, b_2, \omega_c$ means that ω_s has to be determined. The central and satellite patches are discretized with boundary points R_k^c, $2 \le k \le N$, and R_k^s, $2 \le k \le P$, respectively, such that boundary points are evenly spaced θ in polar coordinates. $R_1^c, R_{N+1}^c, R_1^s, R_{P+1}^s$ are fixed. These radii are defined relative to the relevant patch 'centre', which is taken to be origin for central patch and the radial mid point of the satellite patches. An initial boundary profile in the form of (2.19) is used for the central patch and a circle used for satellite patches. The corresponding modifications for updating the boundary points is given in Section 2.2.1, the difference here being that there are two functions $F_{k+1/2}^c$ and $F_{k+1/2}^s$ defined as in (2.13) for two sets of boundary points which are used in (2.14) to update boundary points. In order to find $F_{k+1/2}^c$ and $F_{k+1/2}^s$, at the n-th iteration the vorticity ω_s and Ω are updated using boundary conditions (2.15) on two separate boundaries. These two equations are coupled linear equations in ω_s, Ω and, after

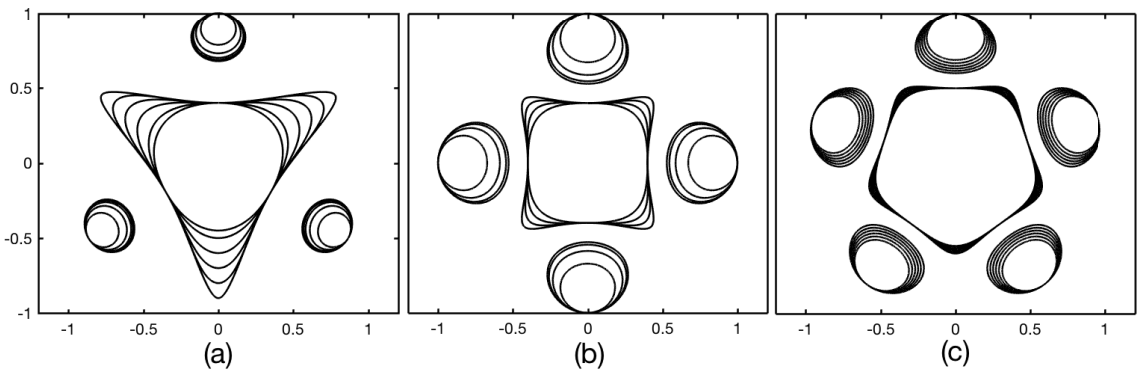

Figure 2.10: Opposite-signed multipolar equilibria computed by prescribing a_1, a_2, b_2, ω_c, ω_s defined in Figure 2.3(b), family of solutions corresponds to various values of a_2 with other parameters fixed. (a) '3+1' equilibria with $a_1 = 0.4$, $a_2 = 0.9$, 0.8, 0.7, 0.6, 0.5, 0.45. $b_2 = 1$, $\omega_c = 1$, $\omega_s = -4$. (b) '4+1' equilibria with $a_1 = 0.4$, $a_2 = 0.6$, 0.55, 0.5, 0.45. $b_2 = 1$, $\omega_c = 1$, $\omega_s = -4$. (c) '5+1' equilibria with $a_1 = 0.5$, $a_2 = 0.6$, 0.59, 0.58, 0.57, 0.56, 0.55. $b_2 = 1$, $\omega_c = 1$, $\omega_s = -3.5$

splitting the velocities due to contribution of different patches, they give

$$\begin{aligned}
\omega_c \sum_{k=1}^{N+1} [u_{k+1/2}^{(cc)} \Delta y_k^c - v_{k+1/2}^{(cc)} \Delta x_k^c] + \omega_s \sum_{k=1}^{N+1} [u_{k+1/2}^{(cs)} \Delta y_k^c - v_{k+1/2}^{(cs)} \Delta x_k^c] &= \frac{\Omega}{2}(a_1^2 - a_2^2), \\
\omega_c \sum_{k=1}^{P+1} [u_{k+1/2}^{(sc)} \Delta y_k^s - v_{k+1/2}^{(sc)} \Delta x_k^s] + \omega_s \sum_{k=1}^{P+1} [u_{k+1/2}^{(ss)} \Delta y_k^s - v_{k+1/2}^{(ss)} \Delta x_k^s] &= \frac{\Omega}{2}(b_1^2 - b_2^2),
\end{aligned} \tag{2.29}$$

where $(x_k^c, y_k^c), (x_k^s, y_k^s)$ are the boundary points on central patch and satellite patches. (2.29) is solved for ω_s, Ω.

The same procedure can be applied to find equilibria with more than two sets of identical vortex patches by prescribing two characteristic radial points of each patch along with vortex strength of one of the patch sets. For example, with 3 sets of patches in an equilibrium, three sections of boundary points need to be considered and correspondingly three $F_{k+1/2}$ for each boundary must be computed. The equivalence of (2.29) then becomes three linear equations in the vorticity strengths of two other sets of vortex patches and Ω.

2.4.1 Numerical results and discussions

The numerical solutions reveal two limiting behaviours for each distinct family of '$m+1$' multipolar vortex equilibria, dependent on the relative vorticity strengths of the central patch to the satellite patches. One way to illustrate the limiting behaviours is by prescribing the same characteristic radii a_1, b_1, b_2 with various circulation ratios of patches as shown in Figure 2.9(d,e,f) for same-signed '$m+1$' multipolar vortex equilibria. In this case the two limiting states are evident by decreasing the circulation ratio α. When α is large and at its maximum, the central patch is relatively strong hence has near circular shape while the satellite patches have oval shapes with pointy tips close to the central patch. When α decreases towards a minimum, the central patch becomes relatively weak and eventually attains corners on its boundary while the satellite patches are relatively strong and have near elliptical shape. Another way to illustrate the limiting behaviour is by varying one characteristic radius: for example, Figure 2.9(a,b,c) gives equilibria with increasing sizes of satellite patches by prescribing decreasing values of b_1. Similar limiting m-polygon co-rotating patches as in Figure 2.9(a,b,c) in the absence of central patch have been computed by Dritschel (1985).

The opposite-signed '$m+1$' equilibria are expected to have two limiting behaviours, one with satellite patches approaching a limiting state that requires more sophisticated numerical treatment than the one used here, the other with the central patch approaching a limiting state. This is demonstrated in Figure 2.10: for sufficiently large central patch, the limiting state central patch acquires 'tips' on its boundary. A common feature for opposite-signed equilibria is that the satellite patches flatten against the central patch as indicated in Figure 2.10.

The streamline plots in Figure 2.11 and Figure 2.12 for multipolar vortex equilibria of 3,4,5 symmetries reveal different circulation regions. Figure 2.12 has arrows added to indicate the flow directions. These streamlines are produced by time ad-

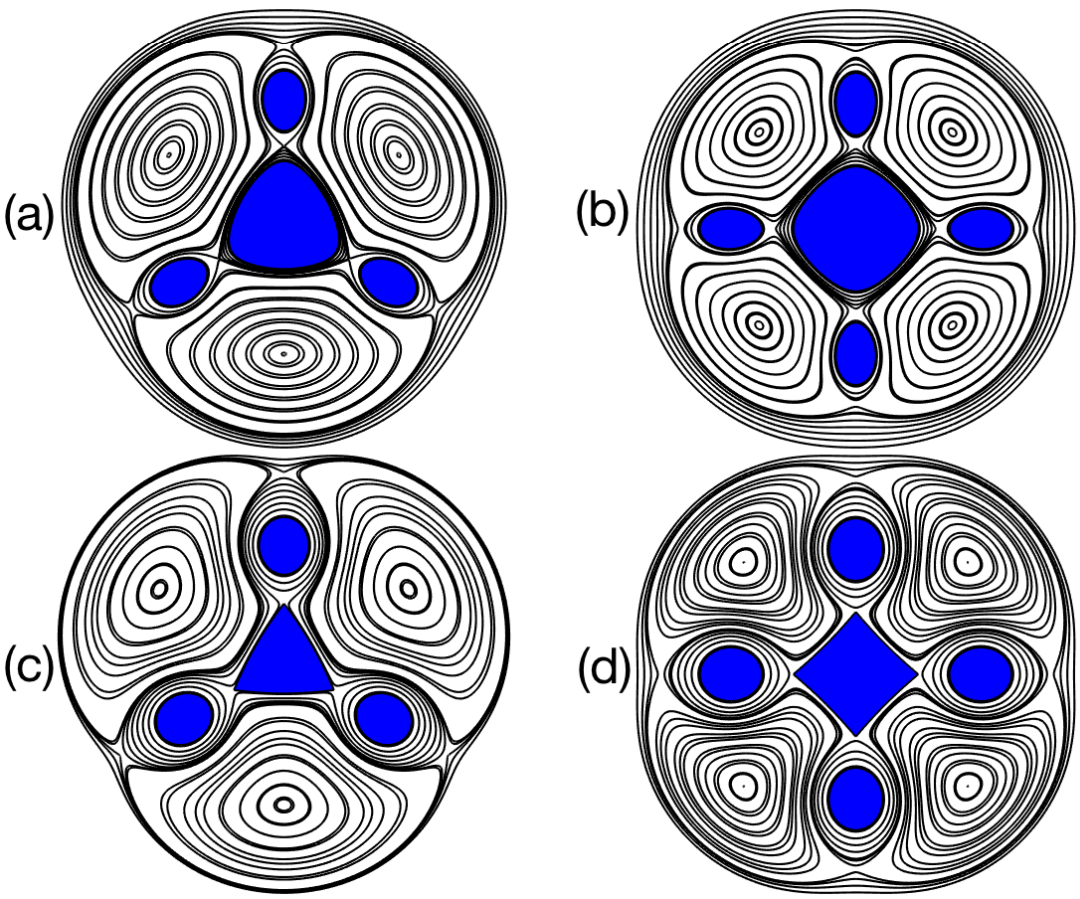

Figure 2.11: Streamline plots of same-signed multipolar equilibria with the shaded regions being the vortex patches having same-signed vorticity. (a) '3+1' equilibrium with $a_1 = 0.4$, $b_1 = 0.6$, $b_2 = 1$, $\omega_c = 1$, $\omega_s = 2$. (b) '4+1' equilibrium with $a_1 = 0.4$, $b_1 = 0.6$, $b_2 = 1$, $\omega_c = 1$, $\omega_s = 2$. (c) '3+1' equilibrium with $a_1 = 0.4$, $b_1 = 0.6$, $b_2 = 1$, $\omega_c = 1$, $\omega_s = 3.077$. (d) '4+1' equilibrium with $a_1 = 0.4$, $b_1 = 0.6$, $b_2 = 1$, $\omega_c = 1$, $\omega_s = 3.77$.

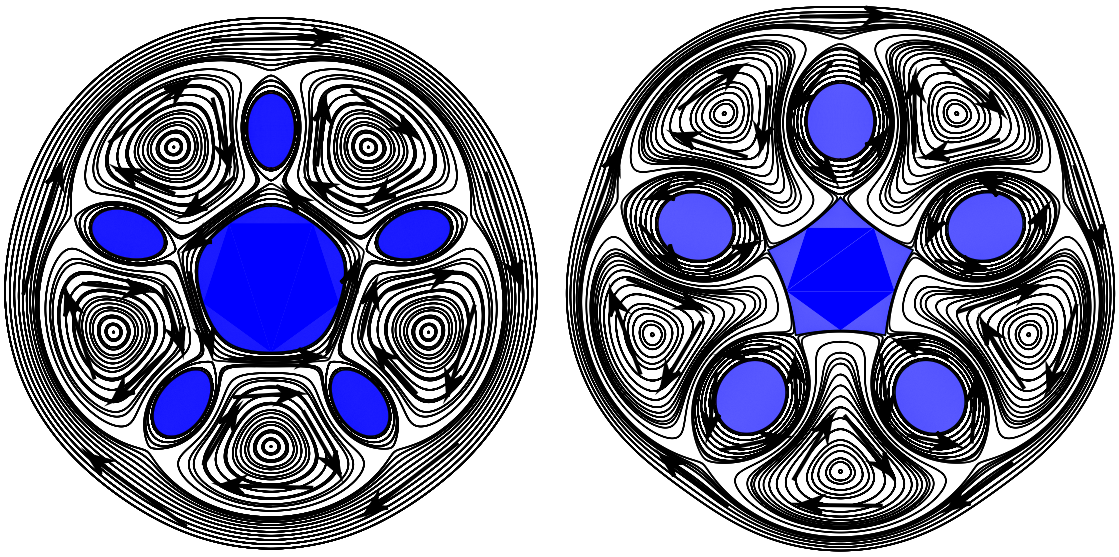

Figure 2.12: Streamline plots of '5+1' same-signed multipolar equilibria with the shaded regions being the vortex patches having same-signed vorticity. Arrows are added to indicate direction of flows. (a) $a_1 = 0.4$, $b_1 = 0.6$, $b_2 = 1$, $\omega_c = 1$, $\omega_s = 2$. (b) $a_1 = 0.4$, $b_1 = 0.6$, $b_2 = 1$, $\omega_c = 1$, $\omega_s = 3.922$.

vancing fluid points outside the patches using a standard 4th order Runge-Kutta scheme. In both example there exists unstable stagnation points between the central patch and the satellite patches due to the opposing flows produced by them. When the central patch tends to its limiting state, these stagnation points meet the corners of the central patch, see Figure 2.12(b). When the satellite patches tend to their limiting states, these stagnation points meet the tips of the satellite patches (not shown). Stable stagnation points are also evident in Figure 2.12. New equilibria can, in principle, be computed by 'growing' sets of satellite patches of either positive or negative vorticity at such stable stagnation points. Indeed, the '$m+1$' multipolar vortex equilibria themselves can be seen as the result of 'growing' a central patch of either sign from existing 'm'-polygonal co-rotating equilibria. Numerical computations of new equilibria by placing point vortices at the stable stagnation points of a '$m+1$' multipolar vortex equilibria has been done but not included here.

2.4.2 Fully non-linear evolutions

In this section the time-dependent behaviour of the equilibria is investigated using contour surgery (see Dritschel (1988)) that allows vortex filamentation and merging. This enables another way to examine the stability of the equilibria computed here. For all evolutions hereafter, the cut-off scale used in contour surgery that allows breaking and merging of patches is chosen to be $\mu = 0.1$ and time step of integration is chosen to be $dt = 0.05$.

A simple configuration involving patches is the '2+1' equilibrium families. First note that in the '2+1' equilibria, all the patches have their centre of vorticity on a straight line as in Figure 2.13. These '2+1' equilibria are generally unstable: an unstable same-signed '2+1' equilibria leads to central patch being drawn towards one of the satellite patches, and unstable opposite-signed '2+1' equilibria leads to the central patch pairing up with one of satellite patches to form a self-propagating dipole which propagates away leaving the remaining patch behind. Figure 2.13(a) shows evolution of an opposite-signed '2+1' equilibrium in which the central patch (the dashed patch) is displaced a distance 0.1 towards upper satellite patch, the central patch pair up with upper satellite patch and propagate away leaving the unpaired satellite vortex behind. Figure 2.13(b) shows evolution of a same-signed '2+1' equilibrium in which the central patch (the dashed patch) is again displaced 0.1 towards upper satellite patch, the central patch is drawn towards upper satellite patch and this satellite patch is thrown towards its counter-part patch which then merges into one single patch that subsequently form a rotating pair.

Now consider '$m + 1$' multipolar vortex equilibria when the central patch is at, or near, its limiting state as in Figure 2.14. Figure 2.14(a) shows the evolution of unstable opposite-signed '3+1' equilibria in which the tips send off filaments of vorticity that wrap around the satellite patches, and the central patch eventually gets torn apart. This instability is a result of the flow field being strongest between

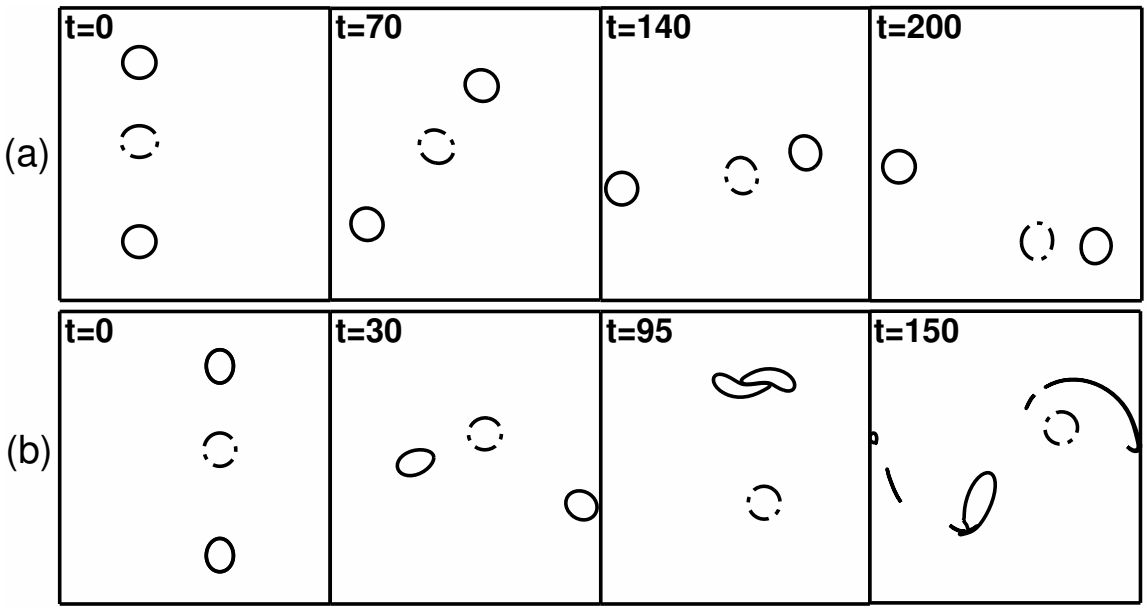

Figure 2.13: (a) Evolution of perturbed opposite-signed '2+1' equilibrium with $a_1 = 0.15$, $b_1 = 0.7$, $b_2 = 1$, $\omega_c = 1$, $\omega_p = -1$. (b) Evolution of same-signed '2+1' equilibrium with prescribed $a_1 = 0.15$, $b_1 = 0.7$, $b_2 = 1$, $\omega_c = 2.5$, $\omega_p = 1$. The dashed lines indicates the displaced central patch.

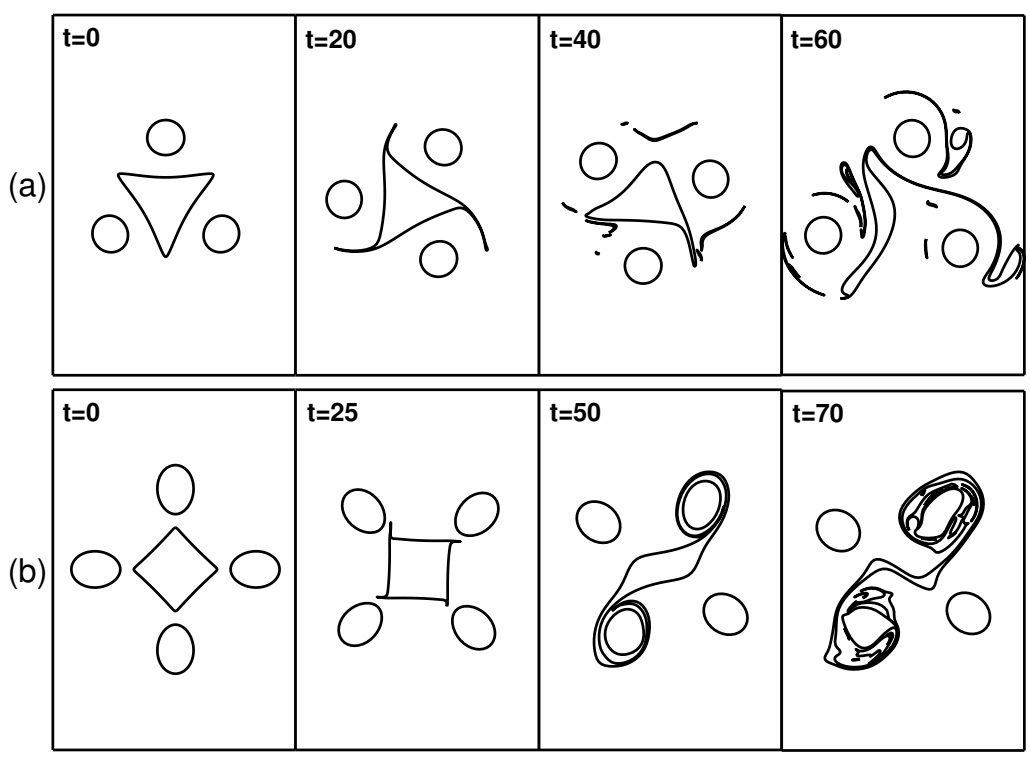

Figure 2.14: (a) Evolution of opposite-signed '3+1' equilibrium with $a_1 = 0.3$, $a_2 = 0.67$, $b_2 = 1$, $\omega_c = 1$, $\omega_s = -4$. (b) Evolution of same-signed '4+1' equilibrium with prescribed $a_1 = 0.4$, $b_1 = 0.53$, $b_2 = 1$, $\omega_c = 1$, $\omega_s = 2.5$.

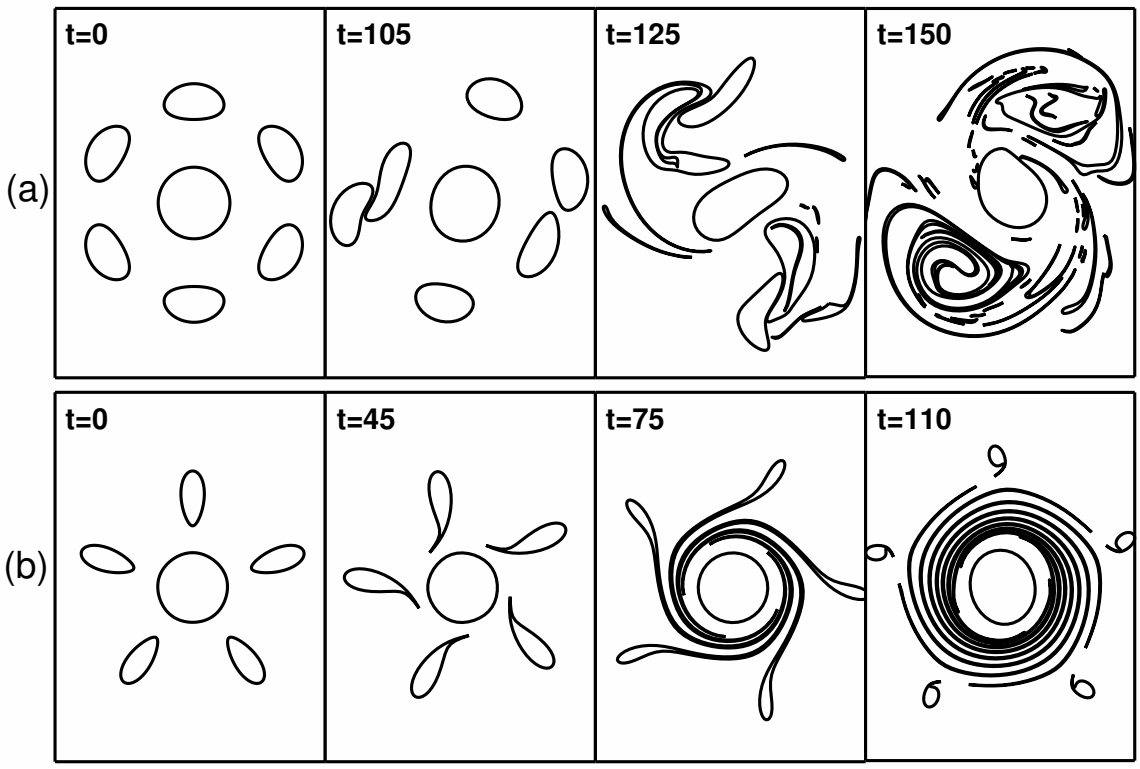

Figure 2.15: (a) Evolution of opposite-signed '6+1' equilibrium with $a_1 = 0.3$, $b_1 = 0.7$, $b_2 = 1$, $\omega_c = 2$, $\omega_s = -1$. (b) Evolution of same-signed '5+1' equilibrium with $a_1 = 0.3$, $b_1 = 0.53$, $b_2 = 1$, $\omega_c = 1$, $\omega_s = 1.1$.

the central patch and satellite patches: a small (linear) perturbation of the central patch boundary is expected to be swept towards the tips resulting in filamentation there. Unstable configurations with smooth boundaries for opposite-signed equilibria for the special case of zero total circulation have been thoroughly studied by Morel and Carton (1994). Figure 2.14(b) shows the evolution of unstable same-signed '4+1' equilibrium in which the instability is manifested through the corners being drawn towards satellite patches. Again this is the result of central patch having largest velocity on its 'flat' side and smallest at corners, an instability mechanism related to the linear stability result in Figure 2.8(a) on the left of the 'kinks'. The right of the 'kinks' of 2.8(a) represents of different instability mechanism: it corresponds to equilibria with a smoother central patch for which an unstable distortion of central patch that tears it apart before any filamentation process.

The other limiting behaviour is when the central patch is relatively strong com-

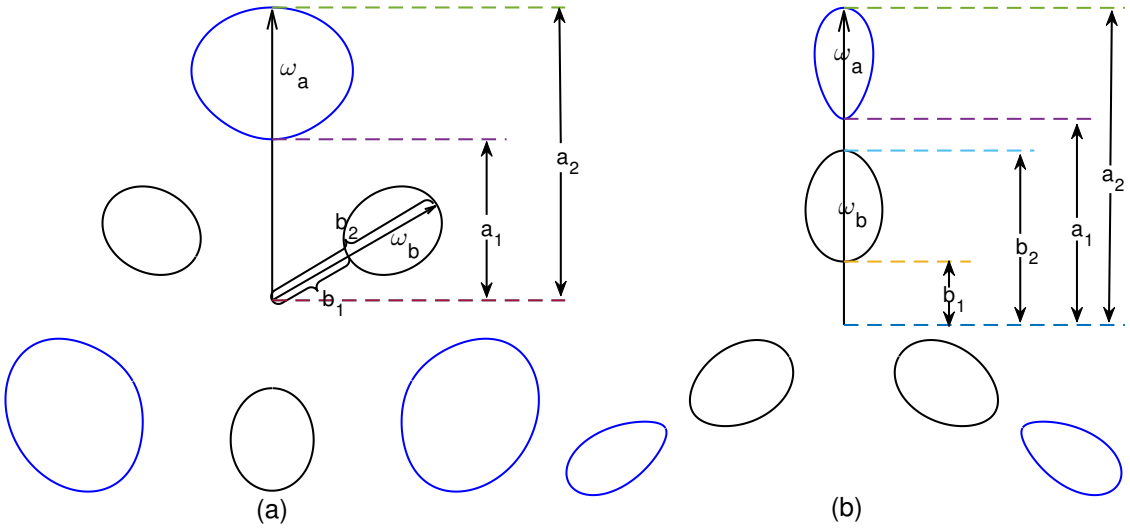

Figure 2.16: Schematic diagram of '3+3' nested polygons with the parameters that defines an equilibrium. (a) Staggered, nested polygons which are out-of-phase by angle $\pi/3$. (b) Aligned, nested polygons. The vorticities ω_a and ω_b can be either same-signed or opposite-signed.

pared to satellite patches ($|\alpha|$ large) i.e. the central patch is near circular. In the opposite-signed equilibrium the satellite patches flatten against central patch as shown in Figure 2.15(a), while in same-signed equilibrium the satellite patches look tear-dropped with tips pointing towards origin as shown in Figure 2.15(b). The investigation of analogous '$m+1$' point vortex equilibria by Morikawa and Swenson (1971) concludes that opposite-signed '$m+1$' point vortex equilibria with a strong central vortex leads to the surrounding m-polygon satellite point vortices becoming unstable. This is also evident for finite area patches e.g. Figure 2.15(a) For same-signed equilibria the satellite patches are also unstable, undergoing filamentation from the tips of satellite patches as shown in Figure 2.15(b). The shed filaments shield the central patch while satellite patches remain but are much reduced in area.

2.5 Nested polygonal multipolar vortex equilibria

An extension to steady rotating m-polygon point vortex equilibria, nested polygonal equilibria, have been found in Aref et al. (2002) which consists of m_1 identical point vortices of circulation Γ_1 centred at the vertices of a regular polygon whose vertices reside on circle of radius R_1 and m_2 identical point vortices of circulation Γ_2 centred at the vertices of a regular polygon whose vertices reside on circle of radius R_2. It has been shown in Aref et al. (2002) that for such equilibria to exist, m_1 must be equal to m_2 (say $m_1 = m_2 = m$), and the polygons can either be in alignment with each other or out-of-phase (referred to here as 'staggered') by angle π/m. Figure 2.16 gives a schematic diagram of the analogous finite area 3-fold symmetric nested-polygons that are uniquely defined by five of the parameters of characteristic radii a_1, a_2, b_1, b_2 and vorticities ω_a, ω_b (or, equivalently, their circulations Γ_a, Γ_b). Figure 2.16(a) gives schematic diagram for staggered nested polygonal equilibria (hereafter staggered '$m + m$' equilibria) and Figure 2.16(b) gives a schematic diagram for polygonal equilibria in alignment (hereafter aligned '$m + m$' equilibria) where m is the number of patches in each polygon. Note all the vortex patches in consideration have reflectional symmetry so only discretized boundary points on half of the patch boundaries needs to be considered in computations. The numerical routine for obtaining equilibria by prescribing two characteristic radii for each set of identical patches (a_1, a_2, b_1, b_2 in this case) and strength of one set of patches, say ω_a, is given at the beginning of Section 2.4.

For either aligned or staggered '$m + m$' equilibria, there again exists two distinct families of solutions: opposite-signed equilibria ($\alpha < 0$ where $\alpha = \Gamma_a/\Gamma_b$ the total circulation ratio), or same-signed equilibria ($\alpha > 0$). The $m = 2, 3$ cases are given here for illustration.

2.5.1 Aligned '$m + m$' equilibria

Families of solutions of same-signed ($\alpha > 0$) aligned 'm+m' equilibria are given in Figure 2.17 for $m = 2, 3$. Two limiting behaviours are revealed by increasing the sizes of polygonal patches: Figure 2.17(a) shows the limiting states with the outer set of patches tending towards tear-dropped shapes pointing towards the origin and Figure 2.17(b) shows the limiting state in which the inner set of patches touch at the origin. Figure 2.17(c,d) gives the family solutions for '3+3' equilibria where Figure 2.17(c) shows the limiting state where inner set of patches become tear-dropped and pointing outwards towards outer polygon patches. Figure 2.17(d) shows limiting state outer set of patches pointing towards the origin. Figure 2.17(e) shows a streamline plot for a '3+3' equilibrium. There exists unstable stagnation points between the aligned patches indicating existence of a possible instability mechanism.

In the opposite-signed case, only a limited range of solutions have been found for aligned equilibria (for $m = 2, 3$ cases) and none for $m \geq 4$. Figure 2.18(a,b) gives examples of '2+2' and '3+3' equilibrium for illustration, as expected the opposite-signed patches flatten against each other. Figure 2.18(e) plots the streamlines for an opposite-signed aligned '3+3' equilibrium.

2.5.2 Staggered '$m + m$' equilibria

The family of solutions with same-signed, staggered '$m + m$' equilibria are given in Figure 2.19 for $m = 2, 3$ in which limiting states are approached by increasing the sizes of one set of the patches. The '2+2' equilibria exhibit different limiting state in comparison to '3+3' equilibria: Figure 2.19(a) shows the limiting state '2+2' equilibria touching at origin, while Figure 2.19(b) shows the limiting state '3+3' having flattened shapes. One can think of these structures as extension to co-rotating vortex pairs and 3-polygon rotating structure by 'growing' extra set of patches at

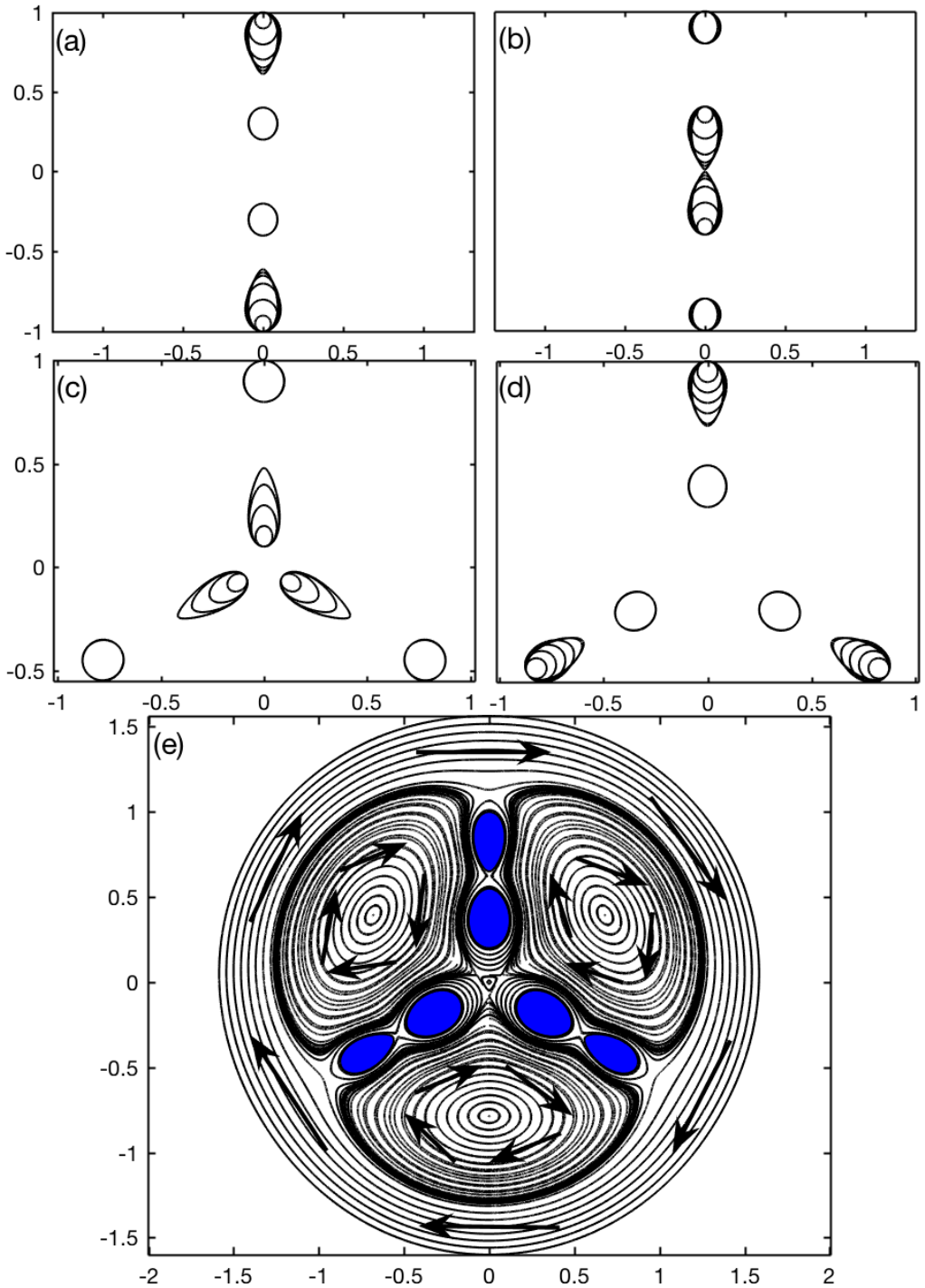

Figure 2.17: Same-signed ($\alpha > 0$), aligned, '$m+m$' equilibria for $m = 2, 3$. (a) '2+2' equilibria with $a_1 = 0.9, 0.8, 0.7, 0.65, 0.63, 0.61$. $a_2 = 1$, $b_1 = 0.2$, $b_2 = 0.4$, $\omega_a = 1$ with $\omega_b = 0.268, 1.24, 2.97, 3.79, 3.98, 4.05$. (b) '2+2' equilibria with $a_1 = 0.8$, $a_2 = 1$, $b_1 = 0.3, 0.2, 0.1, 0.05, 0.03, 0.01, 0.005$. $b_2 = 0.4$, $\omega_a = 1$ with $\omega_b = 9.68, 1.24, 0.37, 0.26, 0.23, 0.23, 0.23$. (c) '3+3' equilibria with $a_1 = 0.8, a_2 = 1, b_1 = 0.1$, $b_2 = 0.2, 0.3, 0.4, 0.48$. $\omega_a = 1$ with $\omega_b = 0.22, 0.15, 0.16, 0.18$. (d) '3+3' equilibria with $a_1 = 0.9, 0.85, 0.8, 0.75, 0.7, 0.68$. $a_2 = 1, b_1 = 0.3$, $b_2 = 0.5$, $\omega_a = 1$ with $\omega_b = 0.27, 0.68, 1.32, 2.15, 2.88, 2.96$. (e) Streamlines for a '3+3' equilibrium with $a_1 = 0.65$, $a_2 = 1$, $b_1 = 0.2$, $b_2 = 0.55$, $\omega_a = 1$, $\omega_b = 1.16$. The shaded regions are the vortex patches having same-signed vorticity. Arrows indicate the direction of flow field.

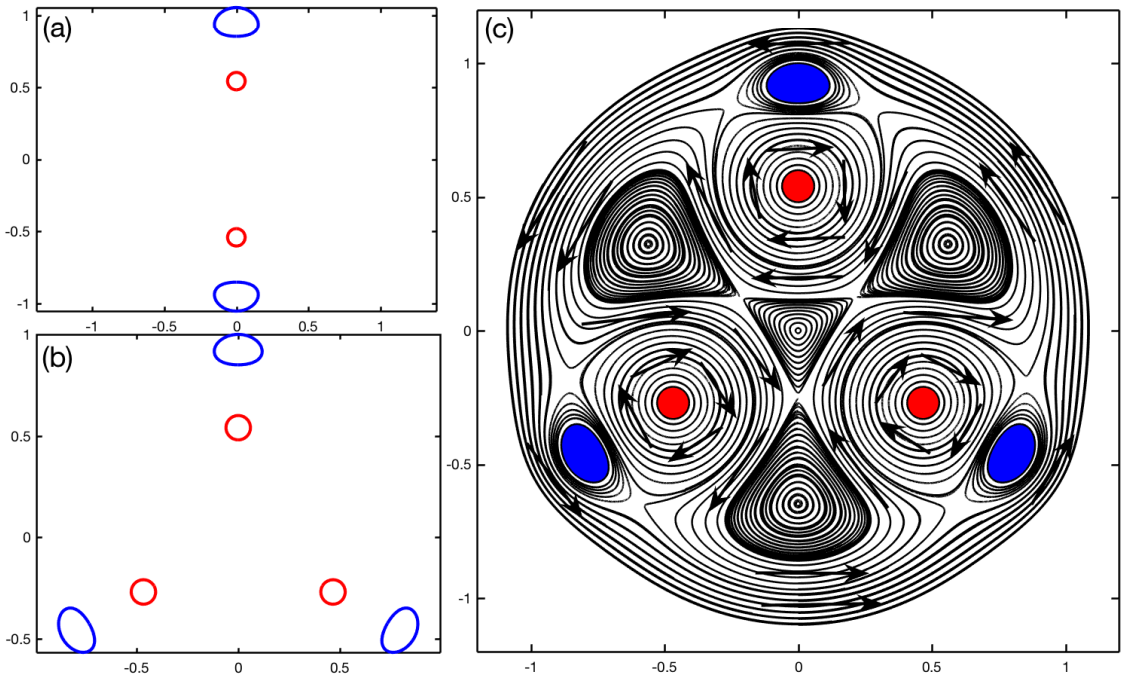

Figure 2.18: Opposite-signed ($\alpha < 0$), aligned, '$m + m$' equilibria. (a) '2+2' equilibrium with $a_1 = 0.85$, $a_2 = 1.05$, $b_1 = 0.48$, $b_2 = 0.6$, $\omega_a = 1$, $\omega_b = -10.29$. (b) '3+3' equilibrium with $a_1 = 0.85$, $a_2 = 1$, $b_1 = 0.48$, $b_2 = 0.6$, $\omega_a = 1$, $\omega_b = -9.72$. (c) Streamlines for the '3+3' equilibrium in (b) with shaded regions being the vortex patches.

the stable stagnation points viewed in rotating frame. The idea of growing vortex patches at stagnation points to generate new, exact, equilibria has been used before by Crowdy and Marshall (2004). Streamlines in Figure 2.19(e) gives details of the flow field in rotating frame for a '3+3' equilibrium.

The opposite-signed staggered '$m + m$' equilibria for $m = 2, 3$ cases have two distinct limiting behaviours as shown in Figure 2.20. Scallop-like near limiting states of the outer set of patches are given in the family in Figure 2.20(a,c). The limiting state of inner set of patches in a '2+2' equilibrium touch at origin as shown in Figure 2.20(b), while '3+3' equilibria have long and thin inner set of patches as shown in Figure 2.20(d). Streamlines in Figure 2.20(e) gives details of the flow field in rotating frame for a '3+3' equilibrium.

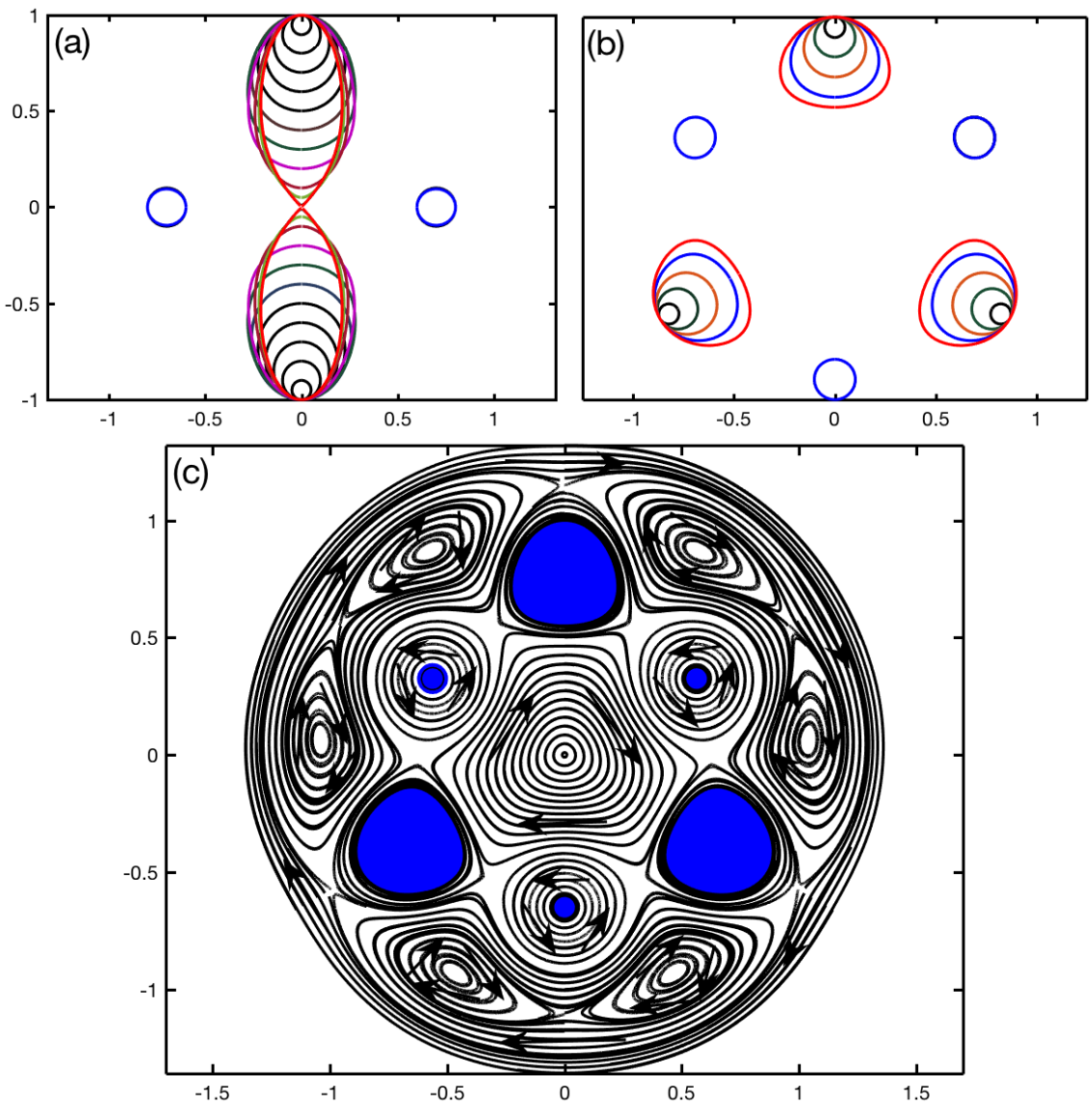

Figure 2.19: Same-signed ($\alpha > 0$) staggered '$m + m$' equilibria. (a) '2+2' equilibria for $a_1 = 0.9, 0.8, 0.7, 0.6, 0.5, 0.4, 0.3, 0.2, 0.1, 0.05, 0.01$. $a_2 = 1$, $b_1 = 0.6$, $b_2 = 0.8$, $\omega_a = 1$ with $\omega_b = 0.53, 1.75, 3.31, 4.98, 6.58, 7.91, 8.59, 8.09, 6.37, 5.43, 5.10$. (b) '3+3' equilibria for $a_1 = 0.9, 0.8, 0.7, 0.6, 0.55$. $a_2 = 1$, $b_1 = 0.7$, $b_2 = 0.9$, $\omega_a = 1$ with $\omega_b = 0.31, 1.13, 2.41, 4.22, 5.50$. (c) Streamlines for a '3+3' equilibrium with $a_1 = 0.55$, $a_2 = 1$, $b_1 = 0.6$, $b_2 = 0.7$ giving $\omega_b = 24.6$. All shaded region are vortex patches having same-signed vorticity.

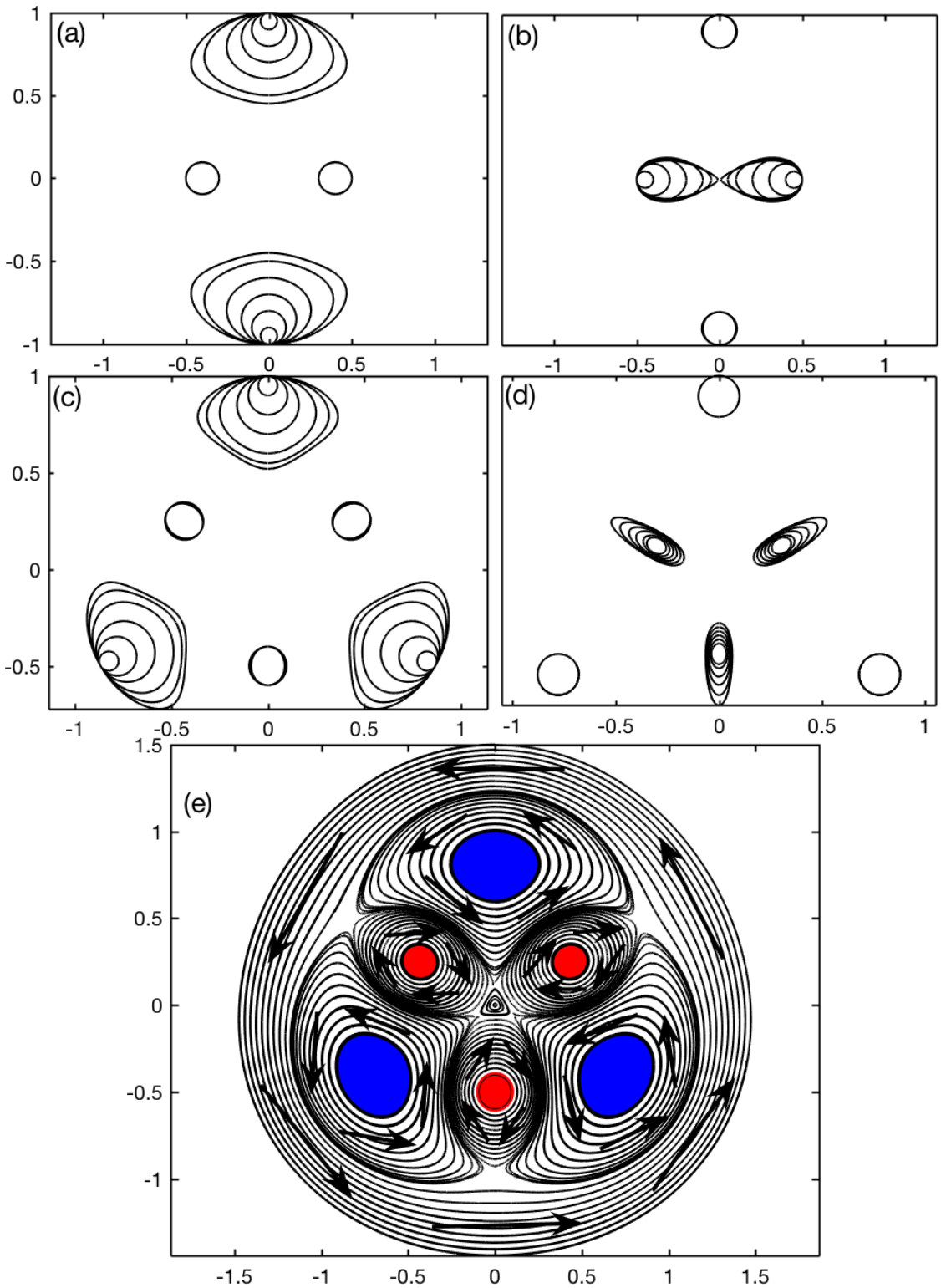

Figure 2.20: Opposite-signed ($\alpha < 0$) staggered '$m + m$' equilibria. (a) '2+2' equilibria for $a_1 = 0.9, 0.8, 0.7, 0.6, 0.5, 0.45$. $a_2 = 1$, $b_1 = 0.3$, $b_2 = 0.5$, $\omega_a = -1$ with $\omega_b = 0.28, 1.47, 4.74, 14.22, 47.93, 103.77$. (b) '2+2' equilibria for $a_1 = 0.8$, $a_2 = 1$, $b_1 = 0.4, 0.3, 0.2, 0.1, 0.05, 0.01$. $b_2 = 0.5$, $\omega_a = -1$ with $\omega_b = 11.73, 1.47, 0.42, 0.18, 0.14, 0.12$. (c) '3+3' equilibria for $a_1 = 0.9, 0.8, 0.7, 0.6, 0.55, 0.52$. $a_2 = 1$, $b_1 = 0.4$, $b_2 = 0.6$, $\omega_a = -1$ with $\omega_b = 0.11, 0.70, 2.97, 14.78, 45.13, 154.89$. (d) '3+3' equilibria for $a_1 = 0.8$, $a_2 = 1$, $b_1 = 0.2, 0.22, 0.24, 0.26, 0.28, 0.30$, $b_2 = 0.6, 0.55, 0.5, 0.46, 0.42, 0.4$, $\omega_a = -1$ with $\omega_b = 0.07, 0.07, 0.07, 0.07, 0.09, 0.15$. (e) Streamlines plot for a '3+3' equilibrium for $a_1 = 0.6$, $a_2 = 1$, $b_1 = 0.4$, $b_2 = 0.6$, $\omega_a = 1$ with $\omega_b = -14.78$. Shaded regions are vortex patches.

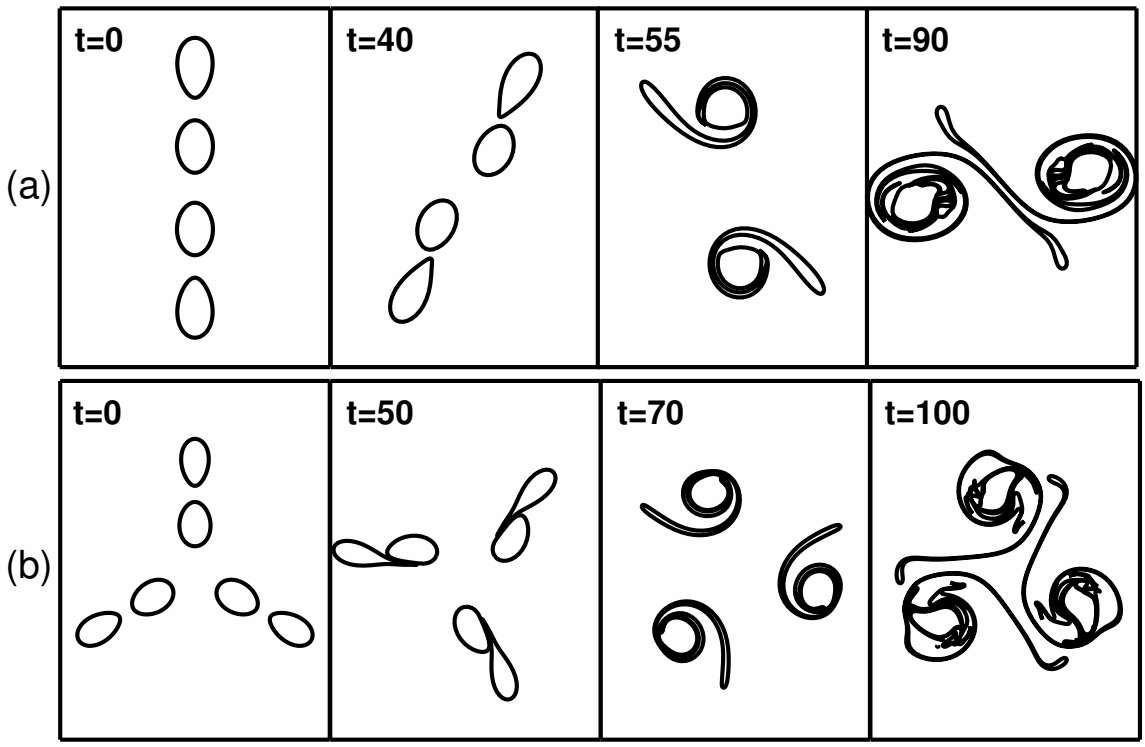

Figure 2.21: Evolution of same-signed aligned '2+2' and '3+3' equilibrium. (a) '2+2' equilibrium with $a_1 = 0.6$, $a_2 = 1$, $b_1 = 0.1$, $b_2 = 0.45$, $\omega_a = 1$ giving convergent $\omega_b = 1.55$. (b) '3+3' equilibrium with $a_1 = 0.65$, $a_2 = 1$, $b_1 = 0.2$, $b_2 = 0.53$ giving convergent $\omega_b = 1.21$.

2.5.3 Fully non-linear evolutions

Stability of the nested polygonal equilibria is explored using time-dependent simulation for the following scenarios: when either set of polygonal patches are at, or near, their limiting states and when the two sets of patches are 'comparable' in sizes and strengths in the sense that they have boundary shapes not too different from circular or ellipse. A summary of some of the general findings is given below:

1. The nested polygonal equilibria are generally less stable than the analogous '$m + 1$' multipolar vortex equilibria. Indeed, in some time-dependent simulations they have been observed to evolve into multipolar equilibria.

2. The '2+2' equilibria are particularly unstable for both aligned and staggered nested polygonal equilibria, '3+3' are the most stable equilibria.

3. The aligned 'm+m' equilibria of either same-signed vorticity or opposite-signed

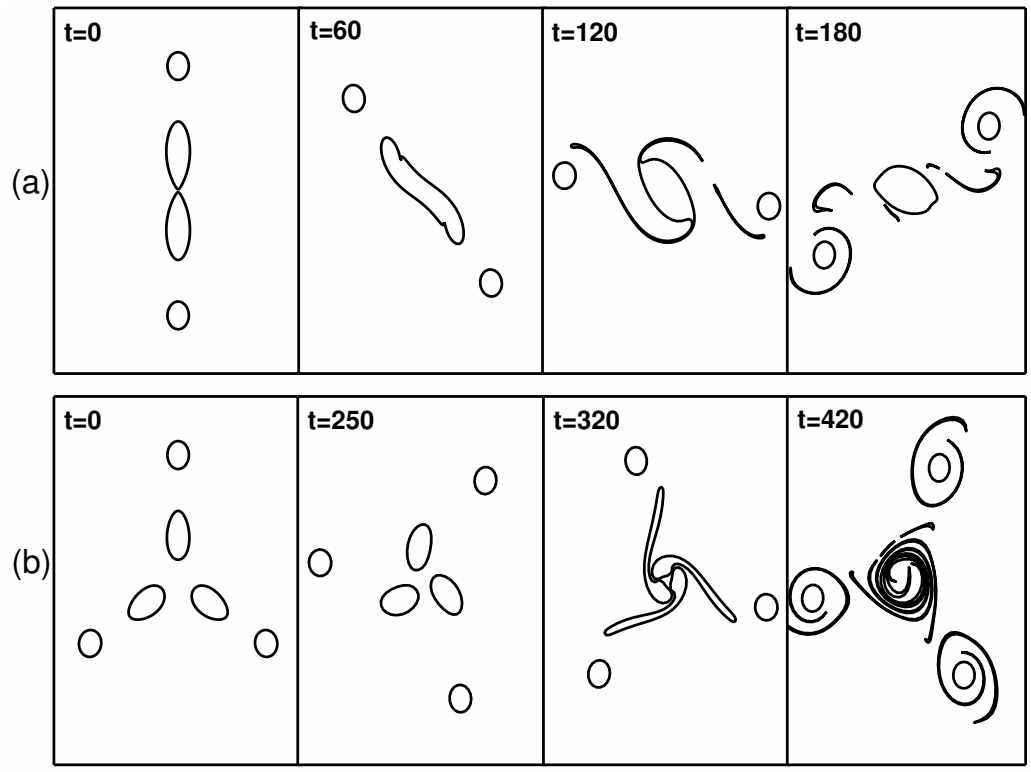

Figure 2.22: Evolution of same-signed aligned '2+2' and '3+3' equilibrium. (a) '2+2' equilibrium with prescribed $a_1 = 0.8$, $a_2 = 1$, $b_1 = 0.01$, $b_2 = 0.5$, $\omega_a = 1$ giving convergent $\omega_b = 0.28$. (b) '3+3' equilibrium with $a_1 = 0.8$, $a_2 = 1$, $b_1 = 0.15$, $b_2 = 0.5$, $\omega_a = 1$ giving convergent $\omega_b = 0.25$.

vorticity are relatively less stable than staggered '$m + m$' equilibria.

The evolution of same-signed, aligned '$m + m$' equilibria for $m = 2, 3$ is shown in Figure 2.21. In both the $m = 2, 3$ cases the outer set of patches are drawn towards the inner set and merge to form a co-rotating pair ($m = 2$) and a tripolar ($m = 3$) rotating structure. However, for equilibria with the inner set of patches close to origin, as shown in Figure 2.22(a), for a '2+2' equilibrium, they merge into a central patch. Figure 2.22(b) shows a similar unstable evolution for the '3+3' equilibrium with the inner set of patches merge to form a central patch. When two sets of patches are of 'comparable' size and having boundaries not too different from circular as shown in Figure 2.23 for a '3+3' equilibrium, the patches drift from alignment and the inner patches contract towards the origin before returning to alignment with outer patches after which the inner patches rotates $2\pi/3$ relative to

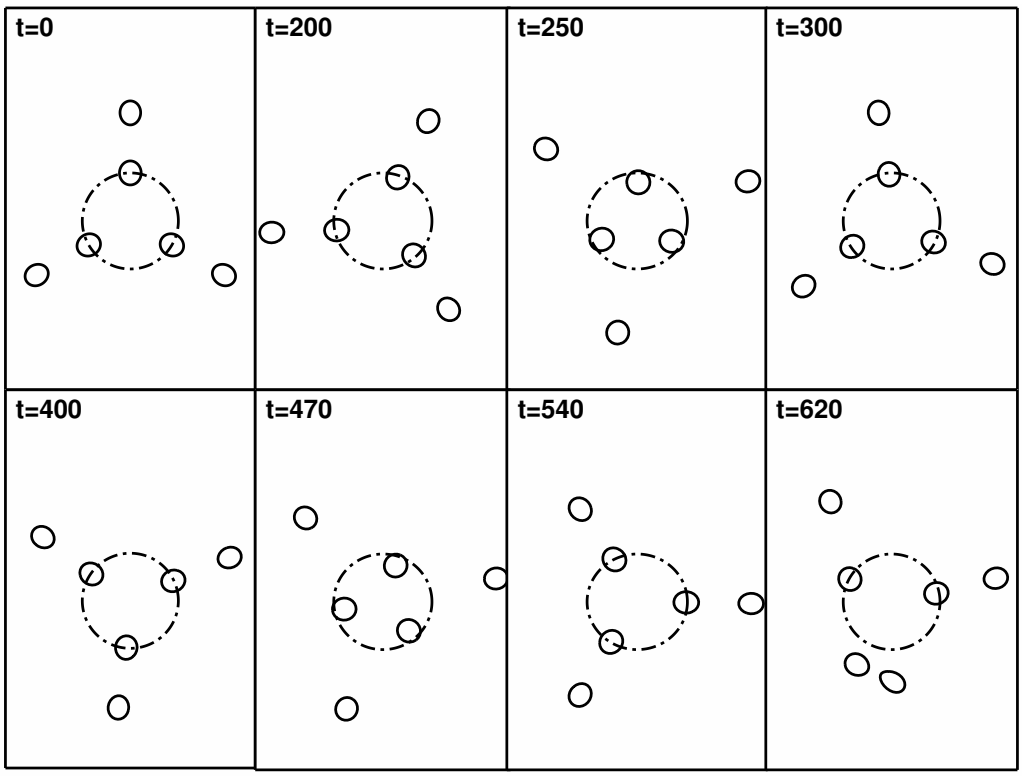

Figure 2.23: Evolution of same-signed aligned '3+3' equilibrium with $b_1 = 0.2$, $b_2 = 0.5$, $a_1 = 0.8$, $a_2 = 1$, $\omega_a = 1$ giving convergent $\omega_b = 1.318$. Dashed circle indicates the radial drift of the inner set of patches.

outer patches. This process occurs twice before the rotating structure is irreversibly destroyed ($t = 620$).

Recall, for opposite-signed, aligned '$m + m$' equilibria, only a limited range of solutions have been found. An opposite-signed equilibrium generally survives a relatively long time in terms of the turnover time for an individual vortex patch and are not shown here.

Staggered '$m + m$' equilibria are relatively more stable than aligned '$m + m$' equilibria. The same-signed, staggered '$m + m$' equilibria bear similar characteristics to the '$2m$'-polygon co-rotating equilibria. The '2+2' staggered equilibria is the most unstable structure. Figure 2.24(a) shows the evolution of same-signed '2+2' equilibrium when one set of polygonal patches, large and close to origin, merge into a central patch which is then eventually destroyed by the other set of patches. But '$m + m$' configuration for $m \geq 3$ with centres of vorticities of each m of the patches

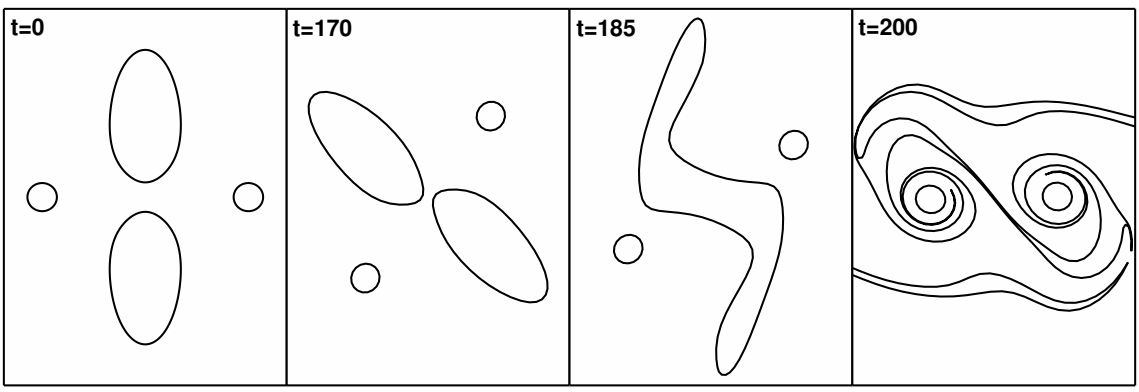

Figure 2.24: (a) Evolution of same-signed, staggered '2+2' equilibrium with $b_1 = 0.6$, $b_2 = 0.8$, $a_1 = 0.1$, $a_2 = 1$, $\omega_a = 1$ with $\omega_b = 6.37$.

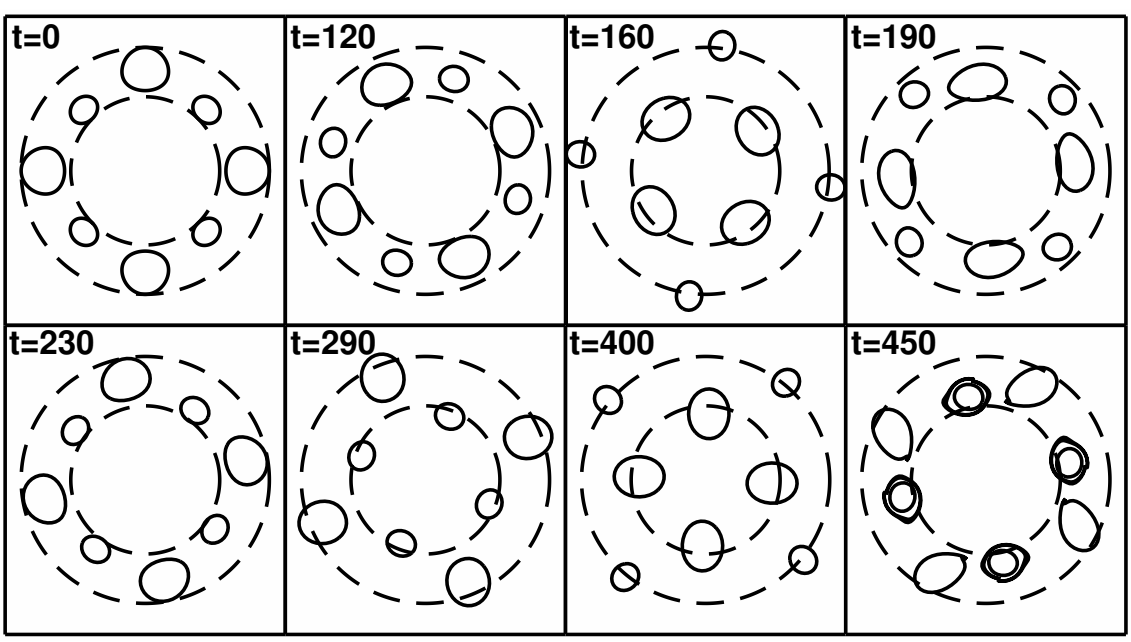

Figure 2.25: Evolution of same-signed staggered '4+4' equilibrium with prescribed $a_1 = 0.65$, $a_2 = 1$, $b_1 = 0.6$, $b_2 = 0.8$, $\omega_a = 1$ giving convergent $\omega_b = 1.95$.

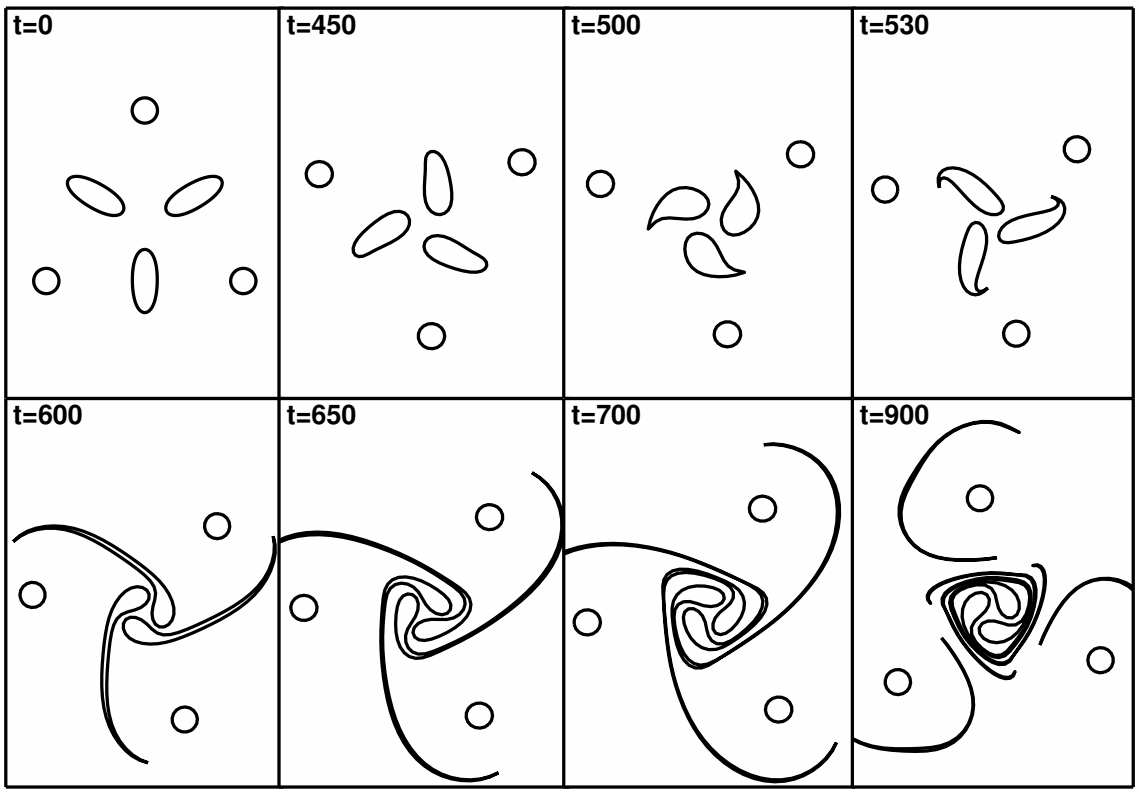

Figure 2.26: Evolution of opposite-signed staggered '3+3' equilibrium with $b_1 = 0.2$, $b_2 = 0.7$, $a_1 = 0.8$, $a_2 = 1$, $\omega_a = 1$ and $\omega_b = -0.09$.

of differing sizes lying on circles not far away from each other prove to be robust even when one set of the patches are large and close to a limiting state. Figure 2.25 shows the evolution of a same-signed, staggered '4+4' equilibrium. Initially, the two sets of polygonal patches adjust radially with the smaller size inner patches moving outwards and large size outer patches contracting inwards such that the overall structure conserves angular momentum. The large size patches are then drawn outwards when they get too close to origin in the meantime two polygonal patches rotate $\pi/2$ relative to the other. The smaller size patches are then in turn drawn towards origin while the larger set move further away. After a second, similar, process the larger patches undergo filamentation which eventually destroys the rotating structure.

The opposite-signed staggered '$m+m$' equilibria with 'comparable' sized patches are robust. When the outer set of polygonal patches are near the limiting states with sector-like boundaries as in Figure 2.20(a,c), these structures prove to be very robust since the sector-like vortex patches are relatively weak in strength hence hold

firmly at their positions in the rotating structure. Near a limiting state instability does eventually set-in as shown in Figure 2.26.

2.6 Summary

Two distinct families of solutions have been computed for '$m+1$' point vortex - vortex patch equilibria, i.e. same-signed equilibria and opposite-signed equilibria. The families have limiting states in which the central patch acquires tips or corners. Linear stability analysis shows that the central patch is most unstable near these limiting states.

The '$m+1$' multipolar vortex equilibria, where finite area satellite patches replace the point vortices, bear many similar properties of the '$m+1$' point vortex - vortex patch equilibria. Two extra limiting behaviours exist when the satellite patches form tips. Time-dependent simulations of these multipolar vortex equilibria show that opposite-signed equilibria are relatively more stable structures than their same-signed counterparts. Various forms of instability are evident including filamentation at tips and corners, vortex pairing to form either same-signed or opposite-signed (propagating) dipoles. In comparison to the '$m+1$' point vortex equilibria, it has been shown that the finite area of the satellite patches plays an important role in the stability of vortex equilibria. In a '$m+1$' multipolar vortex equilibrium, a relatively weak central patch is most susceptible to filamentation and distortion as well as breaking. Increasing the number of satellite patches suppresses the central patch instability but introduces circular instability of the satellite patches especially in opposite-signed equilibria. The circular instability is suppressed in a same-signed '$m+1$' multipolar equilibrium due to the opposing flow in-between central and satellite patches.

The '$m+m$' nested polygonal equilibria consists of aligned or staggered arrange-

ment of vortex patches, each having same-signed and opposite-signed solutions. Various limiting shapes have been found along with their streamlines. These equilibria are typically less stable than the '$m + 1$' multipolar equilibria. In some solution regimes, time-dependent integrations have shown the nested polygonal equilibria evolve into '$m + 1$' vortex equilibria. The same-signed aligned polygonal equilibria are less stable than staggered equilibria, and frequently evolve into m-polygon corotating structures. The opposite-signed aligned '$m + m$' equilibria have a complex flow fields and only a limited range of normalised solutions have been found. A typical unstable mechanism of such equilibria results in opposite-signed vortex patches pairing up and propagating away from their initial location. The staggered polygonal equilibria are more robust structures. Same-signed staggered '$m + m$' equilibria are similar to the $2m$-polygonal equilibria. The opposite-signed staggered polygonal equilibria survive for longer times in time-dependent evolution, but those near limiting states undergo vortex merging, breaking and filamentation.

Chapter 3

Beach vortices of exponential depth with constant PV

3.1 Introduction

Water waves incident on a beach give rise to long-shore currents where energy is lost but momentum is transferred. Wave breaking, bottom friction and turbulent horizontal mixing play an important role in the transport of momentum and sediment in the surf zone. Vortical structures are frequently observed to arise from bores and breaking waves that propagate along or off shore. Evidence of such surf zone eddies is given in Peregrine (1998), including opposite-signed eddies which pair up to form rip currents. A quantitative measure of vorticity generation by bores is also presented there. Some theoretical and numerical considerations (see Nadaoka and Yagi, 1993; Allen et al., 1996; Slinn et al., 1998; Özkan-Haller and Kirby, 1999) show generation and subsequent concentration of vorticity and its propagation under various conditions over barred or uniform sloping beaches. Experimental studies (Sancho and Svendsen, 1998; Oltman-Shay et al., 1989) also demonstrate the existence and propagation of eddies.

The standard theoretical studies of beach vortices use 'radiation stress' for av-

eraged momentum flux introduced by Longuet-Higgins and Stewart (1964). As the surf zone is shallow and typical flow speeds are small compared to the gravity wave speed, the zero Froude number (i.e. rigid lid) approximation is frequently adopted. Hence the alternative theoretical approach adopted here is to use vorticity distribution. Kelvin's circulation theorem means for beach vortices the potential vorticity is conserved. Monopoles and dipoles in constant depth flow have been thoroughly studied using time-dependent integrations, in, for example contour dynamics simulations (Dritschel, 1988). This numerical treatment allows merging, splitting and shedding of vorticity. Motivated by observations, infinitely long steps have been used as a first approximation to represent barred beaches. This choice of topography implies piecewise constant vorticity enabling direct use of Dristchel's contour dynamics method. Johnson et al. (2005) found steadily translating monopoles parallel to step topography, and that these structures are stable. The dynamics of dipole structures have also been considered (see for example Johnson and McDonald, 2004; Hinds et al., 2007a,b) over the step topography.

The present work investigates the two-dimensional monopolar vortex structures over an exponential topography. Such a choice enables both analytical and numerical progress since the Green's function for a point vortex can be found explicitly. A family of steady states is computed numerically. The linear stability of the vortices is considered and time-dependent integrations presented to demonstrate their robustness. An asymptotic approximation of near circular beach vortex in small slope limit has been derived and compared to numerical results. It is clear from works in Johnson et al. (2005) and Bühler and Jacobson (2001) that there are two contributions to the dipole motion: the mutual advection of the vortices and the self advection due to sloping topography. The steady states computed here demonstrate the competition of these two effects. Section 3.2 gives the background and governing equations for this problem. Section 3.3 describes the various numerical routine used

and presents the steady state solutions. Section 3.4 derives an asymptotic approximation for nearly circular beach vortices in the small slope limit. Section 3.5 gives the linear stability analysis of the steady states. Section 3.6 presents time-dependent integrations and a summary of results is given in Section 3.7.

3.2 Background and governing equation

In the rigid-lid limit, volume conservation in the shallow water equations gives

$$\nabla \cdot (H\boldsymbol{u}) = 0, \tag{3.1}$$

where $H(x, y)$ is the given, fixed fluid depth. Thus there exists a volume flux stream-function ψ such that

$$u = -\frac{1}{H}\frac{\partial \psi}{\partial y}, \qquad v = \frac{1}{H}\frac{\partial \psi}{\partial x}. \tag{3.2}$$

The remaining shallow water equation is simply the particle-wise conservation of potential vorticity (PV)

$$\frac{\mathrm{D}q}{\mathrm{D}t} = 0, \tag{3.3}$$

where, in non-rotating flow, the PV is simply $q = \zeta/H$. Here

$$\zeta = (\nabla \times \boldsymbol{u}) \cdot \mathbf{k} = \nabla \cdot (H^{-1}\nabla\psi), \tag{3.4}$$

is the vertical component of the vorticities. The advection operator can be written

$$\frac{\mathrm{D}q}{\mathrm{D}t} = q_t + \boldsymbol{u} \cdot \nabla q = q_t + H^{-1}\partial(\psi, q), \tag{3.5}$$

where $\partial(\psi, q) = \psi_x q_y - \psi_y q_x$ is the Jacobian. Multiplying (3.5) by H and using (3.1) leads to

$$\zeta_t + \nabla \cdot (Hq\boldsymbol{u}) = 0 \qquad \text{or} \qquad \nabla \cdot (H^{-1}\nabla\psi_t + Hq\boldsymbol{u}) = 0. \tag{3.6}$$

Now consider the simplest beach vortex where the PV is constant (say q_0) inside some finite region $\mathcal{D}$ (bounded by a curve $\mathcal{C}$) and zero outside $\mathcal{D}$. Then

$$\zeta = \nabla \cdot (H^{-1}\nabla\psi) = \begin{cases} q_0 H(x,y), & \text{in } \mathcal{D}, \\ 0, & \text{outside } \mathcal{D}. \end{cases} \tag{3.7}$$

The stream-function ψ is thus given by

$$\psi(x,y) = \int_{\mathcal{D}} q_0 H(x',y') G(x',y',x,y)\, \mathrm{d}x'\, \mathrm{d}y', \tag{3.8}$$

where G is the Green's function satisfying

$$\nabla \cdot (H^{-1}\nabla G) = \delta(x-x')\delta(y-y'). \tag{3.9}$$

3.2.1 Exponential bathymetry

Now consider a beach vortex above the x-independent, exponential depth profile of the form

$$H(x,y) = H_0 \exp(2\beta y), \tag{3.10}$$

where H_0 is the depth at the origin and β the topographic slope. Without loss of generality, the vortex can be taken as centred at the origin. Appendix A shows that the Green's function satisfying (3.9) is

$$G(x',y',x,y) = -\frac{H_0}{2\pi} \exp\left[\beta(y+y')\right] \mathrm{K}_0\left(\beta\sqrt{(x-x')^2+(y-y')^2}\right). \tag{3.11}$$

The streamfunction in (3.8) can then be written as

$$\psi(x,y) = -\frac{q_0 H_0^2}{2\pi} \int_{\mathcal{D}} \exp[\beta(y+3y')] \mathrm{K}_0\left(\beta\sqrt{(x-x')^2+(y-y')^2}\right)\, \mathrm{d}x'\, \mathrm{d}y'. \tag{3.12}$$

Multiplying both sides by $\exp(-4\beta y)$ gives

$$\exp(-4\beta y)\psi(x,y) = -\frac{q_0 H_0^2}{2\pi}\int_{\mathcal{D}} F(x-x',y-y')\,\mathrm{d}x'\,\mathrm{d}y', \tag{3.13}$$

where

$$F(x,y) = \exp(-3\beta y)\mathrm{K}_0\left(\beta\sqrt{x^2+y^2}\right). \tag{3.14}$$

Thus using Green's theorem

$$\begin{pmatrix}\partial x\\ \partial y\end{pmatrix}\underbrace{[\exp(-4\beta y)\psi(x,y)]}_{P(x,y)} = \frac{q_0 H_0^2}{2\pi}\oint_{\partial\mathcal{D}} F(x-x',y-y')\begin{pmatrix}\mathrm{d}y'\\ -\,\mathrm{d}x'\end{pmatrix}, \tag{3.15}$$

introducing $P(x,y) = \exp(-4\beta y)\psi(x,y)$. The derivatives of P are thus simple boundary integrals which can be easily evaluated. The velocities in the form of (3.2) are related to the function $P(x,y)$ as

$$\begin{cases} u = -\frac{1}{H(x,y)}\left[\exp(4\beta y)P_y + 4\beta\psi(x,y)\right] = -\frac{1}{H_0}\exp(2\beta y)P_y - \frac{4\beta}{H_0}\exp(-2\beta y)\psi, \\ v = \frac{1}{H(x,y)}\exp(4\beta y)P_x = \frac{1}{H_0}\exp(2\beta y)P_x. \end{cases} \tag{3.16}$$

3.2.2 Conserved quantities

The beach vortices governed by (3.1) and (3.3) have various conserved quantities, which have been derived in Johnson et al. (2005) and their derivations are included here. Consider a vorticity distribution that vanishes at sufficiently large distances and introduce the circulation

$$\Gamma = \int_{\mathcal{D}} \zeta \mathrm{d}x\mathrm{d}y = \int_{\mathcal{D}} q\mathrm{d}V, \tag{3.17}$$

where the volume element $\mathrm{d}V = H\mathrm{d}x\mathrm{d}y$ and the area integral here and below is taken over a finite region containing the non-zero ζ. Since

$$\frac{\mathrm{d}\Gamma}{\mathrm{d}t} = \int_{\mathcal{D}} \zeta_t \mathrm{d}x\mathrm{d}y = -\int_{\mathcal{D}} \nabla.(\boldsymbol{u}\zeta)\mathrm{d}x\mathrm{d}y = 0, \tag{3.18}$$

the circulation Γ is a constant of the motion.

The other conserved quantity above arbitrary topography is the total kinetic energy of the flow

$$\begin{aligned} 2\mathcal{E} &= \int_{\mathcal{D}} H|\boldsymbol{u}|^2 \mathrm{d}x\mathrm{d}y = \int_{\mathcal{D}} H^{-1}|\nabla\psi|^2 \mathrm{d}x\mathrm{d}y \\ &= \int_{\mathcal{D}} \nabla\cdot\left(\frac{\psi}{H}\nabla\psi\right) - \nabla\cdot\left(\frac{1}{H}\nabla\psi\right)\psi \mathrm{d}x\mathrm{d}y = -\int_{\mathcal{D}} \psi\zeta \mathrm{d}x\mathrm{d}y, \end{aligned} \tag{3.19}$$

provided the velocity field vanishes sufficiently rapidly at large distances. Differentiate with respect to t and multiplying (3.6) by ψ gives

$$\begin{aligned} 2\mathcal{E}_t &= -\int_{\mathcal{D}} \psi\zeta_t \mathrm{d}x\mathrm{d}y \\ &= -\int_{\mathcal{D}} \psi\nabla\cdot(Hq\boldsymbol{u})\mathrm{d}x\mathrm{d}y \\ &= -\int_{\mathcal{D}} \nabla\cdot(Hq\psi\boldsymbol{u}) - Hq\boldsymbol{u}\cdot\nabla\psi \mathrm{d}x\mathrm{d}y \\ &= 0. \end{aligned} \tag{3.20}$$

Hence $\mathcal{E}$ is a constant of motion.

Now consider topography independent of x and introduce

$$Y(y) = \int^y H(y')\mathrm{d}y', \qquad \mathcal{I} = \int_{\mathcal{D}} Y\zeta \mathrm{d}x\mathrm{d}y. \tag{3.21}$$

Then

$$\frac{\mathrm{d}\mathcal{I}}{\mathrm{d}t} = \int_{\mathcal{D}} Y\zeta_t \,\mathrm{d}x\mathrm{d}y = -\int Y\nabla\cdot(\boldsymbol{u}\zeta)\mathrm{d}x\mathrm{d}y = -\int \nabla\cdot(\boldsymbol{u}\zeta Y)\mathrm{d}x\mathrm{d}y + \int \zeta\boldsymbol{u}\cdot\nabla Y\mathrm{d}x\mathrm{d}y. \tag{3.22}$$

The first integral vanishes as $\zeta \to 0$ at large distances and the second gives

$$\frac{\mathrm{d}\mathcal{I}}{\mathrm{d}t} = \int \zeta v H = \int (v_x - u_y) v H = \int \left[\left(\frac{1}{2} v^2 H \right)_x - (uvH)_y + (vH)_y u \right], \tag{3.23}$$

since H is a function of y only. The first two terms vanish as the velocity vanishes at large distances and so by continuity

$$\frac{\mathrm{d}\mathcal{I}}{\mathrm{d}t} = -\int_{\mathcal{D}} (uH)_x u \,\mathrm{d}x\mathrm{d}y = -\int_{\mathcal{D}} (\frac{1}{2}u^2 H)_x \,\mathrm{d}x\mathrm{d}y = 0. \tag{3.24}$$

Hence the quantity $\mathcal{I}$, the impulse of the vorticity distribution, is conserved throughout the motion, for topography independent of x.

Since the depth H cannot vanish in the interior of the flow, Y is a strictly monotonically increasing function of y. Thus

$$Y(y_{min})\Gamma < \mathcal{I} < Y(y_{max})\Gamma, \tag{3.25}$$

where y_{min} and y_{max} are the minimum and maximum extents of the vortex distribution in the y-direction. Again since $Y(y)$ is monotonic, this implies that with given $\mathcal{I}$ and Γ there can be associated a unique value of y, say y_c , given by

$$Y(y_c) = \mathcal{I}/\Gamma, \tag{3.26}$$

with $y_{min} < y_c < y_{max}$ and this quantity remains constant throughout the motion. Thus with any vortex distribution there can be associated a unique centre of vorticity

(x_c, y_c) above x-independent topography where x_c is the usual x-mean

$$x_c = \int x\zeta \mathrm{d}x\mathrm{d}y/\Gamma, \tag{3.27}$$

and y_c is the conserved quantity given by (3.26), lying within the extremes of the vorticity distribution in the y-direction. For the chosen exponential topography, these quantities become (with $x_c = 0$ by symmetry)

$$Y(y) = \frac{H_0}{2\beta}\exp(2\beta y), \qquad \Gamma = -\frac{q_0 H_0}{2\beta}\oint_{\partial D}\exp(2\beta y)\mathrm{d}x, \tag{3.28}$$

$$\mathcal{I} = -\frac{q_0 H_0^2}{8\beta^2}\oint_{\partial D}\exp(4\beta y)\mathrm{d}x, \qquad y_c = \frac{1}{2\beta}\log\left(\frac{1}{2}\frac{\oint_{\partial D}\exp(4\beta y)\mathrm{d}x}{\oint_{\partial D}\exp(2\beta y)\mathrm{d}x}\right). \tag{3.29}$$

3.3 Steadily propagating vortices and numerical procedures

Consider a vortex propagating steadily above exponential topography at speed U in the positive x-direction without change of form. The streamfunction for the flow has the form

$$\Psi(x, y, t) = \psi(x - Ut, y), \tag{3.30}$$

and so satisfies the equation

$$-Uq_x + H^{-1}\partial(\psi, q) = 0, \qquad \text{i.e. } \partial(\psi + \psi_0, q) = 0. \tag{3.31}$$

where the subscripted function

$$\psi_0 = U\int^y H(y')\,\mathrm{d}y' = \frac{UH_0}{2\beta}\exp(2\beta y), \tag{3.32}$$

is the streamfunction for a uniform stream in the negative-x direction. Equation (3.31) implies that isolines of q and $\psi + \psi_0$ coincide in steady flow, i.e. the patch boundary $\partial\mathcal{D}$ is a streamline of the total flow. This means on $\partial\mathcal{D}$ the boundary, $\psi+\psi_0 = A$ for some undetermined constant A. When expressed in terms of $P(x, y) = \exp(-4\beta y)\psi$ this condition becomes

$$\exp(4\beta y)P(x, y) + \frac{UH_0}{2\beta}\exp(2\beta y) = A, \tag{3.33}$$

which implies that

$$P(x, y) = \exp(-4\beta y)\left[A - \frac{UH_0}{2\beta}\exp(2\beta y)\right]. \tag{3.34}$$

Recall that the derivatives P_x, P_y are given by the boundary integrals in (3.15) which can be transformed using integration by parts into

$$\begin{pmatrix} P_x \\ P_y \end{pmatrix} = \frac{q_0 H_0^2}{2\pi}\oint \begin{pmatrix} y - y' \\ -(x - x') \end{pmatrix} \beta \exp(-3\beta(y - y'))\left(3K_0(\beta r)dy' - K_1(\beta r)dr\right). \tag{3.35}$$

No velocity normal to patch boundary in the translating frame means that

$$(u - U)\frac{dy}{ds} - v\frac{dx}{ds} = 0, \tag{3.36}$$

where the velocities (u, v) defined in (3.16) can be written purely in derivatives of function $P(x, y)$ as

$$\begin{cases} u = -\frac{1}{H_0}\exp(2\beta y)P_y - \frac{4\beta}{H_0}\exp(-2\beta y)A + 2U, \\ v = \quad \frac{1}{H_0}\exp(2\beta y)P_x, \end{cases} \tag{3.37}$$

using the fact that $\psi = \exp(4\beta y)P(x, y)$ and (3.34).

To find the steadily translating beach vortex above an exponential depth profile

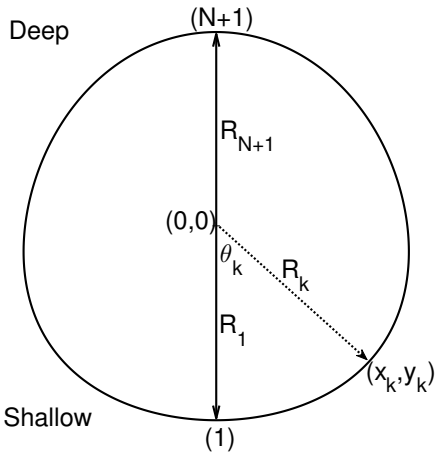

Figure 3.1: The schematic diagram of a steady translating beach vortex where the patch boundary is discretized using polar coordinates with evenly spaced θ. The upper and lower boundary points, characterized by R_1, R_{N+1}, are prescribed and uniquely determine a beach vortex. The potential vorticity within the boundary is a constant q_0 and the depth profile is $H(x, y) = H_0 \exp(2\beta y)$ with deep and shallow side as indicated.

as shown in Figure 3.1, first note such a steady state must have for-and-aft symmetry which means in the numerical treatment that only half of the discretized boundary points need to be considered. Circular patches are used to initialise the computation and boundary points are discretized relative to the centre of circle say at $(0, y_0)$ where usually it is sufficient to take $y_0 = 0$. Hence boundary points can be expressed as

$$(x_k, y_k) = (R_k \cos(\theta_k), R_k \sin(\theta_k) + y_0), \qquad k = 1, 2, \ldots, N + 1. \tag{3.38}$$

where $N + 1$ is the number of boundary points on half of the patch boundary, here $\theta_k = \pi(k-1)/N - \pi/2$ so that (R_1, θ_1) and (R_{N+1}, θ_{N+1}) corresponds to the lower and upper boundary points on the patch boundary as shown in Figure 3.1. At least 300 discretized boundary points are used for computation, that is $N = 300$. Increasing the number of points has negligible effect on the accuracy of computation. The derivatives P_x, P_y defined in (3.35) are evaluated at (x_k, y_k) using the mid-point rule

$$\begin{pmatrix} P_x \\ P_y \end{pmatrix} = \frac{q_0 H_0^2}{2\pi} \beta \sum_{i=1}^{2N} \frac{(y_k - y_{i+1/2}, x_{i+1/2} - x_k)}{\exp(3\beta(y_k - y_{i+1/2}))} \left(3K_0(\beta r_{i+1/2})\Delta y_i - K_1(\beta r_{i+1/2})\Delta r_i\right), \tag{3.39}$$

where $f_{i+1/2} = (f_i + f_{i+1})/2$, the term $\Delta f_i = f_{i+1} - f_i$ and $r_i = |\boldsymbol{x}_k - \boldsymbol{x}_i|$. These derivatives P_x, P_y have also been evaluated from (3.15) using linear interpolation as described in Appendix B. This requires separation of the integrand into an integrable log part and non-singular part where Gaussian quadrature can be applied and tends to be slower and no improvement in accuracy since the discretized velocity is only second order accurate. The evaluations presented below thus use the mid-point discretisation.

To find a unique solution, we seek convergent solutions with prescribed parameters and employ Newton iteration to satisfy the boundary conditions. For example, to find a solution characterized by the two prescribed radii R_1, R_{N+1} for a chosen value of β, or the unique solution characterized by prescribed centre of vorticity y_c defined in (3.26) and total circulation Γ for chosen value of β, or the unique solution characterized by prescribed centre of vorticity y_c and the lower boundary point R_1 for chosen value of β. Three different numerical routines have been used for computations and they are cross-checked with each other and found to agree. The three numerical routines described below are based on streamfunction boundary condition or velocity boundary condition for finding a convergent solution characterized by R_1, R_{N+1}, unique solutions with other prescribed parameters require a minor change to the equations used for Newton's iterations and will be skipped here.

3.3.1 Numerical routine 1

This routine uses the streamfunction boundary condition in (3.34), at the n-th iteration with patch boundary points $\left(x_i^{(n)}, y_i^{(n)}\right), i = 1, \ldots, N+1$. The total derivatives $\left(dx_i^{(n)}/d\theta, dy_i^{(n)}/d\theta\right)$ can be computed using FFT where θ is evenly spaced, the total derivative of $P^{(n)}(r, \theta)$ with respect to θ at $\left(x_i^{(n)}, y_i^{(n)}\right)$ is then

$$\frac{dP_i^{(n)}}{d\theta} = P_x|_{\left(x_i^{(n)}, y_i^{(n)}\right)} \frac{dx_i^{(n)}}{d\theta} + P_y|_{\left(x_i^{(n)}, y_i^{(n)}\right)} \frac{dy_i^{(n)}}{d\theta}, \qquad i, = 1, 2 \ldots, N+1, \tag{3.40}$$

where P_x, P_y at $\left(x_i^{(n)}, y_i^{(n)}\right)$ is evaluated using (3.39). Due to 2π periodicity, inverse FFT leads to

$$\begin{aligned} P_i^{(n)} &= \exp\left(-4\beta y_i^{(n)}\right)\psi\left(x_i^{(n)}, y_i^{(n)}\right) + C \qquad \text{(by definition)} \\ &= \exp\left(-4\beta y_i^{(n)}\right)\left[A - \psi_0\left(x_i^{(n)}, y_i^{(n)}, U\right)\right] + C, \quad i = 1, \ldots, N+1. \end{aligned} \tag{3.41}$$

The constant C arises from the inverse FFT integration. The constant A is determined by equating the total vorticity and the total circulation of the system.

$$\int_{\mathcal{D}} \zeta \mathrm{d}x\mathrm{d}y = \oint_{\partial\mathcal{D}} u \, \mathrm{d}x + v \, \mathrm{d}y. \tag{3.42}$$

Integrating over $\mathcal{D}$ gives the total vorticity as

$$\int_{\mathcal{D}} \zeta \mathrm{d}x\mathrm{d}y = \iint q_0 H(x,y) dx dy = q_0 H_0 \iint \exp(2\beta y) dx dy = -\frac{q_0 H_0}{2\beta} \oint \exp(2\beta y) dx. \tag{3.43}$$

Total circulation of the system, using (3.37), is

$$\oint_{\partial\mathcal{D}} u \, \mathrm{d}x + v \, \mathrm{d}y = \frac{1}{H_0} \oint \exp(2\beta y)(P_x dy - P_y dx) - A\left[\frac{4\beta}{H_0} \oint \exp(-2\beta y) dx\right]. \tag{3.44}$$

where P_x, P_y are evaluated using (3.39). Equating (3.43) and (3.44) gives value A as

$$A = \frac{\oint \exp(2\beta y)(P_x dy - P_y dx) + \frac{q_0 H_0^2}{2\beta} \oint \exp(2\beta y) dx}{4\beta \oint \exp(-2\beta y) dx}. \tag{3.45}$$

Now we seek the unique solution characterised by fixed radii R_1, R_{N+1} (or y_1, y_{N+1}). At these points

$$P(r_1, \theta_1) = \exp(-4\beta y_1^n \quad)\left[A^{n+1} - \frac{U^{(n+1)} H_0}{2\beta} \exp(2\beta y_1^n)\right] + C^{n+1},$$

$$P(r_{N+1},\theta_{N+1}) \;=\; \exp(-4\beta y^n_{N+1})\left[A^{n+1}-\frac{U^{(n+1)}H_0}{2\beta}\exp(2\beta y^n_{N+1})\right]+C^{n+1}.$$

These are coupled equations for U, C with P values given in (3.40) and value of A given in (3.45). Solving these equations gives $U^{(n+1)}, C^{(n+1)}$ which can be inserted into the rest of the equations in (3.41) to give

$$P_i^{(n)}-\exp\left(-4\beta y_i^{(n)}\right)\left[A^{(n+1)}-\frac{U^{(n+1)}H_0}{2\beta}\exp\left(2\beta y_i^{(n)}\right)\right]-C^{(n+1)}=\Delta_i,\quad i=2,\ldots,N, \tag{3.46}$$

where the unknowns are $R_i, (i = 2,\ldots,N)$. A standard Newton iteration then gives $\Delta R_i, (i = 2,\ldots,N)$ and the boundary points are adjusted accordingly. This procedure is repeated until the convergence condition

$$\max(\Delta_i) < 10^{-8}, \qquad \text{for } i = 2,3,\ldots,N, \tag{3.47}$$

is met. To summarise, the steps for this numerical routine is as follows:

1. Compute (x_θ, y_θ) using FFT and find P_θ using (3.40) which gives $P(x, y)$ at each boundary point up to a constant C by inverse FFT.

2. Compute P_x, P_y using (3.39) which are used to update constant A using (3.45) by equating the total vorticity with total circulation.

3. Update U, C using coupled equations for boundary conditions at R_1, R_{N+1}. Then substitute into boundary conditions giving (3.46).

4. Using a standard Newton iteration compute $\Delta R_i, (i = 2,3,\ldots,N)$.

5. Repeat the procedure until convergence.

3.3.2 Numerical routine 2

A weakness of the first procedure is that when computing the Jacobian to find ΔR_i, both U and C have to be adjusted each time a numerical derivative is computed during the update process. To avoid integration that gives rise to the constant C, a second procedure is applied here which also uses streamfunction boundary condition $\psi + \psi_0 = A$. For convenience set $q_0 = 1$ here.

Define $\phi = \psi + \psi_0$ which satisfies on the vortex boundary

$$\phi_i = A, \qquad i = 1, \ldots, N+1.$$

Again two end points are fixed. The value of $A^{(n+1)}$ is first updated using (3.45) following same step before. The idea is to start with $\phi_1 = A$ and integrate for $\phi_i, (i = 2, \ldots, N+1)$. To find the adjustment $\Delta R_i, \Delta U$ such that

$$\phi_i(R_2 + \Delta R_2, \ldots, R_N + \Delta R_N, U + \Delta U) = A, \qquad i = 2, \ldots, N+1, \tag{3.48}$$

use the Taylor expansion and

$$\sum_{j=2}^{N} \frac{\partial \phi_i}{\partial R_j} \Delta R_j + \frac{\partial \phi_i}{\partial U} \Delta U = A - \phi_i, \qquad i = 2, \ldots, N+1, \tag{3.49}$$

given values of $\partial\phi_i/\partial R_j, \partial\phi_i/\partial U, A - \phi_i$ the set of linear equations (3.49) can be solved to give $\Delta R_i, \Delta U$. To compute $\phi_i, i = 2, \ldots, N+1$, use

$$d\phi \simeq \phi_{i+1} - \phi_i = \phi_r dr + \phi_\theta d\theta, \quad i.e. \quad \phi_{i+1} = \phi_i + \bar{\phi}_{ir} dr_i + \bar{\phi}_{i\theta} d\theta_i, \tag{3.50}$$

where $\bar{f}_i = (f_{i+1} + f_i)/2$, to find ϕ_r, ϕ_θ, since $\phi = \psi + \psi_0 = \psi + UH_0 e^{2\beta y}/2\beta$

$$\phi_r = \psi_r + UH_0 \sin\theta e^{2\beta y}, \quad \phi_\theta = \psi_\theta + UH_0 x e^{2\beta y}. \tag{3.51}$$

Now

$$\psi_r = \psi_x \frac{\partial x}{\partial r} + \psi_y \frac{\partial y}{\partial r} = \psi_x \cos\theta + \psi_y \sin\theta, \tag{3.52}$$

$$\psi_\theta = \psi_x \frac{\partial x}{\partial \theta} + \psi_y \frac{\partial y}{\partial \theta} = \psi_y x - \psi_x y. \tag{3.53}$$

Also $\psi + \psi_0 = A$ and the derivatives

$$\psi_x = e^{4\beta y} P_x, \quad \psi_y = e^{4\beta y} P_y + 4\beta A - 2H_0 U e^{2\beta y}. \tag{3.54}$$

Thus

$$\phi_r = e^{4\beta y}(P_x \cos\theta + P_y \sin\theta) - U H_0 \sin\theta e^{2\beta y} + 4\beta A \sin\theta, \tag{3.55}$$

$$\phi_\theta = e^{4\beta y}(P_y x - P_x y) - U H_0 x e^{2\beta y} + 4\beta A x. \tag{3.56}$$

Now an approximation to the Jacobian can be computed by finding $\partial\phi_i/\partial R_j$ by introducing small perturbation to the R_j term and update ϕ_i using (3.50). Finally, $\partial\phi_i/\partial U = e^{2\beta y_i}/2\beta$. The matrix equation is then solved to find the adjustment.

3.3.3 Numerical routine 3

The difficulty with algorithm 2 is having to compute $\phi_i, i = 1, 2, \ldots, N+1$ for every derivative computed in the Jacobian. So the final and most efficient algorithm introduced here uses the velocity boundary condition in (3.36). Given $\left(x_i^{(n)}, y_i^{(n)}\right)$, as before, the constant A is updated first using (3.45). Now using second order accurate discretisation, the boundary condition is expressed as

$$(u_{i+1/2} - U)\Delta y_i - v_{i+1/2}\Delta x_i = 0, \qquad i = 1, \ldots, N, \tag{3.57}$$

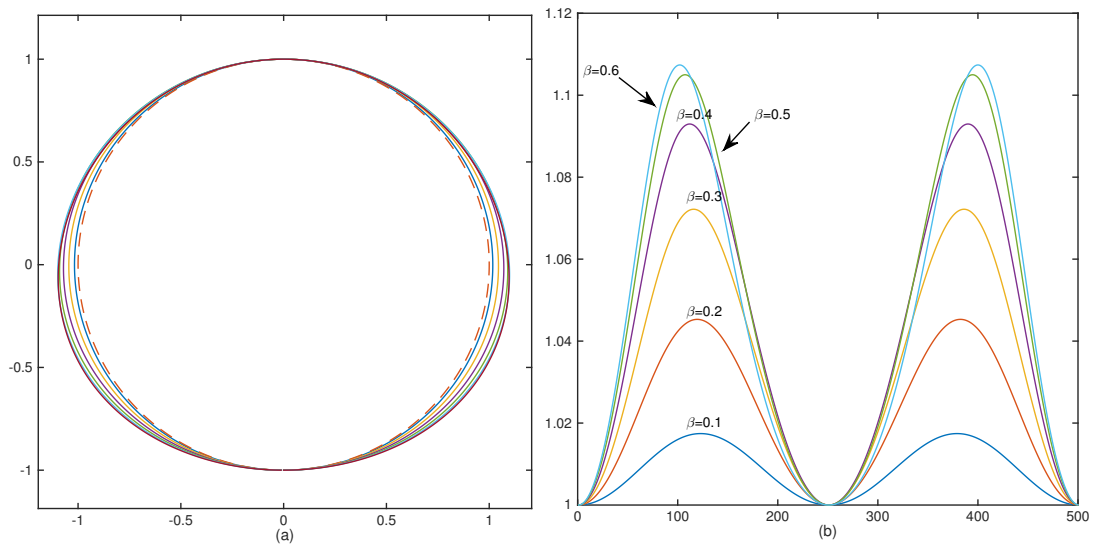

Figure 3.2: (a) Steady state beach vortices for various slopes β=0.1,0.2,...,0.6 that have $R_1 = R_{N+1} = 1$. The dashed line gives the unit circle. (b) The radius of boundary points starting from $N = 1$ ($\theta = -\pi/2$) to $N = 500$ ($\theta = \pi/2$).

where $f_{i+1/2} = (f_{i+1} + f_i)/2$ and $\Delta f_i = f_{i+1} - f_i$. This gives N equations in N unknowns: R_i, $(i = 2, \ldots, N)$ and U. The adjustment ΔR_i is computed and the usual Newton iteration is applied. The steps for this numerical routine is as follows:

1. Compute P_x, P_y using (3.39) and update A.

2. Compute u, v using (3.37).

3. Use (3.57) and standard Newton iteration to find ΔR_i.

Unique solutions correspond to requiring the centre of vorticity be at $y_c = 0$ and are obtained simply by incorporating this extra equation into the Newton iteration.

3.3.4 Steady state solutions

The steadily translating beach vortices presented in Figure 3.2(a) and Figure 3.3(a) were produced numerically by prescribing $R_1 = R_{N+1} = 1$ for various slopes β from 0.1 to 2.4. They constitute a family of solutions and there exists a limiting slope β (around 2.7) beyond which no solutions have been found. Accurate treatment of

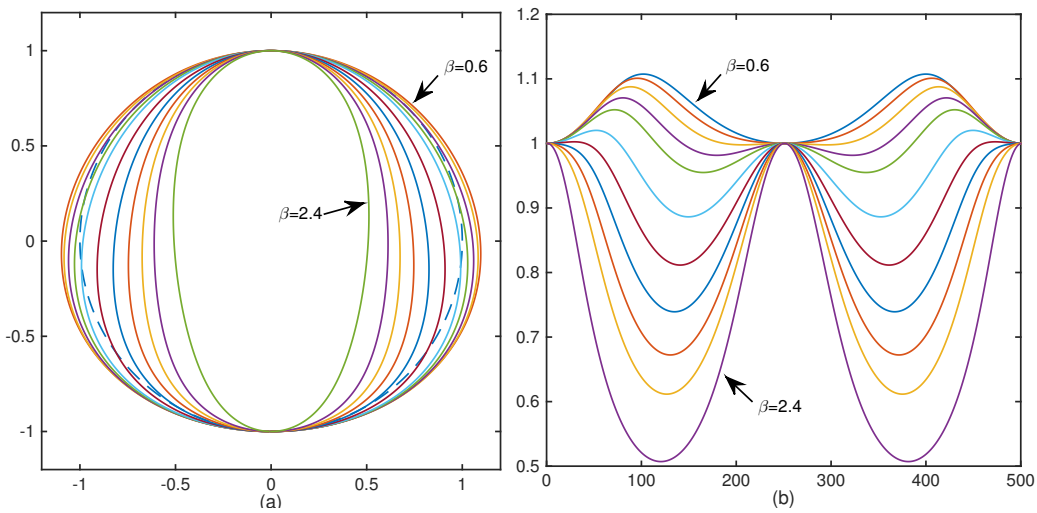

Figure 3.3: (a) Steady state beach vortices for various slopes $\beta = 0.6, 0.7, \ldots, 2.4$ that have $R_1 = R_{N+1} = 1$. The dash line gives the unit circle. (b) The radius of boundary points starting from $N = 1$ to $N = 500$.

limiting state vortex patches would require sophisticated treatment of the high curvature of its boundary and is not considered here. The family of solutions presented here shows different monotonic behaviours separated by a certain critical value of slope β (around 0.6). The behaviours show the competition of two contributing factors to the shapes of beach vortex: self-induction and bottom slope. Figure 3.2(b) and Figure 3.3(b) plot the radius of boundary points around the patch boundary starting at the lowest ($\theta = -\pi/2$) boundary point $N = 1$. Figure 3.2(b) shows the patch boundary expanding outwards from unit circle as β increases from 0.1 towards a critical value around 0.6. The patch boundary then moves inwards as β increases further from 0.6 to 2.4 as shown in Figure 3.3(b). Near the limiting state as shown by the inner most boundary in Figure 3.3(a), the boundary of beach vortex has an oval shape pointing towards the shallow side of water.

Since the centre of vorticity of a beach vortex is a constant of the motion in the translational frame, another natural way to present the family of solutions is to find the steady states with same centre of vorticity y_c to obtain a unique solution, the boundary point defined by R_1 is also prescribed. Increasing the sizes of beach vortices by prescribing larger R_1 reveals a family of solutions as shown in Figure

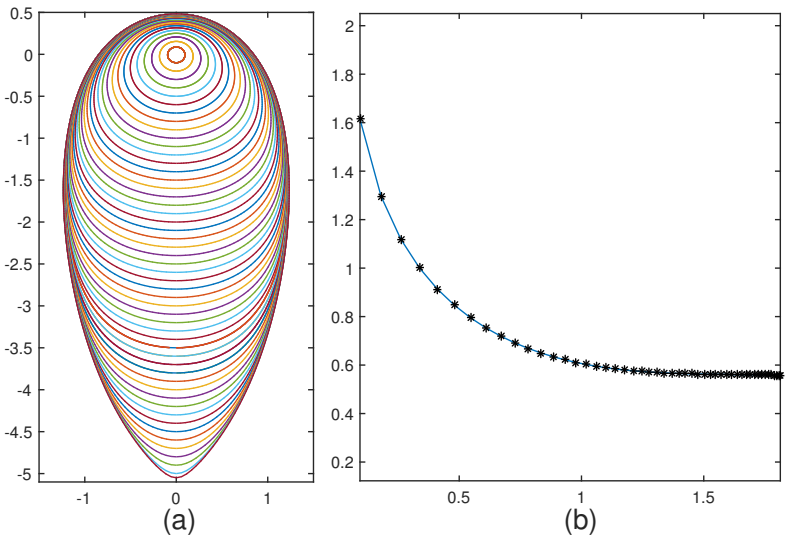

Figure 3.4: (a) Family of steady states with fixed $y_c = 0$ and R_1, the lower boundary point ranging from 0.1 to 5.0 at steps of 0.1, and also $R_1 = 5.05$. (b) the corresponding translational velocities plotted against mean radius $\sqrt{\text{area}/\pi}$ approaches a constant with increasing radius.

3.4(a). Members of the family have $y_c = 0$ and correspond to solutions with lower boundary points R_1 at $0.1, 0.2, \ldots, 5.0, 5.05$. These solutions are normalised to have total circulation π and the constants H_0, β have been set to 1. The potential vorticity q_0 is different for each member of the family. To achieve convergence, the boundary of the vortex is discretized relative to the centre of the circular vortex used to initialise the computation. This is to make sure that the distance between boundary points remain relatively uniform. Figure 3.4(b) plots the corresponding velocity against the mean radius. The steady states expand into shallow water with increasing radius but the translational velocity of the steady states approaches a constant approximately 0.562. This is due to the exponentially decreasing depth on the shallow side: although the sizes of beach vortices have expanded, the change in volume of patch is very small. The patch boundary approaches a limiting state and the local analysis of Overman (1986) suggests that this limiting state has a corner with angle $\pi/2$ at the lowest boundary point.

To reveal more information and visualise the flow field, the streamlines for three members of this family solutions are plotted in Figure 3.5. The streamlines for the

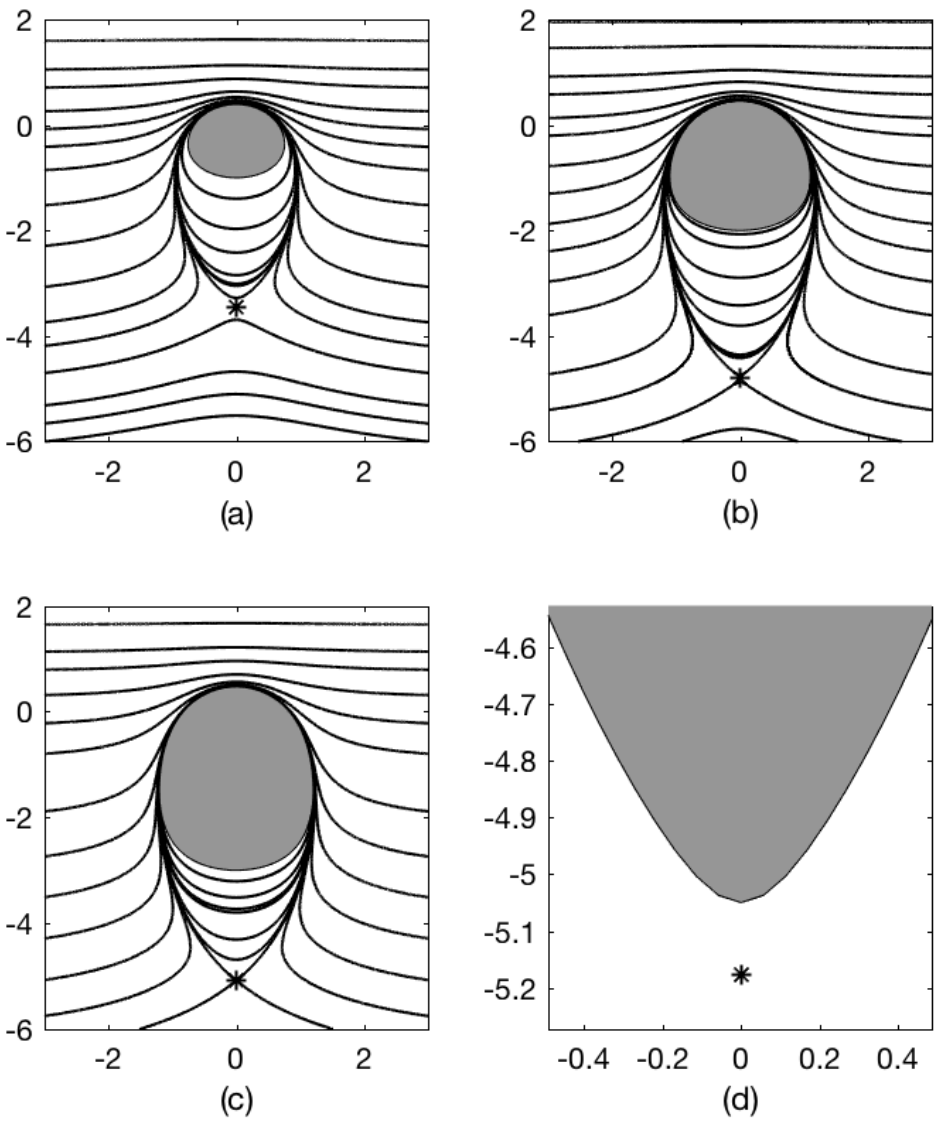

Figure 3.5: Streamlines for three members of the solution family shown in Figure 3.4 in the translational frame. The stars indicate the location of the stagnation points. (a) R_1=1. (b) R_1=2. (c) R_1=3. The shaded region is the beach vortex. (d) A magnification of the most extreme case computed ($R_1 = 5.05$) with the location of the stagnation point.

convergent configurations in the translating frame are drawn using the fact that $P(x_0, y_0) = \exp(-4\beta y_0)\left[A - \frac{UH_0}{2\beta}\exp(2\beta y_0)\right]$ is known on the patch boundary, since A is determined for the particular steady state of interest during computation. The derivatives P_x, P_y at any off boundary points can thus be easily computed and so the values of $P(x, y)$ can be found at points away from the patch by marching from the patch boundary. This then gives ψ. Specifically, polar coordinates are used and the partial derivative is evaluated as

$$\frac{\partial P}{\partial r} = \frac{\partial P}{\partial x}\frac{\partial x}{\partial r} + \frac{\partial P}{\partial y}\frac{\partial y}{\partial r} = \frac{\partial P}{\partial x}\cos\theta + \frac{\partial P}{\partial y}\sin\theta, \tag{3.58}$$

once the r derivative is known, (found using finite difference with a small increment in r by marching away from the patch boundary) the values of $P(x, y)$ off the boundary are determined. The streamfunction in the translating frame is then

$$\psi(x, y) = \exp(4\beta y)P(x, y) + \frac{UH_0}{2\beta}\exp(2\beta y). \tag{3.59}$$

Streamlines are plotted for three members of the family solution having zero centre of vorticity y_c with corresponding $R_1 = 1, 2, 3$ as shown in Figure 3.5. The last frame presents a magnified section of most extreme case computed ($R_1 = 5.05$). A more sophisticated numerical routine would need to be developed for the computation of a limiting state that has high curvature. The streamlines indicate that there exists an unstable stagnation point on the y-axis below the lowest patch boundary point, by unstable here it means placing a fluid next to the stagnation point will result in it being carried away. As the beach vortex approaches its limiting state, the stagnation point approaches the patch boundary and is expected to meet the lowest boundary point when the limiting state is achieved. The streamline patterns show that the velocity is largest on the deep side of the patch and smallest on the shallow side. The streamlines are compressed near the upper patch boundary compared to the

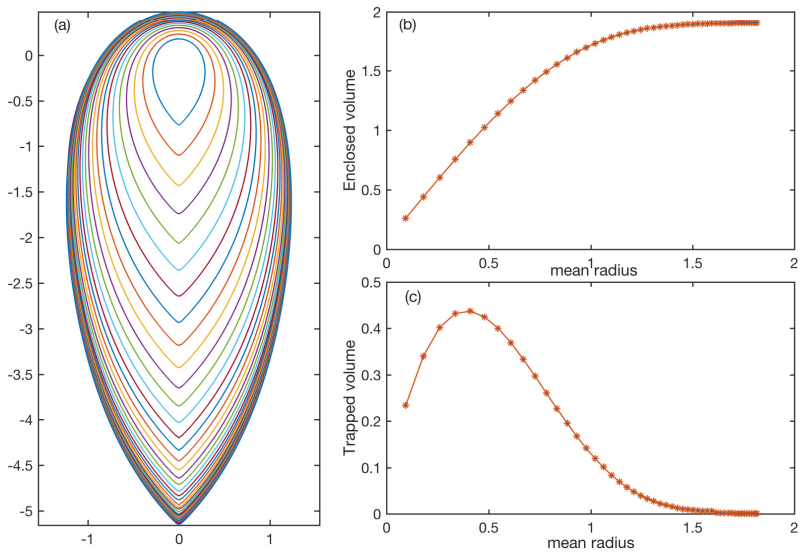

Figure 3.6: (a) The bounding streamlines for the beach vortices. (b) Total volume enclosed by bounding streamline plotted against the mean radius. (c) Trapped fluid volume between vortex patch and bounding streamline against mean radius.

shallow side of the fluid.

The bounding streamlines that separate different flow regions for the family of solutions in Figure 3.4 are plotted in Figure 3.6(a). The total volume enclosed by the bounding streamlines is plotted in Figure 3.6(b) as a function of the mean radius of the beach vortex and the fluid volume trapped in-between the beach vortex and bounding streamline is plotted in Figure 3.6(c) against the mean radius. As expected the total volume approaches a constant and the trapped volume approaches zero as the patch approaches its limiting state. In the limiting state, the beach vortex boundary coincides with the bounding streamline.

3.4 Asymptotic Analysis

Analytical progress in finding the streamfunction can be made in the limiting case of a circular beach vortex when the slope β tends to zero. The asymptotic expansion and matching method follows from the examples given in Hinch (1991).

The governing equation can be written as

$$\nabla \cdot \left(\frac{1}{H} \nabla \psi \right) = \begin{cases} q_0 H, & r < R(\theta), \\ 0, & r > R(\theta), \end{cases} \tag{3.60}$$

where the boundary for $\beta \ll 1$ is expanded as $R(\theta) = a + \beta F_1(\theta) + \beta^2 F_2(\theta) + \cdots$, where a is the asymptotic circular radius. In polar coordinates

$$\nabla^2 \psi - 2\beta \underbrace{\left(\sin\theta \frac{\partial \psi}{\partial r} + \frac{\cos\theta}{r} \frac{\partial \psi}{\partial \theta} \right)}_{\frac{\partial \psi}{\partial y}} = \begin{cases} q_0 H_0^2 \exp(4\beta y), & r < R(\theta), \\ 0, & r > R(\theta). \end{cases} \tag{3.61}$$

The term F_1 if included is found to be zero, an asymptotic approximation is derived here using $F_1 = 0$ for simplicity. The boundary conditions to apply here are that velocity is continuous across the patch boundary and the far field velocity tends to zero, i.e.

$$\begin{aligned} &\left(\frac{\partial \psi}{\partial r}, \frac{\partial \psi}{\partial \theta} \right), \quad \text{continuous on } r = R, \\ &\left(-\frac{1}{H} \frac{\partial \psi}{\partial r}, \frac{1}{Hr} \frac{\partial \psi}{\partial \theta} \right) \to 0, \quad \text{as } r \to \infty. \end{aligned} \tag{3.62}$$

3.4.1 Regular Expansion

First try expressing ψ as the regular expansion

$$\psi = \psi_0 + \beta \psi_2. \tag{3.63}$$

Using boundary conditions (3.62) the the leading order term ψ_0 is found to be:

$$\psi_0 = \begin{cases} \frac{1}{4}q_0 H_0^2(r^2 - a^2), & r < a, \\ \frac{1}{2}q_0 H_0^2 a^2 \log(r/a), & r > a. \end{cases} \tag{3.64}$$

(3.65)

Moving to O(β), the next order solution, ψ_2 is found to be

$$\psi_2 = \begin{cases} (A_1 r + \frac{5}{8}q_0 H_0^2 r^3)\sin\theta, & r < a, \\ (Ar + \frac{B}{r} + \frac{1}{2}q_0 H_0^2 a^2 r\log(r))\sin\theta, & r > a. \end{cases} \tag{3.66}$$

However, outside the patch the far field condition cannot be satisfied due to the presence of $r\log r$ term. The reason being, in the region $\rho = \beta r$, the $\beta\frac{\partial\psi}{\partial y}$ term in (3.61) is no longer small and becomes comparable to the other terms. The solution in the region ρ must be found and be used for matching.

3.4.2 The $\rho = \beta r$ region expansion

Consider the solution outside the beach vortex when $r > R$, in the ρ region the governing equation is rescaled to be

$$\frac{1}{\rho}\frac{\partial}{\partial\rho}\left(\rho\frac{\partial\Psi}{\partial\rho}\right) + \frac{1}{\rho^2}\frac{\partial^2\Psi}{\partial\theta^2} - 2\sin\theta\frac{\partial\Psi}{\partial\rho} - \frac{2\cos\theta}{\rho}\frac{\partial\Psi}{\partial\theta} = 0, \tag{3.67}$$

where Ψ is the ρ region streamfunction i.e. ($r \to \infty$ region). The solution to this homogeneous equation is in the form of the Green's function and its derivatives, the Green's function being

$$G = \exp(Y)K_0(\rho) = \exp(\rho\sin\theta)K_0(\rho). \tag{3.68}$$

which satisfies governing equation for $\rho \neq 0$. Here $Y = \rho \sin\theta$. Both derivatives of G vanishes as the $\rho \to \infty$ and so G satisfies the far field boundary condition. Thus Ψ is a multiple of G and $\partial G/\partial Y$. In the limit $\rho \to 0$, the Green's function G becomes

$$G \to \Big(-\gamma + \log 2 - \log \rho \Big) + \Big(-\gamma + \log 2 - \log \rho \Big) \rho \sin\theta + O(\rho^2), \tag{3.69}$$

where γ is the Euler Gamma constant.

3.4.3 Scaling the far field solution

In the regular expansion the $\log r$ term in ψ_0 behaves in the far field as $\log(\rho/\beta) = -\log\beta + \log\rho$ which suggests a far field expansion must include a $\log\beta$ order term and a constant term. To match the regular inner expansion, the far field expansion must be of the form

$$\Psi = C\log\beta + C_1 + D * G(\rho,\theta) + O(\beta) + \ldots \tag{3.70}$$

where C, C_1, D are constants to be determined through matching. Now the expansion of function G in (3.69) contains a $\rho\log\rho\sin\theta$ term. This means the regular expansion must include a $\beta\log\beta\psi_1$ term in order to match two regions and it is easy to deduce that $\psi_1 = f(r)\sin\theta$. By solving the streamfunction outside $r > R$, ψ_1 is found to be $\psi_1 = \big(Er + \frac{F}{r}\big)$. The $1/r$ term can be matched by $\partial G/\partial Y$ in the far field, but the matching does not give any information about what the constant F is. To determine this constant, the velocity condition across the patch boundary must be used. In summary, the regular expansion for the region $r > R$ (outside patch) is in the form

$$\begin{aligned} \psi &= \frac{1}{2}q_0 H_0^2 a^2 \log\left(\frac{r}{a}\right) + \beta\log\beta\left(Er + \frac{F}{r}\right)\sin\theta \\ &\quad + \beta\Big(Ar + \frac{B}{r} + \frac{1}{2}q_0 H_0^2 a^2 r\log r\Big)\sin\theta. \end{aligned} \tag{3.71}$$

3.4.4 Matching

Finally, to determine the constants in the regular expansion and ρ region expansion the two solutions are match at intermediate region defined by η being constant where

$$\eta = r\beta^{\alpha} = \frac{\rho}{\beta^{1-\alpha}}, \qquad 0 < \alpha < 1. \tag{3.72}$$

Expanding both solutions gives

$$\begin{aligned} \psi &= \frac{1}{2}q_0 H_0^2 a^2\Big(\log\eta - \alpha\log\beta\Big) - \frac{1}{2}q_0 H_0^2 a^2 \log a \\ &\quad +\beta\log\beta E\frac{\eta}{\beta^{\alpha}}\sin\theta \\ &\quad \beta\Big(\frac{B}{\eta}\beta^{\alpha} + \frac{1}{2}q_0 H_0^2 a^2\frac{\eta}{\beta^{\alpha}}\log\left(\frac{\eta}{\beta^{\alpha}}\right) + A\frac{\eta}{\beta^{\alpha}}\Big)\sin\theta, \end{aligned} \tag{3.73}$$

and the far field solution as

$$\begin{aligned} \Psi &= C\log\beta + C_1 + D(-\gamma+\log 2) - D\Big(\log\eta + (1-\alpha)\log\beta\Big) \\ &\quad +D(-\gamma+\log 2)\beta^{1-\alpha}\eta\sin\theta - D\Big(\log\eta + (1-\alpha)\log\beta\Big)\beta^{1-\alpha}\eta\sin\theta. \end{aligned} \tag{3.74}$$

Now, for different orders, this must be true for all valid α

$$\begin{aligned} O(\log\beta): &\quad C - D(1-\alpha) = -\alpha\frac{1}{2}q_0 H_0^2 a^2, \\ O(\beta^0): &\quad D(-\gamma+\log 2) - D\log\eta + C_1 = \frac{1}{2}q_0 H_0^2 a^2(\log\eta - \log a), \\ O(\beta^{1-\alpha}\log\beta): &- D(1-\alpha)\eta\sin\theta = (E - \frac{1}{2}q_0 H_0^2 a^2\alpha)\eta\sin\theta, \\ O(\beta^{1-\alpha}): &\quad D(-\gamma+\log 2)\eta\sin\theta - D\eta\log\eta\sin\theta, \\ &= \frac{1}{2}q_0 H_0^2 a^2\eta\log\eta\sin\theta + A\eta\sin\theta, \end{aligned}$$

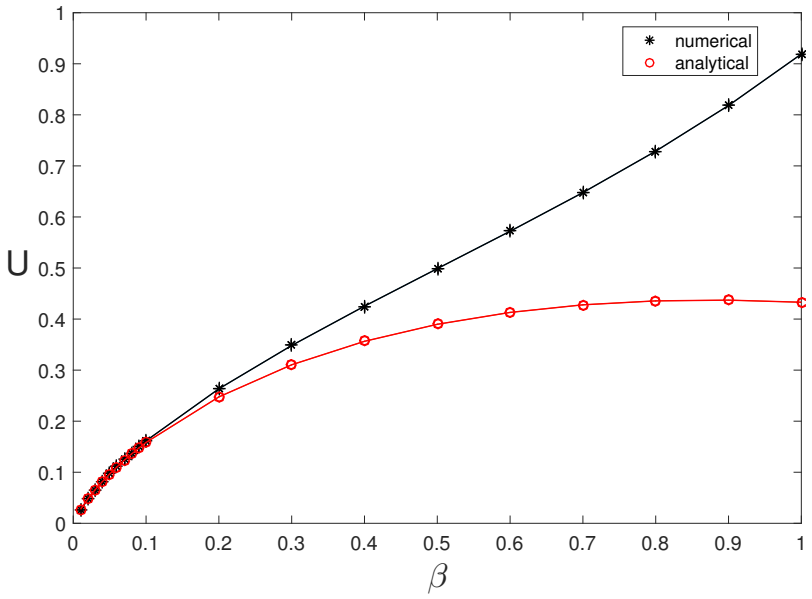

Figure 3.7: The asymptotically approximated translational velocity of near unit circular beach vortex for various β and the numerically computed translational velocity for beach vortices with prescribed characteristic radii $R_1 = R_{N+1} = 1$.

(3.75)

It is found that

$$D = C = -\frac{1}{2}q_0 H_0^2 a^2, \qquad C_1 = -D(-\gamma + \log(2/a)),$$
$$E = \frac{1}{2}q_0 H_0^2 a^2, \qquad A = D(-\gamma + \log 2).$$

The composite solution is in fact just Ψ since the regular expansion after rescaling is completely contained in far field expansion. Now setting $a = q_0 = H_0 = 1$ gives

$$\psi = \frac{1}{2}\log r + \beta \log \beta \left(\frac{1}{2}r + \frac{F}{r}\right)\sin\theta + \beta\left(\frac{1}{2}(\gamma - \log 2)r + \frac{B}{r} + \frac{1}{2}r\log r\right)\sin\theta + \ldots$$
$$\Psi = -\frac{1}{2}\log\beta - \frac{1}{2}(\gamma - \log 2) - \frac{1}{2}\exp(\rho\sin\theta)K_0(\rho) + \beta^2\log\beta L_1\frac{\partial G}{\partial Y} + \beta^2 L_2\frac{\partial G}{\partial Y} + O(\beta)$$

(3.76)

where L_1, L_2 are just constants and these terms turns out to be not necessary to obtain first order approximation. To determine F and B, the boundary condition

that velocity is continuous across the patch boundary is used. The streamfunction inside the patch ($r < R$) is

$$\psi_{(\text{inside})} = \frac{1}{4}q_0 H_0^2(r^2 - a^2) + \beta \log \beta C_1 r \sin\theta + \beta(A_1 r + \frac{5}{8}q_0 H_0^2 r^3)\sin\theta. \quad (3.77)$$

Using continuity of velocity across patch boundary gives $F = 0$ and $B = -3/8$. Now in the translating frame the streamfunction on the patch boundary satisfies

$$\psi + \frac{U}{2\beta}\exp(2\beta y) = A. \quad (3.78)$$

Expanding $U = -\beta \log \beta U_1 - \beta U_2 + \cdots$, and using the boundary condition gives

$$\begin{aligned} U &= -\frac{1}{2}\beta \log \beta - \frac{1}{2}\beta\left(\gamma - \log 2 - \frac{3}{4}\right) \\ &= -\frac{1}{2}\beta\left(\log \beta + \gamma - \log 2 - \frac{3}{4}\right). \end{aligned} \quad (3.79)$$

Figure 3.7 compares the asymptotic formula (3.79) for the translational velocity with the numerically computed results obtained by prescribing $R_1 = R_{N+1} = 1$ for various values of slope β. The agreement is excellent for β up to 0.1 after which two results start to diverge.

3.5 Linear stability analysis

Before investigating the linear stability of the beach vortices over exponential topography, the well-known linear stability results of a circular patch and Kirchhoff ellipse in a constant depth profile are reviewed here and reproduced numerically. The numerical routine used for computation follows Dritschel (1985) and subsequently the algorithm is modified to compute the linear stability of beach vortices.

3.5.1 Linear stability of a circular patch of constant vorticity in constant depth

Consider the perturbation of a unit circular patch of constant vorticity in the form

$$r = 1 + \sum_{m=1}^{N} \left(a_m \sin(m\theta) + b_m \cos(m\theta)\right) e^{\sigma t}, \tag{3.80}$$

where $a_m, b_m \ll 1$ and σ is the term representing growth and frequency of the perturbation (in general, a complex number). A point on the boundary stays on the boundary, so

$$\frac{Dr}{Dt} = u_r, \tag{3.81}$$

and the linearised form of (3.81) using (3.80) has the form

$$\sigma \sum_{m=1}^{N} \left(a_m \sin(m\theta) + b_m \cos(m\theta)\right) + u_{0\theta} \sum_{m=1}^{N} \left(m a_m \cos(m\theta) - m b_m \sin(m\theta)\right) = \widehat{u}_r. \tag{3.82}$$

where $u_{0\theta} = \frac{1}{2} w_0$ is the velocity for circular patch (Rankine vortex), ω_0 is the patch vorticity, and $\widehat{u}_r$ is the perturbation radial velocity. It is straight forward to show from the integral form of velocity that

$$\widehat{u}_r = \frac{1}{2} w_0 \sum_{m=1}^{N} \left(a_m \cos(m\theta) - b_m \sin(m\theta)\right). \tag{3.83}$$

Plug (3.83) into (3.82) and solve to give the frequency as eigenvalues:

$$\sigma = \pm i \frac{m-1}{2}. \tag{3.84}$$

These are all imaginary, so the circular patch is neutrally stable.

3.5.2 Linear stability of Kirchhoff vortices in constant depth

The linear stability of an elliptical vortex patch has been given in Love (1893). Using elliptical coordinates(ξ, η), perturbations of the form

$$\frac{\delta\xi}{h_0(\eta)^2} = \sum_{m=1}^{\infty} a_m \cos(m\eta) + b_m \sin(m\eta), \tag{3.85}$$

where $h_0^2(\eta) = a^2 \sin(\eta)^2 + b^2 \cos(\eta)^2$ is the Jacobian of the coordinate transformation, and $\delta\xi e^{ist}$ is the perturbation used for linear stability analysis. Here s is the frequency of the perturbation and a, b are the semi-axes of the elliptical boundary of the vortex. For the m mode isolated perturbation it is found

$$s^2 = \frac{w_0^2}{4}\left[\left(\frac{2mab}{(a+b)^2} - 1\right)^2 - \left(\frac{a-b}{a+b}\right)^{2m}\right]. \tag{3.86}$$

The $m = 1$ mode is always stable, and $m = 2$ mode of perturbation leads to a larger sized steady rotating Kirchhoff ellipse which which is stable by nature. For $m = 3$, within the range of aspect ratio $a/b < 3$, the eigenvalues s^2 is real and positive so the patch is linearly stable. Higher frequency modes have a larger critical aspect ratio that separates the linear stability and instability regions.

Figure 3.8 shows the magnitude of eigenvalues $|s|$ in (3.86) for m mode perturbation to Kirchhoff ellipses of various aspect ratio a/b are plotted as the dashed and solid lines. As a/b increases from 1 (circular patch) upwards, the eigenvalue σ goes from pure imaginary (plotted as dashed line) across zero to pure real (plotted as solid line) i.e. there exists a critical aspect ratio a/b for which the Kirchhoff vortex is linearly stable. The stars, crosses, circles and squares are the numerically computed eigenvalues which agree well with the analytical results. The numerical results have been calculated following the method of Dritschel (1985) who introduces a numeri-

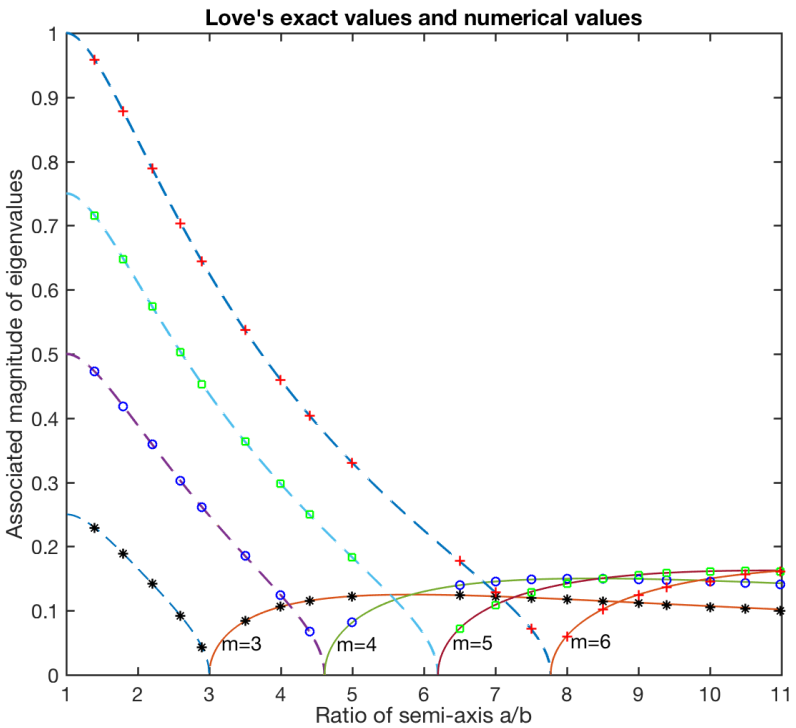

Figure 3.8: The magnitude of the eigenvalues $|s|$ for perturbations of mode number m for Kirchhoff ellipses of various aspect ratios. The dashed line and solid lines are the analytical solution from (3.86) where dashed line gives the oscillatory eigenvalues (pure imaginary) and solid line gives the eigenvalues having real values. The stars, crosses, squares and circles are the numerically produced eigenvalues in which 1000 boundary points and 201 modes are used in the perturbation series.

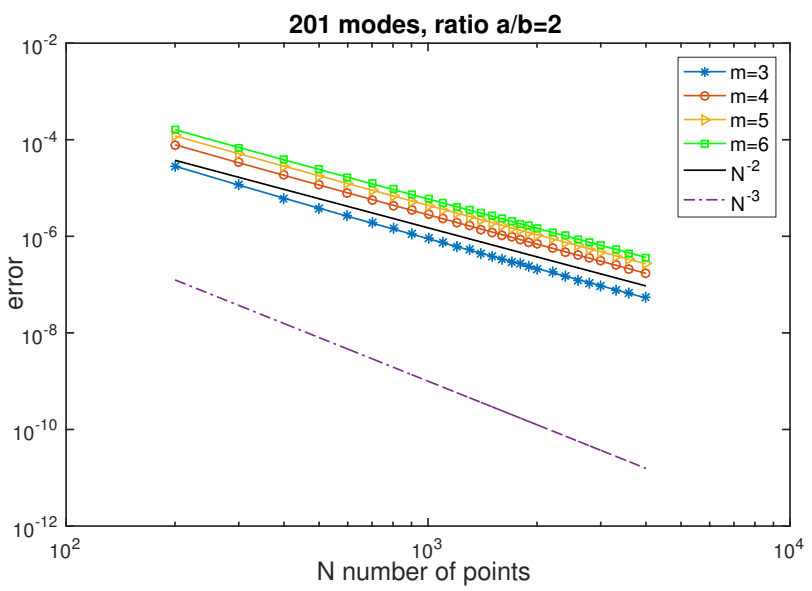

Figure 3.9: The error in the numerically computed eigenvalues for mode m perturbations for a Kirchhoff ellipse of aspect ratio 2.

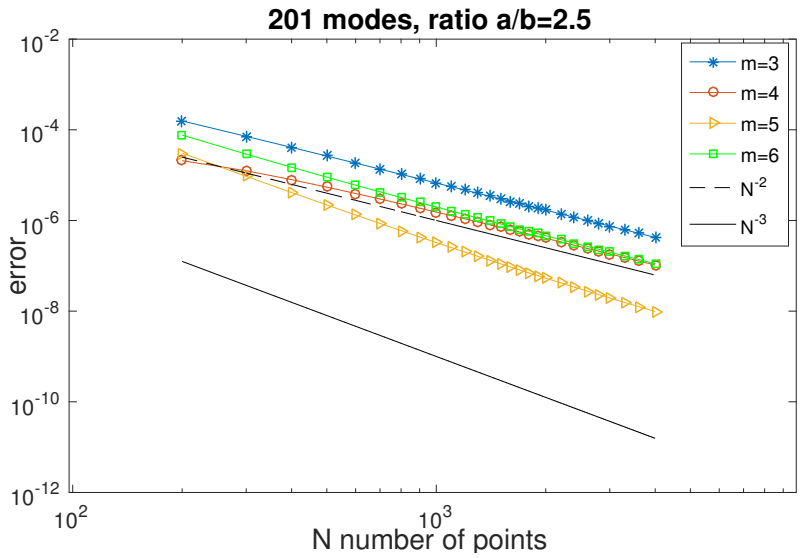

Figure 3.10: The error in the numerically computed eigenvalues for mode m perturbations for a Kirchhoff ellipse of aspect ratio 2.5

cal routine to compute the linear stability of m-polygon co-rotating vortex patches. This method has been described and adapted in Section 2.3.3 to compute the linear stability of '$m+1$' point vortex - vortex patch equilibria. A series summation of an orthonormal series in (2.24) has been used to represent the linear perturbation to the patch boundaries, which upon substituting into the governing linearised boundary equation leads to an eigenvalue problem (2.28). For the computations in Figure 3.8, 1000 boundary points have been used with 201 modes to represent the linear perturbation, the corresponding eigenvalues for $m = 3, 4, 5, 6$ modes are found from the ordered list of the eigenvalues of the 201 modes. Figure 3.9 and Figure 3.10 show plots of the errors in the numerically computed eigenvalues for mode m perturbations against the number of boundary points N on the Kirchhoff vortex. Comparing with lines of shape N^{-2} and N^{-3}, the two figures, one for the Kirchhoff vortex of aspect ratio 2 the other for the Kirchhoff ellipse of aspect ratio 2.5, indicate that second order accuracy is achieved. With the accuracy of the numerical procedure demonstrated, the next section applies the same procedure to determine the stability of beach vortices over exponential topography.

3.5.3 Linear stability of beach vortices

Consider a convergent solution for a beach vortex with boundary points $x_0 = r_0(\theta)\cos\theta, y_0 = r_0(\theta)\sin\theta$ where θ are evenly spaced, and subject the boundary to a perturbation of the form

$$r = r_0 + \widehat{r}e^{\sigma t} = r_0(\theta) + r_0(\theta)\sum_{m=1}^{M} C_m\phi_m(\theta)e^{\sigma t}, \tag{3.87}$$

where the $\phi_m(\theta)$ are the orthonormal functions

$$\pi^{\frac{1}{2}}\phi = \left(\frac{1}{\sqrt{2}}, \cos\theta, \cos(2\theta), \ldots, \cos(P\theta), \sin\theta, \sin(2\theta), \ldots, \sin(P\theta)\right), \tag{3.88}$$

($M = 2P+1$). The coefficients C_m are to be determined. M is the order of truncation. Now a point on the boundary stays on the boundary, so in the translational frame

$$\frac{D}{Dt}\left(r_0(\theta) + \widehat{r}(\theta)e^{\sigma t}\right) = u_r. \tag{3.89}$$

Linearising (3.89) and collecting terms of the same order gives

$$\sigma\widehat{r}(\theta) + \frac{1}{r_0}\frac{\partial r_0}{\partial\theta}\widehat{u}_\theta - \frac{u_{0\theta}}{r_0^2}\frac{\partial r_0}{\partial\theta}\widehat{r} + \frac{u_{0\theta}}{r_0}\frac{\partial\widehat{r}}{\partial\theta} = \widehat{u}_r, \tag{3.90}$$

$$\text{base state O(1):} \qquad \frac{u_{0\theta}}{r_0}\frac{\partial r_0}{\partial\theta} = u_{0r}, \tag{3.91}$$

where the velocities on the perturbed boundary used for linearisation are

$$(u_\theta, u_r) = (u_{0\theta} + \widehat{u}_\theta e^{\sigma t}, u_{0r} + \widehat{u}_r e^{\sigma t}), \tag{3.92}$$

the first terms on the right side $u_{0\theta}, v_{0\theta}$ are the base state velocities in the azimuthal and radial direction and the terms with hats are the perturbation velocities. The

velocities in the radial and azimuthal directions are

$$u_\theta = v\cos(\theta) - (u-U)\sin(\theta), \tag{3.93}$$

$$u_r = (u-U)\cos(\theta) + v\sin(\theta), \tag{3.94}$$

where u, v are the Cartesian components of velocities defined in (3.37) on the perturbed boundary and

$$(u, v) = (u_0 + \widehat{u}, v_0 + \widehat{v}). \tag{3.95}$$

Note

$$\widehat{u_\theta} = \widehat{v}\cos\theta - \widehat{u}\sin\theta, \tag{3.96}$$

$$\widehat{u_r} = \widehat{u}\cos\theta + \widehat{v}\sin\theta. \tag{3.97}$$

Using the velocity expression in terms of $P(x, y)$ and its derivatives in (3.16) gives the perturbation velocities, after linearisation to first order,

$$\begin{aligned}\widehat{u} &= -\frac{1}{H_0}\exp(2\beta y_0)\left[2\widehat{r}\beta\sin(\theta)P_y^0 + \widehat{P}_y\right] - \frac{4\beta}{H_0}\exp(-2\beta y_0)\left[-2\widehat{r}\beta\sin(\theta)\psi^0 + \widehat{\psi}\right], \\ \widehat{v} &= \frac{1}{H_0}\exp(2\beta y_0)\left[2\widehat{r}\beta\sin(\theta)P_x^0 + \widehat{P}_x\right],\end{aligned} \tag{3.98}$$

where the superscript 0 means evaluation at (r_0, θ), the unperturbed boundary. Now replace

$$\psi^0 = A - \frac{UH_0}{2\beta}\exp(2\beta y_0),$$

the constant A comes from the numerical computation as part of the solution of finding convergent vortex patch. The remaining task is to find expressions for $\widehat{P_x}, \widehat{P_y}, \widehat{\psi}$, which have two contributions: the perturbation of the observation point and the contribution from the perturbation of integration boundary points i.e. the perturbation due to the evaluation of functions at perturbed boundary integrated over

unperturbed boundary, and the perturbation due to evaluation of functions at unperturbed boundary integrated over perturbed boundary.

To find $\widehat{\psi}$, first consider the perturbation of observation points which gives rise to first order perturbation term:

$$\begin{aligned}\widehat{\psi}_p &= \widehat{r}\frac{\partial\psi}{\partial r}(r_0,\theta) \\ &= \widehat{r}\left[\frac{\partial\psi}{\partial x}(r_0,\theta)\cos\theta + \frac{\partial\psi}{\partial y}(r_0,\theta)\sin\theta\right],\end{aligned} \tag{3.99}$$

where $\partial\psi/\partial x, \partial\psi/\partial y$ can be found through relationship between ψ and $P(x,y)$:

$$\begin{aligned}\frac{\partial\psi}{\partial x}(r_0,\theta) &= \exp(4\beta y_0)P_x^0, \\ \frac{\partial\psi}{\partial y}(r_0,\theta) &= \exp(4\beta y_0)P_y^0 + 4\beta\psi(r_0,\theta),\end{aligned} \tag{3.100}$$

and $\psi(r_0,\theta)$ comes from $\psi + \psi_0 = A$. The second contribution of perturbation term in $\widehat{\psi}$ is from the perturbation of the integration boundary points, from the streamfunction expression (3.12) this is simply

$$\widehat{\psi}_i = -\frac{q_0 H_0^2}{2\pi}\int_0^{2\pi}\widehat{r'}\exp(\beta y_0 + 3\beta y_0')K_0\left(\beta\sqrt{(x_0-x_0')^2+(y_0-y_0')^2}\right)r_0' d\alpha, \tag{3.101}$$

where the dashed variables are a function of α, the integrating variable. This integral is evaluated using the mid-point rule. Summing gives $\widehat{\psi} = \widehat{\psi}_p + \widehat{\psi}_i$. Substituting into (3.98) gives

$$\begin{aligned}\widehat{u} &= -\frac{1}{H_0}\exp(2\beta y_0)\left[\widehat{r}\left(6\beta\sin(\theta)P_y^0 + 4\beta\cos(\theta)P_x^0\right) + \widehat{P}_y\right] \\ &\quad -\frac{4\beta}{H_0}\exp(-2\beta y_0)\left[\widehat{r}2\beta\sin(\theta)\psi^0 + \widehat{\psi}_i\right], \\ \widehat{v} &= \frac{1}{H_0}\exp(2\beta y_0)\left[\widehat{r}2\beta\sin(\theta)P_x^0 + \widehat{P}_x\right].\end{aligned} \tag{3.102}$$

Recall that P_x^0, P_y^0 are evaluated using the boundary integrals in (3.39). It remains

to find $\widehat{P_x}, \widehat{P_y}$ terms.

The perturbation terms $\widehat{P}_x, \widehat{P}_y$ again have two contributions. First, express P_x, P_y as the integral

$$\begin{pmatrix} P_x \\ P_y \end{pmatrix} = \frac{q_0 H_0^2}{2\pi} \int_0^{2\pi} \exp(-3\beta(y-Y)) K_0 \left(\beta \sqrt{(x-X)^2 + (y-Y)^2} \right) \begin{pmatrix} \frac{dY}{d\alpha} \\ -\frac{dX}{d\alpha} \end{pmatrix} d\alpha,$$

where $x = x_0 + \widehat{x}, y = y_0 + \widehat{y}, X = X_0 + \widehat{X}, Y = Y_0 + \widehat{Y}$. Here subscripts indicate the steady solution and hatted variables are the perturbation variables. Now Taylor expand the integrand, use integration by parts to convert one of the integrals and collect the first order terms to give

$$\begin{aligned} \begin{pmatrix} \widehat{P}_x \\ \widehat{P}_y \end{pmatrix} = & \frac{q_0 H_0^2}{2\pi} \left[\widehat{r}(\theta) \int_0^{2\pi} \exp(-3\beta y_{01}) K_0(\beta r_{01}) \left(\frac{dX_0}{d\alpha} \sin\theta - \frac{dY_0}{d\alpha} \cos\theta \right) \begin{pmatrix} 0 \\ 3\beta \end{pmatrix} \right] d\alpha \\ & + \frac{q_0 H_0^2}{2\pi} \left[\widehat{r}(\theta) \int_0^{2\pi} \exp(-3\beta y_{01}) \frac{K_1(\beta r_{01})}{r_{01}} \left(\frac{dX_0}{d\alpha} \sin\theta - \frac{dY_0}{d\alpha} \cos\theta \right) \begin{pmatrix} \beta x_{01} \\ \beta y_{01} \end{pmatrix} \right] d\alpha \\ & - \frac{q_0 H_0^2}{2\pi} \left[\int_0^{2\pi} \widehat{r}(\alpha) \exp(-3\beta y_{01}) K_0(\beta r_{01}) \left(\frac{dX_0}{d\alpha} \sin\alpha - \frac{dY_0}{d\alpha} \cos\alpha \right) \begin{pmatrix} 0 \\ 3\beta \end{pmatrix} \right] d\alpha \\ & - \frac{q_0 H_0^2}{2\pi} \left[\int_0^{2\pi} \widehat{r}(\alpha) \exp(-3\beta y_{01}) \frac{K_1(\beta r_{01})}{r_{01}} \left(\frac{dX_0}{d\alpha} \sin\alpha - \frac{dY_0}{d\alpha} \cos\alpha \right) \begin{pmatrix} \beta x_{01} \\ \beta y_{01} \end{pmatrix} \right] d\alpha, \end{aligned} \tag{3.103}$$

where $x_{01} = x_0 - X_0, y_{01} = y_0 - Y_0$ and $r_{01} = \sqrt{(x_0 - X_0)^2 + (y_0 - Y_0)^2}$. Introducing a similar abbreviation to Dritschel (1985), namely

$$\begin{aligned} \langle() \rangle &= \frac{q_0 H_0^2}{2\pi} \int_0^{2\pi} () d\alpha, \qquad b^x = \frac{x_{01}}{r_{01}}, \qquad b^y = \frac{y_{01}}{r_{01}}, \\ Q_0 &= \exp(-3\beta y_{01}) K_0(\beta r_{01}) \left[\frac{dX_0}{d\alpha} \sin\alpha - \frac{dY_0}{d\alpha} \cos\alpha \right], \\ T_0 &= \exp(-3\beta y_{01}) K_0(\beta r_{01}) \left[\frac{dX_0}{d\alpha} \sin\theta - \frac{dY_0}{d\alpha} \cos\theta \right], \\ Q_1 &= \exp(-3\beta y_{01}) K_1(\beta r_{01}) \left[\frac{dX_0}{d\alpha} \sin\alpha - \frac{dY_0}{d\alpha} \cos\alpha \right], \\ T_1 &= \exp(-3\beta y_{01}) K_1(\beta r_{01}) \left[\frac{dX_0}{d\alpha} \sin\theta - \frac{dY_0}{d\alpha} \cos\theta \right], \end{aligned} \tag{3.104}$$

allows the $\widehat{P}_x, \widehat{P}_y$ to be abbreviated as

$$\begin{aligned}\widehat{P}_x(\theta) &= \widehat{r}(\theta)\langle\beta T_1 b^x\rangle - \langle\beta\widehat{r}(\alpha)Q_1 b^x\rangle,\\ \widehat{P}_y(\theta) &= \widehat{r}(\theta)\langle 3\beta T_0 + \beta T_1 b^y\rangle - \langle 3\beta\widehat{r}(\alpha)Q_0 + \beta\widehat{r}(\alpha)Q_1 b^y\rangle. \end{aligned} \tag{3.105}$$

Collecting the perturbation terms in the velocity from (3.102) gives

$$\begin{aligned}\widehat{u} &= -\frac{1}{H_0}\exp(2\beta y_0)\Big[\widehat{r}(\theta)\Big(\langle 3\beta T_0 + \beta T_1 b^y\rangle + 6\beta\sin\theta P_y^0 + 4\beta\cos\theta P_x^0\Big)\Big]\\ &\quad +\frac{1}{H_0}\exp(2\beta y_0)\Big[\langle\widehat{r}(\alpha)\Big(3\beta Q_0 + \beta Q_1 b^y\Big)\rangle\Big]\\ &\quad -\frac{4\beta}{H_0}\exp(-2\beta y_0)\left[\widehat{r}(\theta)2\beta\sin\theta\psi^0 + \widehat{\psi}_i(\widehat{r}(\alpha),\theta)\right],\\ \widehat{v} &= \frac{1}{H_0}\exp(2\beta y_0)\left[\widehat{r}(\theta)\Big(\langle\beta T_1 b^x\rangle + 2\beta\sin\theta P_x^0\Big) - \langle\beta\widehat{r}(\alpha)Q_1 b^x\rangle\right].\end{aligned}$$

Now express $\widehat{r}(\theta)$ as

$$\widehat{r}(\theta) = r_0(\theta)\gamma(\theta), \quad \text{where} \quad \gamma(\theta) = \sum_{m=1}^{M} C_m\phi_m(\theta), \tag{3.106}$$

Then (3.90) can be rewritten in terms of γ, define

$$\epsilon(\theta) = \sigma\gamma + \frac{u_{0\theta}}{r_0}\frac{d\gamma}{d\alpha} - \frac{1}{r_0 u_{0\theta}}(\widehat{u}v_0 - \widehat{v}u_0) \neq 0. \tag{3.107}$$

Using a Galerkin approach with finite number truncation requires:

$$\int_0^{2\pi}\epsilon(\alpha)\phi_i(\alpha)d\alpha = 0, \qquad i = 1, 2, \ldots, M. \tag{3.108}$$

Substitute these into the governing equation, defining similar matrix variables as in Dritschel (1985):

$$B(\theta) = -\frac{v_0}{H_0 u_{0\theta}}\left[\exp(2\beta y_0)\left(\langle 3\beta T_0 + \beta T_1 b^y\rangle + 6\beta\sin\theta P_y^0 + 4\beta\cos\theta P_x^0\right)\right]$$

$$
\begin{aligned}
& -\frac{v_0}{H_0 u_{0\theta}}\left[8\beta^2\exp(-2\beta y_0)\sin\theta\psi^0\right] \\
& -\frac{u_0}{H_0 u_{0\theta}}\exp(2\beta y_0)\left[\langle\beta T_1 b^x\rangle + 2\beta\sin\theta P_x^0\right], \\
D_m(\theta) &= \frac{v_0}{H_0 r_0 u_{0\theta}}\exp(2\beta y_0)\left[\langle\phi_m r_0(\alpha)\Big(3\beta Q_0 + \beta Q_1 b^y\Big)\rangle - 4\beta\exp(-4\beta y_0)\widehat{\psi}_i(\phi_m r_0(\alpha),\theta)\right] \\
& +\frac{u_0}{H_0 r_0 u_{0\theta}}\exp(2\beta y_0)\langle\beta\phi_m r_0(\alpha) Q_1 b^x\rangle, \\
E_{mn} &= \int_0^{2\pi} d\theta\Big(B(\theta)\phi_m(\theta) - \frac{u_{0\theta}}{r_0}\frac{d\phi_m}{d\theta}\Big)\phi_n(\theta), \\
F_{mn} &= \int_0^{2\pi} d\theta D_m(\theta)\phi_n(\theta), \\
A_{mn} &= F_{mn} + E_{mn},
\end{aligned}
\tag{3.109}
$$

reduces the problem to the matrix eigenvalue problem:

$$
\sigma C_n = \sum_{m=1}^{M} A_{mn} C_m, \qquad n = 1, 2, \ldots, M. \tag{3.110}
$$

Two constraints must also be imposed for constant depth profile vortex patch: the area and second momentum constraints. After linearisation they reduce to

$$
\begin{aligned}
\sum_{m=1}^{M} a_m C_m = 0, \qquad & a_m = \int_0^{2\pi} r_0^2(\theta)\phi_m(\theta)d\theta, \\
\sum_{m=1}^{M} b_m C_m = 0, \qquad & b_m = \int_0^{2\pi} r_0^4(\theta)\phi_m(\theta)d\theta.
\end{aligned}
\tag{3.111}
$$

These constraints are substituted here by choosing two non-zero coefficients say C_1, C_2 and expressing them in terms of $C_m, m = 3, 4, \ldots, M$ as

$$
\begin{aligned}
C_1 = \sum_{m=3}^{M} t_m C_m \quad , \quad t_m &= \frac{b_2 a_m - a_2 b_m}{a_2 b_1 - a_1 b_2}, \\
C_2 = \sum_{m=3}^{M} s_m C_m \quad , \quad s_m &= \frac{b_1 a_m - a_1 b_m}{a_1 b_2 - a_2 b_1}.
\end{aligned}
\tag{3.112}
$$

Substituting (3.112) into the eigenvalue problem (3.110) reduces the matrix to size

$(M-2)*(M-2)$, i.e.

$$\sigma C_n = \sum_{m=3}^{M} T_{m-2,n-2} C_m \quad , \quad n = 3, 4, \cdots, M, \tag{3.113}$$

where the new matrix T_{mn} is

$$T_{m-2,n-2} = A_{mn} + A_{n1} t_m + A_{n2} s_m. \tag{3.114}$$

The matrix problem (3.113) can then be solved in a standard way.

For example, to implement the two constraints for linear stability computation of a Kirchhoff vortex in Section 3.5.2 note that due to symmetry

$$\begin{aligned}
\int_0^{2\pi} r_0^2(\theta)\sin(n\theta)d\theta &= \left(\int_0^{\frac{\pi}{2}} + \int_{\frac{\pi}{2}}^{\pi} + \int_{\pi}^{\frac{3}{2}\pi} + \int_{\frac{3}{2}\pi}^{2\pi}\right) r_0^2 \sin(n\theta)d\theta \\
&= \int_0^{\frac{\pi}{2}} r_0^2(\theta)\sin(n\theta)d\theta + \int_0^{\frac{\pi}{2}} r_0^2(\theta)\sin(n(\pi-\theta))d\theta \\
&\quad + \int_0^{\frac{\pi}{2}} r_0^2(\theta)\sin(n(\pi+\theta))d\theta + \int_0^{\frac{\pi}{2}} r_0^2(\theta)\sin(-n\theta)d\theta \\
&= 0, \\
\int_0^{2\pi} r_0^2(\theta)\cos(n\theta)d\theta &= \int_0^{\frac{\pi}{2}} r_0^2(\theta)\left(\cos(n\theta) + \cos(n(\pi-\theta)) + \cos(n(\pi+\theta)) + \cos(-n\theta)\right) \\
&= 2(1+(-1)^n)\int_0^{\frac{\pi}{2}} r_0(\theta)^2\cos(n\theta)d\theta,
\end{aligned} \tag{3.115}$$

so in the area conservation, only the basis function $\phi_n(\theta) = \cos(n\theta)$ for n even gives non-zero integrals (as well as the constant basis function). This is also true for the momentum conservation (by replacing r_0^2 by r_0^4 in the integral) since the symmetry of the integrand does not change. These non-zero constant integrals of constraints were used to reduce the matrix eigenvalue problem and gave results presented in Section 3.5.2.

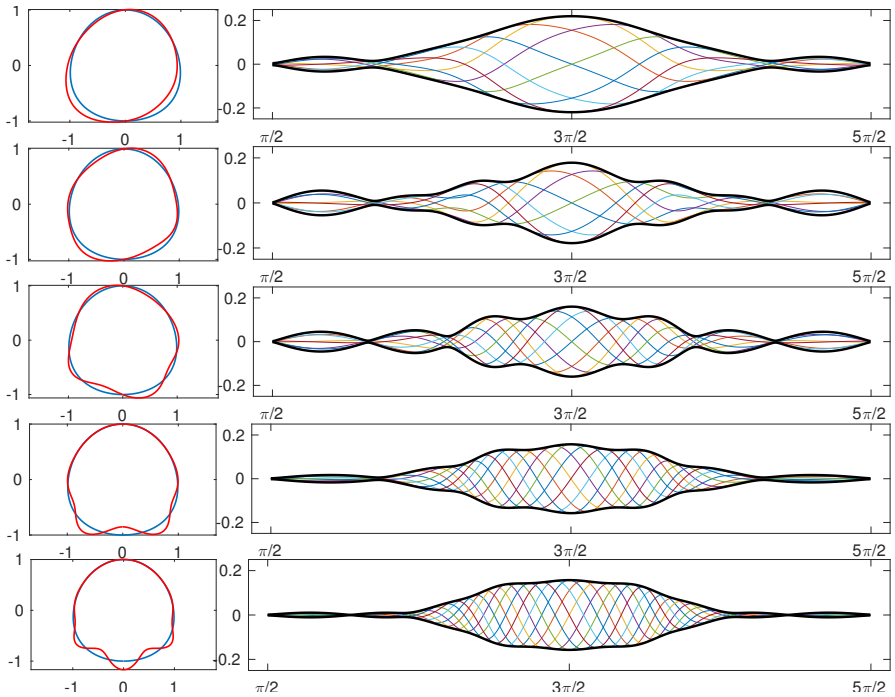

Figure 3.11: Left pictures are the steady states and the perturbed boundaries with $\beta = 1$ and right pictures plots the corresponding perturbation against θ. 1000 boundaries points and 201 modes have been used for computation.

For beach vortices over exponential topography, the total circulation and the impulse defined in (3.17) and (3.21) are conserved. Linearisation leads to

$$q_0 H_0 \int \exp(2\beta r_0 \sin\theta) r_0 \widehat{r} d\theta = \sum_{m=1}^{M} C_m q_0 H_0 \int \exp(2\beta r_0 \sin\theta) r_0^2 \phi_m(\theta) d\theta = 0,$$
$$\frac{q_0 H_0^2}{2\beta} \int \exp(4\beta r_0 \sin\theta) r_0 \widehat{r} d\theta = \sum_{m=1}^{M} C_m \frac{q_0 H_0}{2\beta} \int \exp(4\beta r_0 \sin\theta) r_0^2 \phi_m(\theta) d\theta = 0,$$

and the above procedure can be applied to implement the two constraints.

Linear stability has been computed for the family of solutions defined by fixed R_1, R_{N+1} with various β and the family of solutions with prescribed centre of vorticity y_c with various R_1 for fixed β. For all the computations, a range of boundary points from 300 to 1000 is used, as well as a different number of perturbation modes have been used. No growing modes have been found except when the beach vortices are near their limiting states. These growing eigenvalues appear near the end of the ordered list of eigenvalues computed which suggests they are fictitious grow-

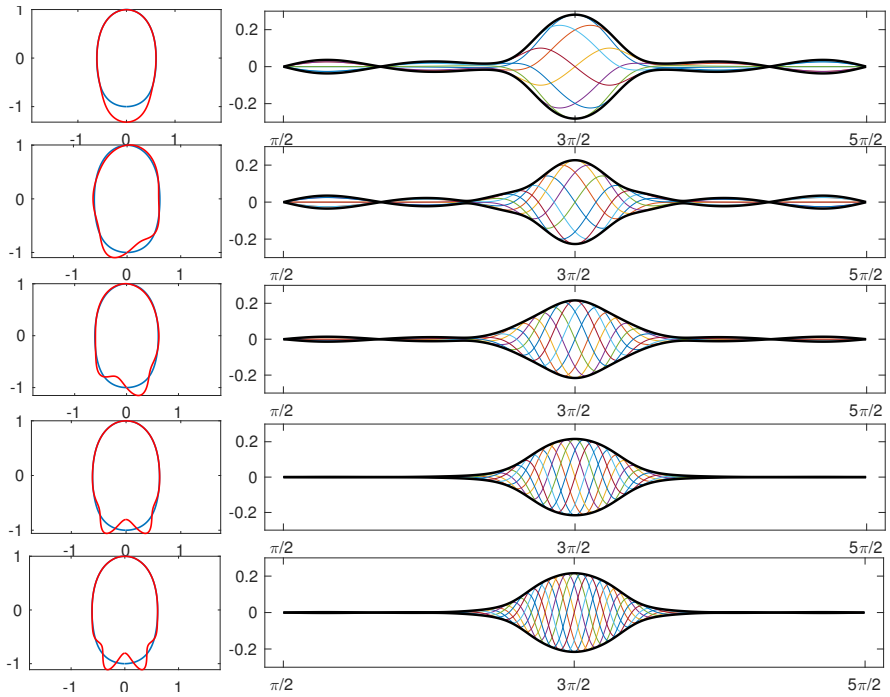

Figure 3.12: Left pictures are the steady states and the perturbed boundaries with $\beta = 2$ and right pictures plots the perturbation against θ at different phases enclosed by the envelopes. 1000 boundaries points and 201 modes have been used for computation.

ing modes generated by numerical inaccuracy. Figure 3.11 and Figure 3.12 shows the first 5 stable perturbations from the ordered list of imaginary eigenvalues (from low to high) for beach vortices with $R_1 = R_{N+1} = 1$. Figure 3.11 is for the beach vortex with $\beta = 1$ and Figure 3.12 is for the beach vortex with $\beta = 2$. Left hand side pictures show the steady states and the boundaries with perturbations in which the perturbation has maximum modulus 0.2 for illustrations. The right hand side pictures plot the first 5 perturbations at different phases enclosed by the two envelopes. The perturbations look rather flat on two sides and hump-like in the middle which corresponds to the part of boundary near the lowest boundary point, this is due to the exponential depth being deep in the positive y direction and shallow in the negative y direction. This is especially true for larger β which results in bigger depth difference. Previously in Figure 3.5 when producing the streamlines, it has been shown the velocities on the patch boundaries are fastest near positive y and gradually reduces towards the negative y, so the linear perturbation will be swept

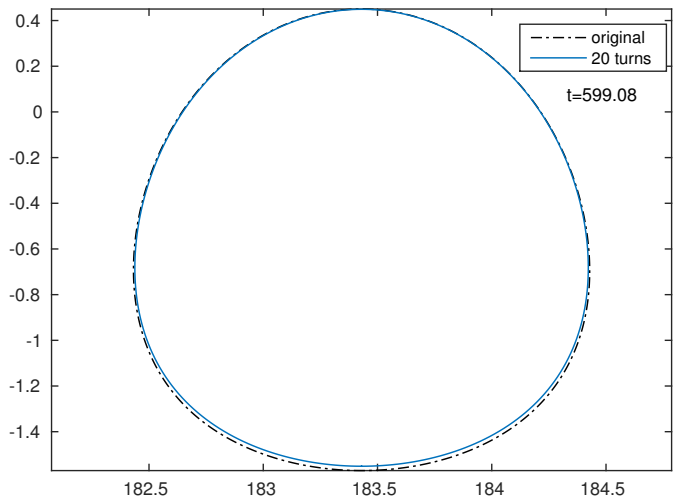

Figure 3.13: A comparison of time advanced beach vortex of unit mean radius after approximately 20 turnover times with the computed steadily propagating solution.

downwards towards the lowest boundary point. However, as mentioned these are associated with imaginary eigenvalues, so the beach vortices are linearly stable up to the near-limiting state.

3.6 Time-dependent evolutions

To test the robustness of the steady state beach vortices, a time-dependent evolution has been carried out on the family of solutions. A standard 4th order Runge-Kutta time-advancing scheme is used and at each time step the beach vortex boundary points are advected and then redistributed using the re-noding scheme of Dritschel (1988). These re-noded boundary points are then interpolated to boundary points that have evenly spaced θ relative to the chosen 'centre' of the beach vortex. The derivative

$$\frac{dP}{d\theta} = \frac{\partial P}{\partial x}\frac{dx}{d\theta} + \frac{\partial P}{\partial y}\frac{dy}{d\theta}, \tag{3.116}$$

can be evaluated where $dx/d\theta, dy/d\theta$ are evaluated using Fourier transforms. The inverse Fourier transform then gives, to within an additive constant, $P(x, y)$ at the

new boundary points. This constant is eliminated by equating the total vorticity with the total circulation as was done previously to obtain the value of A in (3.45). Then the values of $\psi(x, y)$ at the boundary points are known, and can be used to compute the velocities in (3.16) which are then used to advance the boundary points. Note this numerical routine only works for smooth boundaries due to the application of Fourier transforms and becomes inaccurate if the curvature is large. It is found that the beach vortex moves slightly towards positive y as it translates, this is a numerical artefact as the patch should translate purely in the x-direction by momentum conservation . This shift is reduced by having more boundary points and using smaller time steps observed over the same time interval which suggests the shift being the result of finite resolution in time and space. Thus after each time interval, the beach vortex is moved downwards a distance that makes the centre of vorticity of new patch matching the original one. This effectively ensure conservation of momentum. Almost all the beach vortices in the family of solutions with fixed y_c and R_1 have been observed to survive over 10 turnover times. Figure 3.13 shows the comparison of a beach vortex of unit mean radius over the exponential profile with $\beta = 1$ after 20 turnover times with the computed steadily propagating solution. 1000 boundary points have been used with the space increment $h = 0.01$ and time-step $dt = 0.01$. The match is good with a slight loss of volume over the long period of translation. Only those near the limiting state suffer from instability which appears to be due to insufficient resolution of boundaries with high curvature.

3.7 Summary

A family of steady-state beach vortices over exponential topography have been computed, which propagate parallel to isobaths. It is shown that there exist a limiting state beyond which no solution exists. The streamlines reveal that due to the

exponential depth profile, there is large adverse velocity on the deep side of fluid compared to the shallow side of fluid. There exists an unstable stagnation point on the shallow side of the beach vortex viewed in the translational frame. When a beach vortex approaches the limiting state, this stagnation point moves closer and closer to the patch boundary and meets the boundary at the limiting state. Three numerical routines have been described, all of which have been used to compute the steady state solutions. The family of solutions with each member having same fixed upper and lower boundary points demonstrates the competition of self-induction and that due to changing depth. An asymptotic approximation of a near-circular beach vortex in the small slope limiting has been derived and shown to give excellent agreement with the numerically computed results. Using a linear stability analysis modified from a method introduced in Dritschel (1985), these beach vortices have been shown to be linearly stable. Time-dependent integration also leads to the conclusion that beach vortices are robust structures.

The numerical routines used here are second order accurate, and the limiting solution of the solution family here appears to have a 90 degree tangent jump. To investigate more closely this limiting behaviour, a more sophisticated numerical routine would be required to handle the large curvature developed on the patch boundary. Further the time-dependent integration relies on the patch boundaries being smooth, in order to derive the value of streamfunction on the boundary at each time. The method is therefore unable to accurately compute the unstable evolution of a beach vortex. There thus remains further work to be done.

Appendix A

The Green's function derivation

Equation (3.9) can be written as

$$\nabla^2 G + H\nabla(H^{-1}).\nabla G = H(x', y')\delta(x - x')\delta(y - y'). \tag{A.1}$$

For the exponential topography (3.10), (A.1) becomes

$$\nabla^2 G - 2\beta G_y = H_0 \exp(2\beta y')\delta(x - x')\delta(y - y'). \tag{A.2}$$

Introducing $\widehat{G}$ so that $G = \exp(\beta y)\widehat{G}$, (A.2) becomes

$$\nabla^2 \widehat{G} - \beta^2 \widehat{G} = H_0 \exp(\beta y')\delta(x - x')\delta(y - y'), \tag{A.3}$$

which is a standard axisymmetric problem with the well-known solution

$$\widehat{G} = -\frac{H_0}{2\pi} \exp(\beta y')\mathrm{K}_0(\beta\sqrt{(x - x')^2 + (y - y')^2}), \tag{A.4}$$

so the Green's function G is

$$G(x', y', x, y) = -\frac{H_0}{2\pi} \exp[\beta(y + y')]\mathrm{K}_0(\beta\sqrt{(x - x')^2 + (y - y')^2}). \tag{A.5}$$

Appendix B

Evaluating the boundary integral using linear interpolation

The idea is to split the Bessel Function $\mathrm{K}_0(\beta r)$ into two parts, 'singular' and 'non-singular' part, and split the integral into different parts accordingly:

$$\begin{aligned}
&\oint_c \exp(-3\beta(y-y'))\mathrm{K}_0(\beta r)\tbinom{dy'}{dx'} \\
&= \oint_c \exp(-3\beta(y-y'))\left[(\mathrm{K}_0(\beta r)+\log(\beta r)-\log(\beta r)\right]\tbinom{dy'}{dx'} \\
&= \oint_c \exp(-3\beta(y-y'))(\mathrm{K}_0(\beta r)+\log(\beta r))\tbinom{dy'}{dx'} - \oint_c \exp(-3\beta(y-y'))\log(\beta r)\tbinom{dy'}{dx'}.
\end{aligned} \tag{B.1}$$

Note that $\mathrm{K}_0(\beta r)+\log(\beta r) \to -\gamma$ as $r \to 0$ and so is non-singular. Now for the linear interpolation

$$x' = x_n + a_n p, \qquad n = 1 \ldots N, \tag{B.2}$$

$$y' = y_n + b_n p, \qquad n = 1 \ldots N, \tag{B.3}$$

where $a_n = x_{n+1} - x_n, b_n = y_{n+1} - y_n$ are the gradients between adjacent points. The first integral in (B.1) can be written as

$$\sum_{i=1}^{N} \binom{b_i}{a_i} \int_0^1 \exp(-3\beta(y - y_i + b_i p))(K_o(\beta r) + \log(\beta r))dp, \tag{B.4}$$

this can be done using three point Gaussian integration rule. The second part in (B.1) can be approximated as

$$\begin{aligned} &-\sum_{i=1}^{N} \binom{b_i}{a_i} \int_0^1 \exp(-3\beta(y - y_i + b_i p)) \log(\beta r)dp \\ \simeq &-\sum_{i=1}^{N} \binom{b_i}{a_i} \int_0^1 \exp(-3\beta(y - y_i))(1 + 3\beta b_i p + \frac{9}{2}\beta^2 p^2 + \ldots) \log(\beta r)dp. \end{aligned} \tag{B.5}$$

These integrals in (B.5) can be done analytically, retaining integrand up to $o(p^2 \log p)$. For example on the interval $(\underline{x}_n, \underline{x}_{n+1})$

$$\begin{aligned} &\int_0^1 p \log\left[\beta\left((x - x_n - a_n p)^2 + (y - y_n - b_n p)^2\right)^{1/2}\right] dp \\ &\quad = -1 + \frac{1}{e_n} s_{n_3}(f_{n_2} - f_{n_1}) + \log(\beta l_{n_2}^{1/2}) + \frac{1}{2e_n} s_{n_1} g_n, \end{aligned} \tag{B.6}$$

and

$$\begin{aligned} &\int_0^1 p^2 \log\left[\beta\left((x - x_n - a_n p)^2 + (y - y_n - b_n p)^2\right)^{1/2}\right] dp \\ &= -\frac{1}{4} - \frac{1}{2e_n} s_{n_3} + \frac{1}{e_n^2} s_{n_1} s_{n_3}(f_{n_2} - f_{n_1}) + \frac{1}{4e_n^2}(s_{n_1}^2 - s_{n_3}^2) g_n, \end{aligned} \tag{B.7}$$

and

$$\begin{aligned} &\int_0^1 p^3 \log\left[\beta\left((x - x_n - a_n p)^2 + (y - y_n - b_n p)^2\right)^{1/2}\right] dp \\ &= -\tfrac{1}{9} - \tfrac{1}{6e_n} s_{n_1} - \tfrac{1}{3e_n^2}(s_{n_1}^2 - s_{n_3}^2) + \tfrac{1}{3e_n^3}(3 s_{n_3} s_{n_1}^2 - s_{n_3}^3)(f_{n_2} - f_{n_1}) \\ &\quad + \tfrac{1}{3}\log(\beta l_{n_2}^{1/2}) + \tfrac{1}{6e_n^3} s_{n_1}(s_{n_1}^2 - 3 s_{n_3}^2) g_n, \end{aligned} \tag{B.8}$$

where the $e_n, s_{n_1}, s_{n_2}, s_{n_3}, l_{n_1}, l_{n_2}, f_{n_1}, f_{n_2}$ are defined as

$$
\begin{aligned}
e_n &= a_n^2 + b_n^2, && \text{(B.9)}\\
s_{n_1} &= a_n(x - x_n) + b_n(y - y_n), && \text{(B.10)}\\
s_{n_2} &= a_n(x - x_{n+1}) + b_n(y - y_{n+1}), && \text{(B.11)}\\
s_{n_3} &= a_n(y - y_n) - b_n(x - x_n), && \text{(B.12)}\\
l_{n_1} &= (x - x_n)^2 + (y - y_n)^2, && \text{(B.13)}\\
l_{n_2} &= (x - x_{n+1})^2 + (y - y_{n+1})^2, && \text{(B.14)}\\
f_{n_1} &= \arctan(s_{n_3}/s_{n_1}), && \text{(B.15)}\\
f_{n_2} &= \arctan(s_{n_3}/s_{n_2}), && \text{(B.16)}\\
g_n &= \log\left[\frac{s_{n_1}^2}{s_{n_2}^2}\right]. && \text{(B.17)}
\end{aligned}
$$

Bibliography

Allen, J. S., Newberger, P. A., and Holman, R. A. (1996). Nonlinear shear instabilities of alongshore currents on plane beaches. *Journal of Fluid Mechanics*, 310:181–213.

Aref, H., Newton, P. K., Stremler, M. A., Tokieda, T., and Vainchtein, D. L. (2002). Vortex crystals. *Advances in Applied Mechanics*, 39:1–79.

Bühler, O. and Jacobson, T. E. (2001). Wave-driven currents and vortex dynamics on barred beaches. *Journal of Fluid Mechanics*, 449:313–339.

Burbea, J. (1981). On patches of uniform vorticity in a plane of irrotational flow. *Archive for Rational Mechanics and Analysis*, 77(4):349–358.

Burbea, J. and Landau, M. (1982). The kelvin waves in vortex dynamics and their stability. *Journal of Computational Physics*, 45(1):127–156.

Cabral, H. E. and Schmidt, D. S. (2000). Stability of relative equilibria in the problem of n+1 vortices. *SIAM Journal of Mathematical Analysis*, 31(2):231–250.

Carnevale, G. and Kloosterziel, R. (1994). Emergence and evolution of triangular vortices. *Journal of Fluid Mechanics*, 259:305–331.

Carton, X. J. (1992). On the merger of shielded vortices. *Europhysics Letters*, 18(8):697.

Carton, X. J., Flierl, G. R., and Polvani, L. M. (1989). The generation of tripoles from unstable axisymmetric isolated vortex structures. *Europhysics Letters*, 9(4):339.

Carton, X. J. and Legras, B. (1994). The life-cycle of tripoles in two-dimensional incompressible flows. *Journal of Fluid Mechanics*, 267:53–82.

Crowdy, D. G. (2002). Exact solutions for rotating vortex arrays with finite-area cores. *Journal of Fluid Mechanics*, 469:209–235.

Crowdy, D. G. and Marshall, J. (2004). Growing vortex patches. *Physics of Fluids*, 16(8):3122–3130.

Deem, G. S. and Zabusky, N. J. (1978). Vortex waves: Stationary "V states" interactions, recurrence, and breaking. *Physical Review Letters*, 40(13):859.

Dritschel, D. G. (1985). The stability and energetics of corotating uniform vortices. *Journal of Fluid Mechanics*, 157:95–134.

Dritschel, D. G. (1986). The nonlinear evolution of rotating configurations of uniform vorticity. *Journal of Fluid Mechanics*, 172:157–182.

Dritschel, D. G. (1988). Contour surgery: a topological reconnection scheme for extended integrations using contour dynamics. *Journal of Computational Physics*, 77(1):240–266.

Flór, J. B., Govers, W. S. S., Van Heijst, G. J. F., and Van Sluis, R. (1993). Formation of a tripolar vortex in a stratified fluid. In *Advances in Turbulence IV*, pages 405–409. Springer.

Hinch, E. J. (1991). *Perturbation methods*. Cambridge University Press.

Hinds, A. K., Johnson, E. R., and McDonald, N. R. (2007a). Interactions of two vortices near step topography. *Physics of Fluids*, 19(12):126602.

Hinds, A. K., Johnson, E. R., and McDonald, N. R. (2007b). Vortex scattering by step topography. *Journal of Fluid Mechanics*, 571:495–505.

Johnson, E. R., Hinds, A. K., and McDonald, N. R. (2005). Steadily translating vortices near step topography. *Physics of Fluids*, 17(5):056601.

Johnson, E. R. and McDonald, N. R. (2004). Surf-zone vortices over stepped topography. *Journal of Fluid Mechanics*, 511:265–283.

Lamb, H. (1932). *Hydrodynamics*. Cambridge University Press.

Larichev, V. D. and Reznik, G. M. (1983). Collision of two-dimensional solitary Rossby waves. *Okeanologiya*, 23(5):725–734.

Legras, B., Santangelo, P., and Benzi, R. (1988). High-resolution numerical experiments for forced two-dimensional turbulence. *Europhysics Letters*, 5(1):37.

Longuet-Higgins, M. S. and Stewart, R. W. (1964). Radiation stresses in water waves; a physical discussion, with applications. In *Deep Sea Research and Oceanographic Abstracts*, volume 11, pages 529–562.

Love, A. E. H. (1893). On the stability of certain vortex motions. *Proceedings of the London Mathematical Society*, 1(1):18–43.

Moore, D. W. and Saffman, P. G. (1971). Structure of a line vortex in an imposed strain. In *Aircraft wake turbulence and its detection*, pages 339–354. Springer.

Morel, Y. G. and Carton, X. J. (1994). Multipolar vortices in two-dimensional incompressible flows. *Journal of Fluid Mechanics*, 267:23–51.

Morikawa, G. K. and Swenson, E. V. (1971). Interacting motion of rectilinear geostrophic vortices. *Physics of Fluids*, 14(6):1058–1073.

Nadaoka, K. and Yagi, H. (1993). A turbulence model for shallow water and its application to large-eddy computation of longshore currents. *Doboku Gakkai Ronbunshu*, 1993(473):25–34.

Oltman-Shay, J., Howd, P. A., and Birkemeier, W. A. (1989). Shear instabilities of the mean longshore current: 2. Field observations. *Journal of Geophysical Research: Oceans*, 94(C12):18031–18042.

Overman, E. A. (1986). Steady-state solutions of the euler equations in two dimensions ii. local analysis of limiting V-states. *SIAM Journal on Applied Mathematics*, 46(5):765–800.

Özkan-Haller, H. and Kirby, J. T. (1999). Nonlinear evolution of shear instabilities of the longshore current: A comparison of observations and computations. *Journal of Geophysical Research: Oceans*, 104(C11):25953–25984.

Peregrine, D. H. (1998). Surf zone currents. *Theoretical and Computational Fluid Dynamics*, 10(1-4):295–309.

Pierrehumbert, R. T. (1980). A family of steady, translating vortex pairs with distributed vorticity. *Journal of Fluid Mechanics*, 99(1):129–144.

Polvani, L. M. and Carton, X. J. (1990). The tripole: A new coherent vortex structure of incompressible two-dimensional flows. *Geophysical & Astrophysical Fluid Dynamics*, 51(1-4):87–102.

Reinaud, J. N., Sokolovskiy, M. A., and Carton, X. J. (2017). Geostrophic tripolar vortices in a two-layer fluid: Linear stability and nonlinear evolution of equilibria. *Physics of Fluids*, 29(3):036601.

Saffman, P. G. (1992). *Vortex dynamics*. Cambridge University Press.

Saffman, P. G. and Szeto, R. (1980). Equilibrium shapes of a pair of equal uniform vortices. *Physics of Fluids*, 23(12):2339–2342.

Saffman, P. G. and Tanveer, S. (1982). The touching pair of equal and opposite uniform vortices. *Physics of Fluids (1958-1988)*, 25(11):1929–1930.

Sancho, F. E. and Svendsen, I. A. (1998). Shear waves over longshore nonuniform barred beaches. *Coastal Engineering Proceedings*, 1(26).

Slinn, D. N., Allen, J. S., Newberger, P. A., and Holman, R. A. (1998). Nonlinear shear instabilities of alongshore currents over barred beaches. *Journal of Geophysical Research: Oceans*, 103(C9):18357–18379.

Tang, Y. (1987). Nonlinear stability of vortex patches. *Transactions of the American Mathematical Society*, 304(2):617–638.

Thomson, J. J. (1883). *A Treatise on the Motion of Vortex Rings: an essay to which the Adams prize was adjudged in 1882, in the University of Cambridge*. Macmillan.

Van Heijst, G. J. F. and Kloosterziel, R. C. (1989). Tripolar vortices in a rotating fluid. *Nature*, 338(6216):569–571.

Van Heijst, G. J. F., Kloosterziel, R. C., and Williams, C. W. M. (1991). Laboratory experiments on the tripolar vortex in a rotating fluid. *Journal of Fluid Mechanics*, 225:301–331.

Wu, H. M., Overman, E. A., and Zabusky, N. J. (1984). Steady-state solutions of the euler equations in two dimensions: Rotating and translating V-states with limiting cases. i. Numerical algorithms and results. *Journal of Computational Physics*, 53(1):42–71.